

# The GLUOX Beamline and Detector

S. Adhikari<sup>w</sup>, A. Ali<sup>j,1</sup>, M. Amaryan<sup>w</sup>, E.G. Anassontzis<sup>b</sup>, E.C. Aschenauer<sup>n,2</sup>,  
A. Austregesilo<sup>c</sup>, F. Barbosa<sup>n</sup>, J. Barlow<sup>g</sup>, A. Barnes<sup>c</sup>, E. Barriga<sup>g</sup>,  
R. Barsotti<sup>k</sup>, T.D. Beattie<sup>x</sup>, D.W. Bennett<sup>k</sup>, V.V. Berdnikov<sup>d,r</sup>, G. Biallas<sup>n,3</sup>,  
T. Black<sup>u</sup>, W. Boeglin<sup>f</sup>, P. Brindza<sup>n,w</sup>, W.J. Briscoe<sup>h</sup>, T. Britton<sup>n</sup>, J. Brock<sup>n</sup>,  
W.K. Brooks<sup>y</sup>, B.E. Cannon<sup>g</sup>, C. Carlin<sup>n</sup>, D.S. Carman<sup>n</sup>, T. Carstens<sup>n,4</sup>,  
N. Cao<sup>l</sup>, O. Chernyshov<sup>m</sup>, E. Chudakov<sup>n</sup>, S. Cole<sup>a</sup>, O. Cortes<sup>h</sup>, W.D. Crahen<sup>n</sup>,  
V. Crede<sup>g</sup>, M.M. Dalton<sup>n</sup>, T. Daniels<sup>u</sup>, A. Deur<sup>n</sup>, C. Dickover<sup>n</sup>, S. Dobbs<sup>g</sup>,  
A. Dolgolenko<sup>m</sup>, R. Dotel<sup>f</sup>, M. Dugger<sup>a</sup>, R. Dzhygadlo<sup>j</sup>, A. Dzierba<sup>k,5</sup>,  
H. Egiyan<sup>n</sup>, T. Erborra<sup>f</sup>, A. Ernst<sup>g</sup>, P. Eugenio<sup>g</sup>, C. Fanelli<sup>q</sup>, S. Fegan<sup>h,6</sup>,  
A.M. Foda<sup>x</sup>, J. Foote<sup>k</sup>, J. Frye<sup>k</sup>, S. Furletov<sup>n</sup>, L. Gan<sup>u</sup>, A. Gasparian<sup>t</sup>,  
A. Gerasimov<sup>m</sup>, N. Gevorgyan<sup>ab</sup>, C. Gleason<sup>k</sup>, K. Goetzen<sup>j</sup>, A. Goncalves<sup>g</sup>,  
V.S. Goryachev<sup>m</sup>, L. Guo<sup>f</sup>, H. Hakobyan<sup>y</sup>, A. Hamdi<sup>j,1</sup>, J. Hardin<sup>q</sup>,  
A. Henderson<sup>g</sup>, C.L. Henschel<sup>x,7</sup>, G.M. Huber<sup>x</sup>, C. Hutton<sup>n</sup>, A. Hurley<sup>ac</sup>,  
D.G. Ireland<sup>l</sup>, M.M. Ito<sup>n</sup>, N.S. Jarvis<sup>c</sup>, R.T. Jones<sup>e</sup>, V. Kakoyan<sup>ab</sup>, S.  
Katsaganis<sup>x,8</sup>, G. Kalicy<sup>d</sup>, M. Kamel<sup>f</sup>, C.D. Keith<sup>n</sup>, F.J. Klein<sup>d,9</sup>, R. Kliemt<sup>j</sup>,

---

\*Corresponding author: Tel.: +1 757 269 7625.

*Email address:* [elton@jlab.org](mailto:elton@jlab.org) (E.S. Smith)

<sup>1</sup>Also at Goethe University Frankfurt, 60323 Frankfurt am Main, Germany.

<sup>2</sup>Current address: Brookhaven National Laboratory, Upton, New York 11973.

<sup>3</sup>Current address: Biallas.

<sup>4</sup>Current address: 103 Riverside Dr, Yorktown, VA 23692.

<sup>5</sup>Current address: Dzierba.

<sup>6</sup>Current address: University of York, York YO10 5DD, United Kingdom.

<sup>7</sup>Current address: Department of Physics and Astronomy, University of Calgary, Calgary, AB, T2N 1N4, Canada.

<sup>8</sup>Current address: Department of Physics, University of Regina, Regina, SK, S4S 0A2, Canada.

<sup>9</sup>Current address: Office of Academic Computing Services, University of Maryland, College Park, MD 20742.

<sup>10</sup>Current address: iQMetrix, 311 Portage Avenue, Winnipeg, MB, R3B 2B9, Canada.

<sup>11</sup>Current address: Lara.

<sup>12</sup>Current address: NASA.

<sup>13</sup>Current address: Heidelberg Universitaet, Physikalisches Institut 3.406, 69120 Heidelberg, Germany.

<sup>14</sup>Current address: Deep Silver Volition, 1 E Main St., Champaign, IL 61820.

<sup>15</sup>Current address: Oak Ridge National Laboratory, Oak Ridge, TN 37831.

<sup>16</sup>Current address: Toshiba Medical Research Institute USA, Inc., 706 N Deerpath Dr, Vernon Hills, IL 60061.

<sup>17</sup>Current address: 660 E Raven way, Gilbert, Az 85297.

<sup>18</sup>Current address: Brookhaven National Laboratory, Upton, New York 11973.

<sup>19</sup>Current address: Tykans Group Inc., 3412 25 St. NE, Calgary, AB, T1Y 6C1.

<sup>20</sup>Current address: Argonne National Laboratory, Argonne, Illinois 60439.

<sup>21</sup>Current address: Commonwealth Scientific and Industrial Research Organisation, Lucas Heights, NSW 2234, Australia.

<sup>22</sup>Current address: AbbVie Deutschland GmbH, Knollstrasse 67061, Ludwigshafen, Germany.

<sup>23</sup>Current address: University of York, York YO10 5DD, United Kingdom.

<sup>24</sup>Current address: 2808 Linden Ln, Williamsburg, VA 23185.

D. Kolybaba<sup>x</sup>, C. Kourkouvelis<sup>b</sup>, S.T. Krueger<sup>x,10</sup>, S. Kuleshov<sup>y</sup>, M. Lara<sup>k,11</sup>,  
I. Larin<sup>p,m</sup>, D. Lawrence<sup>n</sup>, J.P. Leckey<sup>k,12</sup>, D.I. Lersch<sup>g</sup>, B.D. Leverington<sup>x,13</sup>,  
W.I. Levine<sup>c</sup>, W. Li<sup>ac</sup>, B. Liu<sup>l</sup>, K. Livingston<sup>i</sup>, G.J. Lolos<sup>x</sup>,  
V. Lyubovitskij<sup>z,aa</sup>, D. Mack<sup>n</sup>, H. Marukyan<sup>ab</sup>, P.T. Mattione<sup>n,14</sup>,  
V. Matveev<sup>m</sup>, M. McCaughan<sup>n</sup>, M. McCracken<sup>c</sup>, W. McGinley<sup>c</sup>, J. McIntyre<sup>e</sup>,  
D. Meekins<sup>n</sup>, R. Mendez<sup>y</sup>, C.A. Meyer<sup>c</sup>, R. Miskimen<sup>p</sup>, R.E. Mitchell<sup>k</sup>,  
F. Mokaya<sup>e</sup>, K. Moriya<sup>a</sup>, F. Nerling<sup>j,1</sup>, L. Ng<sup>g</sup>, H. Ni<sup>h</sup>, A.I. Ostrovidov<sup>g</sup>,  
Z. Papandreou<sup>x</sup>, M. Patsyuk<sup>q</sup>, C. Paudel<sup>f</sup>, P. Pauli<sup>i</sup>, R. Pedroni<sup>t</sup>,  
L. Pentchev<sup>n</sup>, K.J. Peters<sup>j,1</sup>, W. Phelps<sup>h</sup>, J. Pierce<sup>n,15</sup>, E. Pooser<sup>n</sup>, B. Pratt<sup>e</sup>,  
Y. Qiang<sup>n,16</sup>, N. Qin<sup>v</sup>, V. Razmyslovich<sup>n,17</sup>, J. Reinhold<sup>g</sup>, B.G. Ritchie<sup>a</sup>,  
J. Ritman<sup>o</sup>, L. Robison<sup>v</sup>, D. Romanov<sup>r</sup>, C. Romero<sup>y</sup>, C. Salgado<sup>s</sup>,  
N. Sandoval<sup>n</sup>, A.M. Schertz<sup>ac</sup>, S. Schadmand<sup>o</sup>, R.A. Schumacher<sup>c</sup>,  
C. Schwarzl<sup>j</sup>, J. Schwiening<sup>j</sup>, A.Yu. Semenov<sup>x</sup>, I.A. Semenova<sup>x</sup>, K.K. Seth<sup>v</sup>,  
X. Shen<sup>l</sup>, M.R. Shepherd<sup>k</sup>, E.S. Smith<sup>n,\*</sup>, D.I. Sober<sup>d</sup>, A. Somov<sup>n</sup>, S. Somov<sup>r</sup>,  
O. Soto<sup>y</sup>, N. Sparks<sup>a</sup>, M.J. Staib<sup>c</sup>, C. Stanislav<sup>n</sup>, J.R. Stevens<sup>ac</sup>,  
J. Stewart<sup>n,18</sup>, I.I. Strakovsky<sup>h</sup>, A. Subedi<sup>k</sup>, K. Suresh<sup>x</sup>, V.V. Tarasov<sup>m</sup>,  
S. Taylor<sup>n</sup>, L.A. Teigrob<sup>x,19</sup>, A. Teymurazyan<sup>x</sup>, A. Thiel<sup>i</sup>, I. Tolstukhin<sup>r,20</sup>,  
A. Tomaradze<sup>v</sup>, A. Toro<sup>y</sup>, A. Tsaris<sup>g</sup>, Y. Van Haarlem<sup>c,21</sup>, G. Vasileiadis<sup>b</sup>,  
I. Vega<sup>y</sup>, G. Visser<sup>k</sup>, G. Voulgaris<sup>b</sup>, N.K. Walford<sup>d,22</sup>, D. Werthmüller<sup>i,23</sup>,  
T. Whitlatch<sup>n</sup>, N. Wickramaarachchi<sup>w</sup>, M. Williams<sup>q</sup>, E. Wolin<sup>n,24</sup>, T. Xiao<sup>v</sup>,  
Y. Yang<sup>q</sup>, J. Zarling<sup>x</sup>, Z. Zhang<sup>ad</sup>, Q. Zhou<sup>l</sup>, X. Zhou<sup>ad</sup>, B. Zihlmann<sup>n</sup>

<sup>a</sup>Arizona State University, Tempe, Arizona 85287, USA

<sup>b</sup>National and Kapodistrian University of Athens, 15771 Athens, Greece

<sup>c</sup>Carnegie Mellon University, Pittsburgh, Pennsylvania 15213, USA

<sup>d</sup>Catholic University of America, Washington, D.C. 20064, USA

<sup>e</sup>University of Connecticut, Storrs, Connecticut 06269, USA

<sup>f</sup>Florida International University, Miami, Florida 33199, USA

<sup>g</sup>Florida State University, Tallahassee, Florida 32306, USA

<sup>h</sup>The George Washington University, Washington, D.C. 20052, USA

<sup>i</sup>University of Glasgow, Glasgow G12 8QQ, United Kingdom

<sup>j</sup>GSI Helmholtzzentrum für Schwerionenforschung GmbH, D-64291 Darmstadt, Germany

<sup>k</sup>Indiana University, Bloomington, Indiana 47405, USA

<sup>l</sup>Institute of High Energy Physics, Beijing 100049, People's Republic of China

<sup>m</sup>Alikhanov Institute for Theoretical and Experimental Physics NRC (Kurchatov Institute),  
Moscow, 117218, Russia

<sup>n</sup>Thomas Jefferson National Accelerator Facility, Newport News, Virginia 23606, USA

<sup>o</sup>Forschungszentrum Juelich

<sup>p</sup>University of Massachusetts, Amherst, Massachusetts 01003, USA

<sup>q</sup>Massachusetts Institute of Technology, Cambridge, Massachusetts 02139, USA

<sup>r</sup>National Research Nuclear University Moscow Engineering Physics Institute, Moscow  
115409, Russia

<sup>s</sup>Norfolk State University, Norfolk, Virginia 23504, USA

<sup>t</sup>North Carolina A&T State University, Greensboro, North Carolina 27411, USA

<sup>u</sup>University of North Carolina at Wilmington, Wilmington, North Carolina 28403, USA

<sup>v</sup>Northwestern University, Evanston, Illinois 60208, USA

<sup>w</sup>Old Dominion University, Norfolk, Virginia 23529, USA

<sup>x</sup>University of Regina, Regina, Saskatchewan, Canada S4S 0A2

<sup>y</sup>Universidad Técnica Federico Santa María, Casilla 110-V Valparaíso, Chile

<sup>z</sup>Tomsk State University, 634050 Tomsk, Russia

<sup>aa</sup>Tomsk Polytechnic University, 634050 Tomsk, Russia

<sup>ab</sup>*A. I. Alikhanian National Science Laboratory (Yerevan Physics Institute), 0036 Yerevan, Armenia*

<sup>ac</sup>*College of William and Mary, Williamsburg, Virginia 23185, USA*

<sup>ad</sup>*Wuhan University, Wuhan, Hubei 430072, People's Republic of China*

---

## Abstract

The GLUEX experiment at Jefferson Lab has been designed to study photo-production reactions with a 9-GeV linearly polarized photon beam. The energy and arrival time of beam photons are tagged using a scintillator hodoscope and a scintillating fiber array. The photon flux is determined using a pair spectrometer, while the linear polarization of the photon beam is determined using a polarimeter based on triplet photoproduction. Charged-particle tracks from interactions in the central target are analyzed in a solenoidal field using a central straw tube drift chamber and six packages of planar chambers with cathode strips and drift wires. Electromagnetic showers are reconstructed in a cylindrical scintillating fiber calorimeter inside the magnet and a lead-glass array downstream. Charged particle identification is achieved by measuring energy loss in the wire chambers and using the flight time of particles between the target and detectors outside the magnet. The signals from all detectors are recorded with flash ADCs and/or pipeline TDCs into memories allowing trigger decisions with a latency of  $3.3\ \mu\text{s}$ . The detector operates routinely at trigger rates of 40 kHz and data rates of 600 megabytes per second. We describe the photon beam, the GLUEX detector components, electronics, data-acquisition and monitoring systems, and the performance of the experiment during the first three years of operation.

---

## 1 Contents

2	<b>1 The GlueX experiment</b>	<b>5</b>
3	1.1 The Hall-D complex . . . . .	6
4	1.2 Experimental requirements . . . . .	9
5	1.3 Data requirements . . . . .	9
6	1.4 Coordinate system . . . . .	10
7	<b>2 The coherent photon source and beamline</b>	<b>10</b>
8	2.1 CEBAF electron beam . . . . .	10
9	2.2 Hall-D photon beam . . . . .	11
10	2.3 Goniometer and radiators . . . . .	14
11	2.3.1 Diamond selection and quality control . . . . .	14
12	2.4 Photon tagging system . . . . .	18
13	2.4.1 Tagger magnet . . . . .	18
14	2.4.2 Tagger Microscope . . . . .	19

15	2.4.3	Broadband tagging hodoscope . . . . .	21
16	2.5	Beam profiler . . . . .	22
17	2.6	Active collimator . . . . .	23
18	2.7	Collimator . . . . .	24
19	2.8	Triplet Polarimeter . . . . .	24
20	2.8.1	Determination of photon polarization . . . . .	24
21	2.9	Pair Spectrometer . . . . .	25
22	2.9.1	Determination of photon flux . . . . .	26
23	2.10	Total Absorption Counter . . . . .	27
24	<b>3</b>	<b>Solenoid Magnet</b>	<b>27</b>
25	3.1	Overview . . . . .	27
26	3.2	Conductor and Coils . . . . .	28
27	3.3	Cooling System . . . . .	30
28	3.4	Measurements and Controls . . . . .	30
29	3.5	Field calculation and measurement . . . . .	31
30	<b>4</b>	<b>Target</b>	<b>31</b>
31	<b>5</b>	<b>Tracking detectors</b>	<b>35</b>
32	5.1	Central drift chamber . . . . .	35
33	5.2	Forward Drift Chamber . . . . .	37
34	5.3	Electronics . . . . .	38
35	5.4	Gas system . . . . .	39
36	5.5	Calibration, performance and monitoring . . . . .	40
37	<b>6</b>	<b>Performance of the charged-particle-tracking system</b>	<b>42</b>
38	6.1	Track reconstruction . . . . .	42
39	6.2	Momentum and vertex resolution . . . . .	42
40	<b>7</b>	<b>Electromagnetic calorimeters</b>	<b>44</b>
41	7.1	Barrel Calorimeter . . . . .	44
42	7.2	Forward Calorimeter . . . . .	46
43	7.3	Electronics . . . . .	47
44	7.4	Calibration and monitoring . . . . .	48
45	7.5	Performance . . . . .	48
46	<b>8</b>	<b>Scintillation detectors</b>	<b>49</b>
47	8.1	Start Counter . . . . .	50
48	8.2	Time-of-Flight counters . . . . .	51
49	8.3	Electronics . . . . .	52
50	8.4	Calibration and monitoring . . . . .	52
51	8.5	Performance . . . . .	53

52	<b>9 Trigger</b>	<b>56</b>
53	9.1 Architecture . . . . .	56
54	9.2 Trigger types . . . . .	57
55	9.3 Performance . . . . .	58
56	<b>10 Data Acquisition</b>	<b>58</b>
57	<b>11 Slow controls</b>	<b>62</b>
58	11.1 Architecture . . . . .	62
59	11.2 Remote Units . . . . .	62
60	11.3 Supervisory Control and Data Acquisition layer . . . . .	63
61	11.4 Experiment Control System . . . . .	63
62	<b>12 Online computing system</b>	<b>64</b>
63	12.1 Monitoring . . . . .	64
64	12.2 Data transport and storage . . . . .	65
65	<b>13 Event reconstruction</b>	<b>67</b>
66	13.1 Calibration . . . . .	68
67	13.2 Monitoring . . . . .	69
68	13.3 Reconstruction . . . . .	69
69	13.4 Offsite reconstruction . . . . .	70
70	13.5 Analysis . . . . .	71
71	<b>14 Monte Carlo</b>	<b>72</b>
72	14.1 Geometry specification . . . . .	72
73	14.2 Event generators . . . . .	73
74	14.3 HDGEANT . . . . .	74
75	14.4 Detector response . . . . .	74
76	14.5 Job submission . . . . .	74
77	<b>15 Detector performance</b>	<b>75</b>
78	15.1 Charged-particle reconstruction efficiency . . . . .	75
79	15.2 Photon efficiency . . . . .	76
80	15.3 Kinematic fitting . . . . .	77
81	15.4 Invariant-mass resolution . . . . .	79
82	15.5 Particle identification . . . . .	81
83	<b>16 Summary and outlook</b>	<b>84</b>
84	<b>17 Acknowledgments</b>	<b>85</b>

85 **1. The GlueX experiment**

86 The search for Quantum ChromoDynamics (QCD) exotics uses data from  
87 a wide range of experiments and production mechanisms. Historically, the  
88 searches have looked for the gluonic excitations of mesons, searching for states

89 of pure glue, glueballs, and hybrid mesons where the gluonic field binding the  
 90 quark-anti-quark pair has been excited. Most experiments searching for glue-  
 91 balls looked for scalars [1], where the searches relied on over-population of  
 92 nonets, as well as unusual meson decay patterns. In the search for hybrid  
 93 mesons [2, 3], efforts have focused on particles with exotic quantum numbers,  
 94 that is systems beyond simple quark-anti-quark configurations. Good evidence  
 95 exists for an isospin 1 state, the  $\pi_1(1600)$ . Looking collectively at past stud-  
 96 ies, data from high-statistics photoproduction experiments in the energy range  
 97 above 6 GeV is lacking.

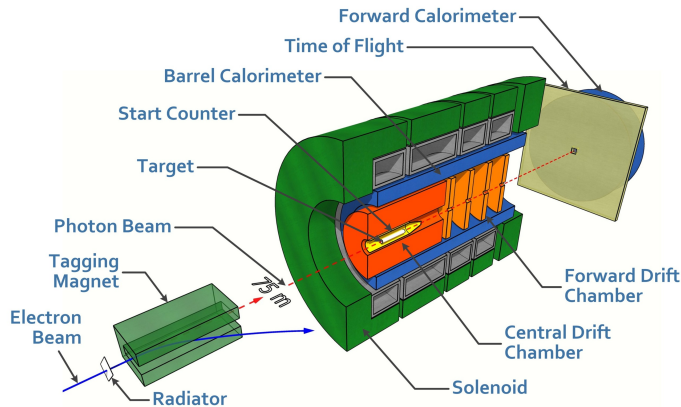


Figure 1: (Color online) A cut-away drawing of the GLUEX detector in Hall D, not to scale.

98 The *Gluonic Excitation* (GLUEX) experiment at the US Department of En-  
 99 ergy’s Thomas Jefferson National Accelerator Facility (JLab)<sup>25</sup> has been built  
 100 to both search for and map out the spectrum of exotic hybrid mesons using  
 101 a 9-GeV linearly-polarized photon beam incident on a proton target[4]. The  
 102 GLUEX detector and beamline are shown schematically in Figure 1. The de-  
 103 tector is nearly hermetic for both charged particles and photons arising from  
 104 reactions in the cryogenic target at the center of the detector, allowing for recon-  
 105 struction of exclusive final states. A 2-T solenoidal magnet surrounds the drift  
 106 chambers used for charged-particle tracking. Two electromagnetic calorimeters  
 107 cover the central and forward regions, and a scintillation detector downstream  
 108 provides particle-identification capability through time-of-flight measurements.

### 109 1.1. The Hall-D complex

110 The GLUEX experiment is housed in the Hall-D complex at JLab (see Fig.2).  
 111 This new facility starts with an extracted electron beam at the north end of  
 112 the Continuous Electron Beam Accelerator Facility (CEBAF) [5]. The electron

<sup>25</sup>Thomas Jefferson National Accelerator Facility, 12000 Jefferson Ave., Newport News, VA 23606, <https://www.jlab.org>.

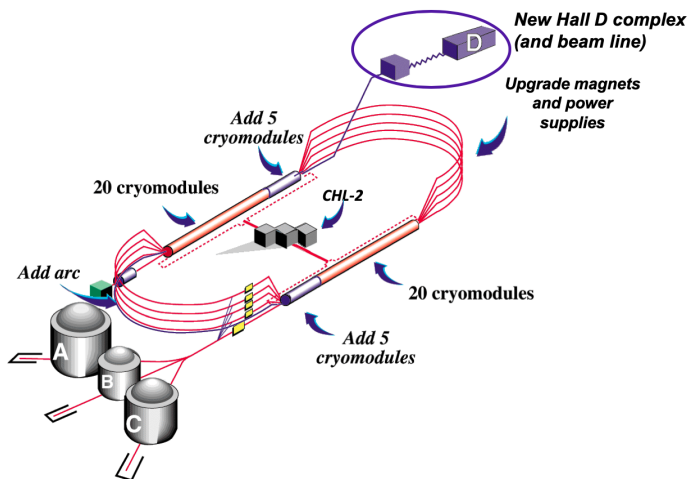


Figure 2: (Color online) Schematic of the CEBAF accelerator showing the additions made during the 12-GeV project. The Hall D complex is located at the north-east end.

113 beam is delivered to the Tagger Hall, where the maximum energy is 12 GeV, due  
 114 to an extra one-half pass of acceleration relative to three other experimental halls  
 115 (A, B and C). Here, linearly-polarized photons are produced through coherent  
 116 bremsstrahlung off a  $50 \mu\text{m}$  thick diamond crystal radiator. The scattered  
 117 electrons pass through a tagger magnet and are bent into tagging detectors. A  
 118 high-resolution scintillating-fiber tagging array covers the 8 to 9 GeV energy  
 119 range, and a tagger hodoscope covers photon energies both from 9 GeV to the  
 120 endpoint, and from 8 GeV to 3 GeV. Electrons not interacting in the diamond  
 121 are directed into a 60 kW electron beam dump. The tagged photons travel to  
 122 the Hall-D experimental hall. The distance from the radiator to the primary  
 123 collimator is 75 m. The collimator, with a diameter of 5 mm diameter, removes  
 124 off-axis incoherent photons. The front face of the collimator is instrumented  
 125 with an active collimator to aid in beam tuning. The beamline and tagging  
 126 system are described below in Section 2.

127 Downstream of the primary collimator is a thin beryllium radiator used  
 128 by both the Triplet Polarimeter, which measures the linear polarization of the  
 129 photons, and a Pair Spectrometer, which is used to measure the flux of the  
 130 photons. More information on the production, tagging and monitoring of the  
 131 photon beam can be found in Section 2. The photon beam continues through  
 132 to a liquid hydrogen target at the heart of the GLUEX detector, and then to  
 133 the end of the experimental hall where it enters the photon beam dump.

134 The layout of the GLUEX detector is shown in Fig. 3. The spectrometer  
 135 is based on a 4-m-long solenoidal magnet that is operated at a maximum field  
 136 of 2 T, see Section 3. The liquid-hydrogen target is located 65 cm inside the  
 137 upstream bore of the magnet. The target consists of a 2-cm-diameter, 30-cm-  
 138 long volume of hydrogen, as described in Section 4. Surrounding the target is

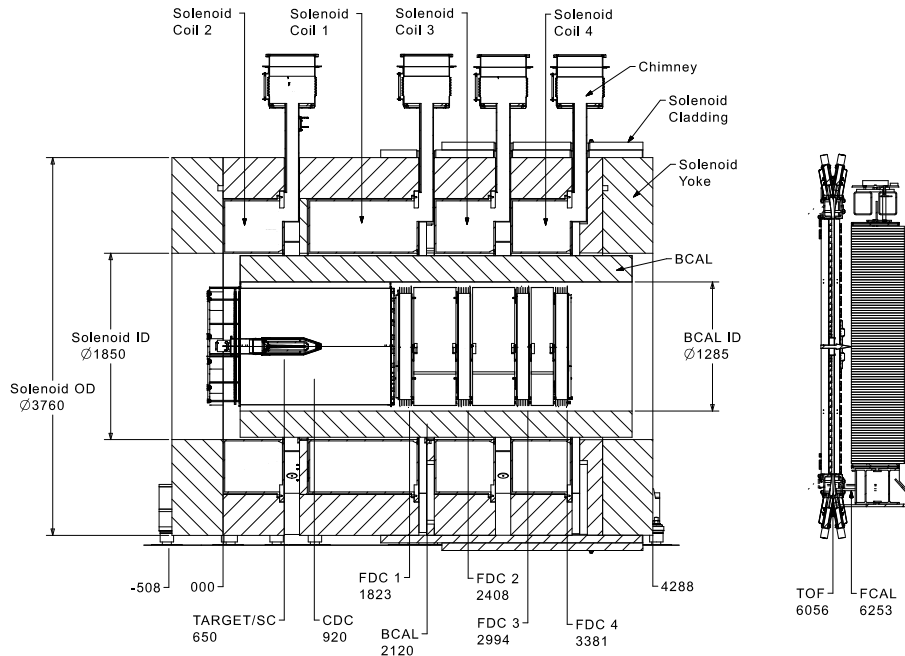


Figure 3: GlueX spectrometer layout. Dimensions are given in mm. The numbers show the Z-coordinates of the detectors' centers, or of the front face of the calorimeter modules in case of the FCAL. Glossary: SC - Start Counter (Section 8.1), CDC - Central Drift Chamber (Section 5.1), FDC - Forward Drift Chamber (Section 5.2), BCAL - Barrel Calorimeter (Section 7.1), TOF - Time-of-Flight hodoscope (Section 8.2), FCAL - Forward Calorimeter (Section 7.2).

139 the Start Counter, which consists of 30 thin scintillator paddles that bend to  
 140 a nose on the down-stream end of the hydrogen target. The Start Counter is  
 141 the primary detector that registers the time coincidence of the radio-frequency  
 142 (RF) bunch containing the incident electron and the tagged photon producing  
 143 the interaction. More information on the scintillator detector can be found in  
 144 Section 8.

145 Starting at a radius of 10 cm from the beam line is the Central Drift Cham-  
 146 ber, a cylindrical straw-tube detector. The active volume of the chamber ex-  
 147 tends from 48 cm upstream to 102 cm downstream of the target center, and  
 148 from 10 cm to 56 cm in radius. The Central Drift Chamber consists of 28 layers  
 149 of straw tubes in axial and two stereo orientations. Downstream of the central  
 150 tracker is the Forward Drift Chamber, which consists of four packages, each  
 151 containing 6 planar layers in alternating  $u$ - $y$ - $v$  orientations. Both cathodes and  
 152 anodes in the Forward Drift Chamber are read out, providing three-dimensional  
 153 space point measurements. More details on the tracking system are provided in  
 154 Sections 5 and 6.

155 Downstream of the magnet is the Time-of-Flight wall. This system consists  
 156 of two layers of scintillator paddles in a crossed pattern, and, in conjunction



157 with the Start Counter, is used to measure the flight time of charged parti-  
158 cles. More information on the time-of-flight system is provided in Section 8.  
159 Photons arising from interactions within in the GLUEX target are detected by  
160 two calorimeter systems. The Barrel Calorimeter, located inside the solenoid,  
161 consists of layers of scintillating fibers alternating with lead sheets. The For-  
162 ward Calorimeter is downstream of the Time-of-Flight wall, and consists of  
163 2800 lead-glass blocks. More information on the the calorimeters can be found  
164 in Section 7.

### 165 *1.2. Experimental requirements*

166 The physics goals of the GlueX experiment require the reconstruction of ex-  
167 clusive final states. Thus, the GLUEX detector must be able to reconstruct both  
168 charged particles ( $\pi^\pm$ ,  $K^\pm$  and  $p/\bar{p}$ ) and particles decaying into photons ( $\pi^0$ ,  $\eta$ ,  
169  $\omega$  and  $\eta'$ ). For this capability, the charged particles and photons must be re-  
170 constructed with good momentum and energy resolution. The experiment must  
171 also be able to reconstruct the energy of the incident photon (8 to 9 GeV) with  
172 high accuracy (0.1%) and have knowledge of the linear polarization (maximum  
173  $\sim 40\%$ ) of the photon beam to an absolute precision of 1%. Finally, many inter-  
174 esting final states involve more than five particles. Thus, the GLUEX detector  
175 must also be nearly hermetic for both charged particles and photons, with an  
176 acceptance that is reasonably uniform, well understood, and accurately modeled  
177 in simulation.

178 In practice, the typical momentum resolution for charged particles is 1–3%,  
179 while the resolution is 8-9% for very-forward high-momentum particles. For  
180 most charged particles, the tracking system has nearly hermetic acceptance for  
181 polar angles from  $1^\circ - 2^\circ$  to  $150^\circ$ . However, protons with momenta below about  
182 250 MeV/c are absorbed in the hydrogen target and not detected. A further  
183 challenge is the reconstruction of tracks from charged pions with momenta under  
184 200 MeV/c due to spiraling trajectories in the magnetic field. The measurement  
185 of energy loss ( $dE/dx$ ) in the Central Drift Chamber enables the separation of  
186 pions and protons up to about 800 MeV/c, while time-of-flight determination  
187 allows separation of forward-going pions and kaons up to about 2 GeV/c.

188 For photons produced from the decays of reaction products, the typical en-  
189 ergy resolution is 5 to 6%/ $\sqrt{E_\gamma}$ . Photons above 60 MeV can be detected in  
190 the Barrel Calorimeter, with some variation depending on the incident angle.  
191 The interaction point along the beam direction is determined by comparing the  
192 information from the readouts on the upstream and downstream ends of the de-  
193 tector. In the Forward Calorimeter, photons with energies larger than 100 MeV  
194 can be detected with uniform resolution across the face of the detector. There is  
195 a gap region between the calorimeters at around  $11^\circ$ , where energy can be lost  
196 due to shower leakage. Both photon detection efficiency and energy resolution  
197 are degraded in this region.

### 198 *1.3. Data requirements*

199 The physics analyses need to be carried out in small bins of energy and  
200 momentum transfer, necessitating not only the ability to reconstruct exclusive

Table 1: Electron beam parameters. The emittance, energy spread and related parameters are estimates based on a model of the transport line from the accelerator to the Hall D radiator. The dimensions of the beam spot at the position of the radiator are directly measured, and vary around the stated values by  $\pm 30\%$  depending on beam conditions. Values for image size at collimator, obtained by projection of the electron beam spot convergence forward to the position of the primary photon collimator, have relative uncertainties of 50%.

parameter	design results
energy	12 GeV
energy spread, RMS	2.2 MeV
transverse $x$ emittance	2.7 mm $\cdot\mu$ rad
transverse $y$ emittance	1.0 mm $\cdot\mu$ rad
$x$ spot size at radiator, RMS	1.1 mm
$y$ spot size at radiator, RMS	0.7 mm
$x$ image size at collimator, RMS	0.5 mm
$y$ image size at collimator, RMS	0.5 mm
image offset from collimator axis, RMS	0.2 mm
distance radiator to collimator	75.3 m

201 final states but also to collect sufficient statistics. While exact cross sections are  
 202 not known, the cross sections of interest will be in the 10 nb to 1  $\mu$ b range.

203 This paper describes the operation of GLUEX Phase I. During this initial  
 204 phase, the GLUEX experiment has run with a data acquisition system capable of  
 205 collecting data using photon beams of a few  $10^7$   $\gamma$ /s in the coherent peak (8.4-9  
 206 GeV), with an expectation to run with 2.5 times higher rates in the future.  
 207 The data acquisition system ran routinely at 40 kHz with raw event sizes of 15-  
 208 20 kilobytes, collecting about 600 megabytes of data per second. With trigger  
 209 improvements, future running is expected at 90 kHz and 1 gigabyte per second.  
 210 Details of the trigger and data acquisition are presented in Sections 9 and 10.

#### 211 1.4. Coordinate system

212 For reference, we introduce here the overall experiment coordinate system,  
 213 which is used in this document and throughout the analysis. The experimental  
 214 area is located off the northeast corner of the accelerator. The  $z$ -axis is defined  
 215 along the nominal beamline increasing downstream (toward the east). The  
 216 coordinate system is right-handed with the  $y$ -axis pointing vertically up and the  
 217  $x$ -axis pointing approximately north. The origin is located 50.8 cm (20 inches)  
 218 downstream of the upstream side of the upstream endplate of the solenoid,  
 219 placing the nominal center of the target at (0,0,65 cm).

## 220 2. The coherent photon source and beamline

### 221 2.1. CEBAF electron beam

222 CEBAF has a race track configuration with two parallel linear accelerators  
 223 based on superconducting radio frequency (RF) technology [5]. The machine

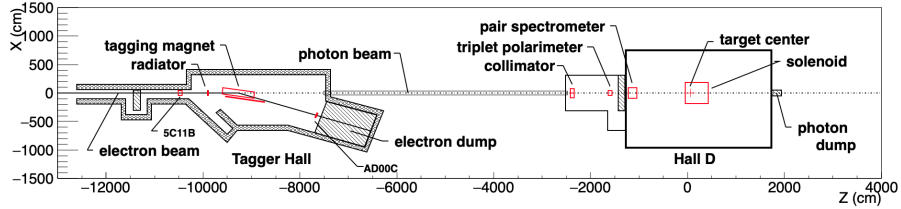


Figure 4: Schematic layout of the Hall-D complex, showing the Tagger Hall, Hall D, and several of the key beamline devices. Also indicated are the locations of the 5C11B and AD00C beam position monitors.

224 operates at 1.497 GHz and delivers beam to Hall D at 249.5 MHz.<sup>26</sup> Precise  
 225 timing signals for the accelerator beam bunches are available to the experiment  
 226 and are used to determine the time that individual tagged photon bunches pass  
 227 through the target. The nominal properties for the CEBAF electron beam to  
 228 the Tagger Hall are listed in Table 1.

## 229 2.2. Hall-D photon beam

230 The Hall-D complex, described in Section 1.1 and shown schematically in  
 231 Fig. 4, includes a dedicated Tagger Hall, an associated collimator cave, and  
 232 Experimental Hall D itself. A linearly-polarized photon beam is created using  
 233 the process of coherent bremsstrahlung [6, 7] when the electron beam passes  
 234 through an oriented diamond radiator at the upstream end of the Tagger Hall.  
 235 The electron beam position at the radiator is monitored and controlled using  
 236 beam position monitors (5C11 and 5C11B) which are located at the end of the  
 237 accelerator tunnel just upstream of the Tagger Hall (see Fig. 4.) The CEBAF  
 238 electron beam is tuned to converge as it passes through the radiator, ideally  
 239 so that the electron beam forms a virtual focus at the collimator located 75 m  
 240 downstream of the radiator. At the collimator, the virtual spot size of 0.5 mm  
 241 is small compared to the cm-scale size of the photon beam on the front face of  
 242 the collimator, such that a cut on photon position at the collimator is effectively  
 243 a cut on photon emission angle at the radiator. The convergence properties of  
 244 the electron beam are measured by scanning the beam profile with vertical and  
 245 horizontal wires. The intensity of the scattered beam is determined from the  
 246 induced current on the wires as a function of position. The wire scanners are  
 247 referred to as "harps." Examples of the horizontal and vertical convergence of  
 248 the electron beam envelope (undeflected by the tagger magnet) measured using  
 249 harp scans and projected downstream along the beamline are shown in Fig. 5.

250 The photon beam position on the collimator is monitored using an active  
 251 collimator positioned just upstream of the primary photon beam collimator  
 252 (described below in section 2.6). The position stability of the photon beam is

<sup>26</sup>Hall D beam at 499 MHz is possible, but not the norm.

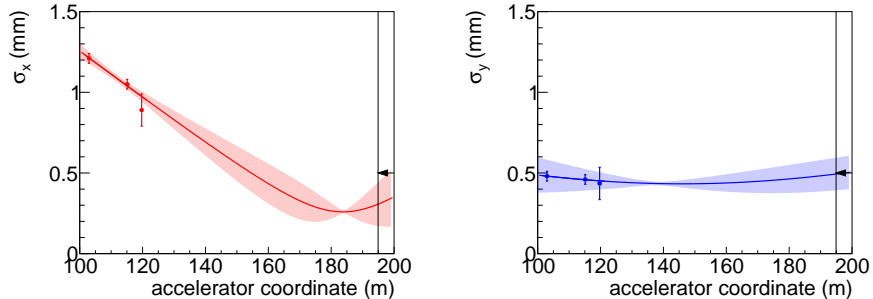


Figure 5: (Color online) Measurements of the root-mean-square width of the electron beam in horizontal (left) and vertical (right) projections as a function of position along the beamline, based on harp scans (data points) of the electron beam. The radiator position is just upstream of the third data point. The primary collimator position is marked by the vertical line indicated by the arrow. The curve downstream of the radiator is an extrapolation from the measured data points, with extrapolation uncertainty indicated by the shaded regions.

253 maintained during normal operation by a feedback system that locks the position  
 254 of the electron beam at the 5C11B beam profile monitor and, consequently, the  
 255 photon beam at the active collimator. The stability of the electron beam current  
 256 and position is monitored using an independent beam position monitor (AD00C  
 257 in Fig. 4) located immediately upstream of the electron dump.

258 The linearly-polarized photon beam is produced via a radiator placed in the  
 259 electron beam just upstream of the Tagger (section 2.4). A properly aligned 20–  
 260 60  $\mu\text{m}$  thick diamond crystal radiator produces linearly polarized photons via  
 261 coherent bremsstrahlung in enhancements [6, 7], that appear as peaks at certain  
 262 energies in the bremsstrahlung intensity spectrum (Fig. 6), superimposed upon  
 263 the ordinary continuum bremsstrahlung spectrum. The energies of the coherent  
 264 photon peaks and the degree of polarization in each of those peaks depend on  
 265 the crystal orientation with respect to the incident electron beam. Adjustment  
 266 of the orientation of the diamond crystal with respect to the incoming electron  
 267 beam permits production of essentially any coherent photon peak energy up  
 268 to that of the energy of the incident electron beam, as well as the degree or  
 269 direction of linear polarization. A choice of 9 GeV for the primary peak energy,  
 270 corresponding to 40% peak linear polarization, was found to be optimum for  
 271 the GLUEX experiment with a 12-GeV incident electron beam.

272 The degree of polarization for a coherent bremsstrahlung beam is great-  
 273 est for photons emitted at small angles with respect to the incident electron  
 274 direction. Collimation of the photon beam to a fraction of the characteristic  
 275 bremsstrahlung angle exploits this correlation to significantly enhance the aver-  
 276 age polarization of the beam. In the nominal GLUEX beamline configuration,

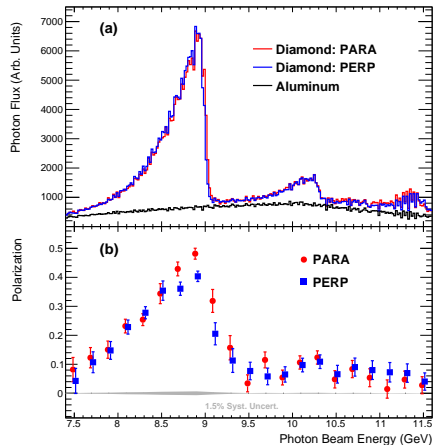


Figure 6: (color online) (a) Photon beam intensity versus energy as measured by the Pair Spectrometer (not corrected for instrumental acceptance). (b) Photon beam polarization as a function of beam energy, as measured by the Triplet Polarimeter, with data points offset horizontally by  $\pm 0.015$  GeV for clarity. The labels PARA and PERP refer to orientations of the diamond radiator that result in polarization planes that are parallel and perpendicular to the horizontal, respectively.

277 a 5.0-mm-diameter collimator<sup>27</sup> positioned 75 m downstream of the radiator is  
 278 used, corresponding to a cut at approximately  $1/2 m/E$  in characteristic angle,  
 279 where  $m$  is the electron rest mass and  $E$  is the energy of the incident elec-  
 280 tron. The photon beam energy spectrum and photon flux after collimation are  
 281 measured by the Pair Spectrometer (section 2.9), located downstream of the  
 282 collimator in Hall D.

283 An example of the measured photon spectrum and degree of polarization  
 284 with a 12-GeV electron beam is shown in Fig. 6. The spectrum labeled “Alu-  
 285 minium” in Fig. 6(a) is shown to indicate the shape of the Pair Spectrometer  
 286 acceptance folded with the spectrum of ordinary (incoherent) bremsstrahlung,  
 287 normalized to the approximate thickness of the diamond radiator in terms of  
 288 radiation lengths. The expected degree of linear polarization in the energy range  
 289 of 8.4–9.0 GeV is  $\sim 40\%$  after collimation. The photon beam polarization is di-  
 290 rectly measured by the triplet polarimeter (section 2.8) located just upstream of  
 291 the pair spectrometer. The stability of the beam polarization is independently  
 292 monitored via the observed azimuthal asymmetry in various photoproduction  
 293 reactions, particularly that for  $\rho$  photoproduction [8].

294 Typical values for parameters and properties of the photon beam are given in  
 295 Table 2. In the sections that follow, we describe in more detail how the linearly-  
 296 polarized photon beam is produced, how the photon energy is determined using

<sup>27</sup>A 3.4 mm collimator is also available, and has been used for some physics production runs with the thinnest ( $20 \mu m$ ) diamond.

Table 2: Typical parameters for the GLUEX photon beam, consistent with the electron beam properties listed in Table 1, a diamond radiator of thickness  $50\ \mu\text{m}$ , and the standard primary collimator of diameter 5.0 mm located at the nominal position. The electron beam current incident on the radiator is taken to be 150 nA. The hadronic rates are calculated for the GLUEX 30 cm liquid hydrogen target.

$E$ upper edge of the coherent peak	9 GeV
Coherent peak effective range	8.4 - 9.0 GeV
Net tagger rate in the coherent peak range	45 MHz
$N_\gamma$ in the peak range after collimator	24 MHz
Maximum polarization in the peak, after collimator	40%
Mean polarization in the peak range, after collimator	35%
Power absorbed on collimator	0.60 W
Power incident on target	0.23 W
Total hadronic rate	70 kHz
Hadronic rate in the peak range	3.7 kHz

297 the tagging spectrometer, how the photon beam polarization spectrum and flux  
 298 are measured with the Pair Spectrometer and Triplet Polarimeter, and how the  
 299 photon flux is calibrated using the Total Absorption Counter.

### 300 2.3. Goniometer and radiators

301 For the linearly-polarized photon beam normally used in GLUEX produc-  
 302 tion running, diamond radiators are used to produce a coherent bremsstrahlung  
 303 beam. This requires precise alignment of the diamond radiator, in order to  
 304 produce a single dominant coherent peak<sup>28</sup> with the desired energy and polar-  
 305 ization by scattering the beam electrons from the crystal planes associated with  
 306 a particular reciprocal lattice vector. A multi-axis goniometer, manufactured by  
 307 Newport Corporation, precisely adjusts the relative orientation of the diamond  
 308 radiator with respect to the incident electron beam horizontally, vertically and  
 309 rotationally about the  $X$ ,  $Y$  and  $Z$  axes, respectively. The Hall-D goniometer  
 310 holds several radiators, any of which may be moved into the beam for use at  
 311 any time according to the requirements of the experiment.

312 In addition to the diamond radiators, several aluminum radiators of thick-  
 313 nesses ranging from 1.5 to  $40\ \mu\text{m}$  are used to normalize the rate spectra measured  
 314 in the Pair Spectrometer, correcting for its acceptance. A separate rail for these  
 315 amorphous radiators is positioned 615 mm downstream of the goniometer.

#### 316 2.3.1. Diamond selection and quality control

317 The properties of diamond are uniquely suited for coherent bremsstrahlung  
 318 radiators. The small lattice constant and high Debye temperature of diamond

---

<sup>28</sup>Defined as 0.6 GeV below the coherent edge (nominally 9 GeV). The position of the edge scaled approximately with the primary incident electron beam energy.

319 result in an exceptionally high probability for coherent scattering in the brems-  
320 strahlung process [9]. Also, the high coherent scattering probability is a conse-  
321 quence of the small atomic number of carbon ( $Z = 6$ ). At the dominant crystal  
322 momentum (9.8 keV) corresponding to the leading (2,2,0) reciprocal lattice vec-  
323 tor, the small atomic number results in minimal screening of the nuclear charge  
324 by inner shell electrons. Diamond is the best known material in terms of its  
325 coherent radiation fraction, and its unparalleled thermal conductivity and ra-  
326 diation hardness make it well-suited for use in a high-intensity electron beam  
327 environment.

328 The position of the coherent edge in the photon beam intensity spectrum is  
329 a simple monotonic function of the angle between the incident electron beam  
330 direction and the normal to the (2,2,0) crystal plane. The 12-GeV-electron  
331 beam entering the radiator has a divergence less than  $10 \mu\text{rad}$ , corresponding  
332 to a broadening of the coherent edge in Fig. 6 by just 7 MeV. However, if the  
333 incident electron beam had to travel through  $100 \mu\text{m}$  of diamond material prior  
334 to radiating, the resulting electron beam emittance would increase by a factor  
335 of 10 due to multiple Coulomb scattering, resulting in a proportional increase in  
336 the width of the coherent edge. Such broadening of the coherent peak diminishes  
337 both the degree of polarization in the coherent peak as well as the collimation  
338 efficiency in the forward direction. Hence, diamond radiators for GLUEX must  
339 be significantly thinner than 100 microns.

340 The cross-sectional area of a diamond target must also be large enough to  
341 completely contain the electron beam so that the beam does not overlap with  
342 the material of the target holder. Translated to the beam spot dimensions from  
343 Table 1, GLUEX requires a target with transverse size 5 mm or greater. Uniform  
344 single-crystal diamonds of this size are now available as slices cut from natural  
345 gems, HPHT (high-pressure, high-temperature) synthetics, and CVD (chemical  
346 vapor deposition) single crystals. Natural gems are ruled out due to cost. HPHT  
347 crystals had been thought to be far superior to CVD single crystals in terms  
348 of their diffraction widths, but our experience did not bear this out. GLUEX  
349 measurements of the x-ray rocking curves of CVD crystals obtained from the  
350 commercial vendor Element Six routinely showed widths that were within a  
351 factor 2 of the theoretical Darwin widtht diamond, similar to the results we  
352 found for the best HPHT diamonds that were available to us [10, 11].

353 Fig. 7 shows a rocking curve topograph of a diamond radiator taken with  
354 15 keV x-rays at the Cornell High Energy Synchrotron Source (CHESS). The  
355 instrumental resolution of this measurement is on the same order as the Darwin  
356 width for this diffraction peak, approximately  $5 \mu\text{rad}$ . During operation, the  
357 electron beam spot would be confined to the relatively uniform central region.  
358 Any region in this figure with a rocking curve root-mean-square width of  $20 \mu\text{rad}$   
359 or less is indistinguishable from a perfect crystal for the purposes of GLUEX.  
360 Regardless of whether or not better HPHT diamonds exist, these Element Six  
361 CVD diamonds have sufficiently narrow diffraction widths for our application.  
362 This, coupled with their lower cost relative to HPHT material, made them the  
363 obvious choice for the Hall-D photon source.

364 The diamond radiator fabrication procedure began with procurement of the

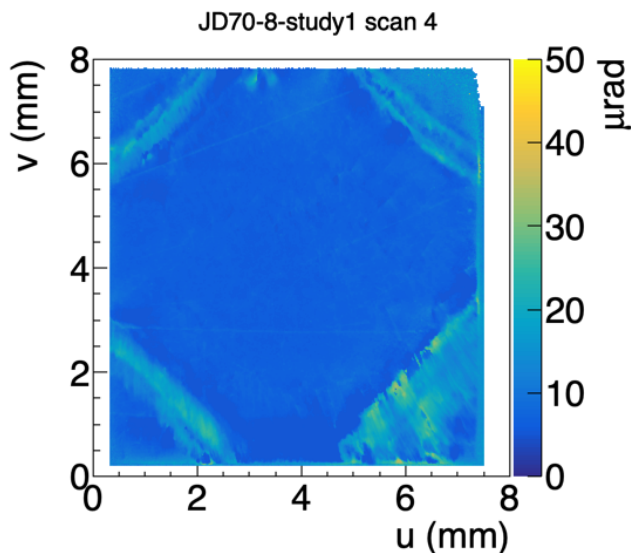


Figure 7: (color online) Rocking curve RMS width topograph taken of the (2,2,0) reflection from a CVD diamond crystal using 15 keV X-rays at the C-line at CHESS. The bright diagonal lines in the corners indicate regions of increased local strain, coinciding with growth boundaries radiating outward from the seed crystal used in the CVD growth process.

365 raw material in the form of  $7 \times 7 \times 1.2 \text{ mm}^3$  CVD single-crystal plates from  
 366 the vendor. After x-ray rocking curve scans of the raw material were taken  
 367 to verify crystal quality, the acceptable diamonds were shipped to a second  
 368 vendor, Delaware Diamond Knives (DDK). At DDK, the 1.2-mm-thick samples  
 369 were sliced into three samples of  $250 \text{ }\mu\text{m}$  thickness each, then each one was  
 370 polished on both sides down to a final thickness close to  $50 \text{ }\mu\text{m}$ . The samples,  
 371 now of dimensions  $7 \times 7 \times 0.05 \text{ mm}^3$  were fixed to a small aluminum mounting  
 372 tab using a tiny dot of conductive epoxy placed in one corner. These crystals  
 373 were then returned to the synchrotron light source for final x-ray rocking curve  
 374 measurements prior to final approval for use in the GLUEX photon source.

375 The useful lifetime of a diamond radiator in the GLUEX beamline is limited  
 376 by the degradation in the sharpness of the coherent edge due to accumulation  
 377 of radiation damage. Experience during the early phase of GLUEX running  
 378 showed that after exposure to about 0.5 C of integrated electron beam charge,  
 379 the width of the coherent edge increased enough that the entire coherent peak  
 380 was no longer contained within the energy window of the tagger microscope.  
 381 When a crystal reached this degree of degradation, the radiator was regarded  
 382 as no longer usable, and a new crystal was installed.

383 During Phase 1 of GLUEX, radiator crystals were replaced three times due  
 384 to degradation, twice with  $50 \text{ }\mu\text{m}$  radiators and once with a  $20 \text{ }\mu\text{m}$  radiator. The  
 385  $20\text{-}\mu\text{m}$  diamond was introduced to test if the reduced multiple Coulomb scat-



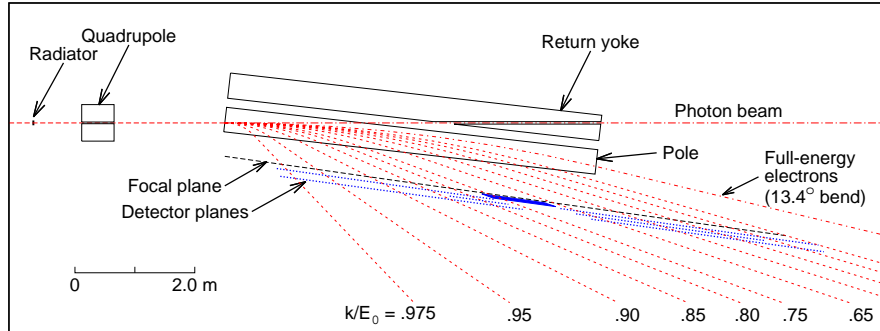


Figure 8: Schematic diagram of the tagging spectrometer, showing the paths of the electron and photon beams. Dotted lines indicate post-radiation electron trajectories identified by the energy the electron gave up to an associated radiated photon, as a fraction of the beam energy  $E_0$ . The Tagger focal plane detector arrays TAGH and TAGM are described in the text.

386 tering might result in an observable increase in peak polarization. This turned  
 387 out not to be the case, for two reasons. The first is that to take full advantage  
 388 of the reduced multiple scattering in the radiator for increased peak polarization,  
 389 the collimator size must be reduced proportionally. A 3.4-mm-diameter  
 390 collimator was available for this purpose, but variability observed in the convergence  
 391 properties of the electron beam at the radiator overruled running with  
 392 any collimator smaller than 5 mm, even when a thinner radiator was in use.

393 The second reason is that any improvements from reduced multiple scattering  
 394 that came with the smaller radiator thickness were more than offset by  
 395 strong indications of radiation damage that appeared not long after the 20  $\mu\text{m}$   
 396 crystal was put into production. The rapid appearance of radiation damage was  
 397 partly due to the larger beam current (factor 2.5) that was needed to produce  
 398 the same photon flux as with a 50  $\mu\text{m}$  crystal, but that factor alone did not  
 399 fully explain what was seen. Subsequent x-ray measurements showed that a  
 400 large buckling of the 20  $\mu\text{m}$  crystal had occurred in the region of the incident  
 401 electron beam spot, evidently due to local differential expansion of the diamond  
 402 lattice arising from radiation damage. Once the crystal buckled, the energy  
 403 of the coherent peak varied significantly across the electron beam spot, effectively  
 404 broadening the peak. Fortunately, the greater stiffness of a 50  $\mu\text{m}$  crystal  
 405 appears to suppress this local buckling under similar conditions of radiation  
 406 damage.

407 Based on these observations, 50  $\mu\text{m}$  was selected as the optimum thickness  
 408 for GLUEX diamond radiators: thin enough to limit the effects of multiple  
 409 scattering and thick enough to suppress buckling from internal stress induced  
 410 by radiation damage. The effective useful lifetime of a 50  $\mu\text{m}$  radiator in the  
 411 photon source is about 0.5 C integrated incident electron charge. This lifetime  
 412 might be extended somewhat by the use of thermal annealing to partially remove  
 413 the effects of radiation damage. This possibility will be explored when the pace  
 414 of diamond replacement increases with the start of GlueX Phase 2 full-intensity  
 415 running and the number of spent radiators starts to accumulate.

416 *2.4. Photon tagging system*

417 After passing through the radiator, the combined photon and electron beams  
418 enter the photon tagging spectrometer (Tagger). The full-energy electrons are  
419 swept out of the beamline by a dipole magnet and redirected into a shielded  
420 beam dump. The subset of beam electrons that radiated a significant frac-  
421 tion of their energy in the radiator are bent further by the dipole field. These  
422 post-bremsstrahlung electrons exit through a thin window along the side of the  
423 magnet, and detected in a highly segmented array of scintillators called the  
424 Tagger Hodoscope, as shown in Fig. 8. The TAGH counters span the full range  
425 in energy from 25% to 97% of the full electron beam energy. A high-energy-  
426 resolution device known as the Tagger Microscope (TAGM) covers the energy  
427 range corresponding to the primary coherent peak, indicated by the denser por-  
428 tion of the focal plane in Fig. 8. The quadrupole magnet upstream of the Tagger  
429 dipole provides a weak vertical focus, optimizing the efficiency of the Tagger Mi-  
430 croscope for tagging collimated photons. A 0.8 Tm permanent dipole magnet is  
431 installed downstream of the Tagger magnet on the photon beam line, in order  
432 to prevent the electron beam from reaching Hall D should the Tagger magnet  
433 trip.

434 Both the TAGM and TAGH devices are used to determine the energy of  
435 individual photons in the photon beam via coincidence, using the relation  $E_\gamma =$   
436  $E_0 - E_e$ , where  $E_0$  is the primary electron beam energy before interaction with  
437 the radiator, and  $E_e$  is the energy of the post-bremsstrahlung electron deter-  
438 mined by its detected position at the focal plane. Multiple radiative interactions  
439 in a 50  $\mu\text{m}$  diamond radiator ( $3 \times 10^{-4}$  radiation lengths) produce uncertainties  
440 in  $E_\gamma$  of the same order as the intrinsic energy spread of the incident electron  
441 beam.

442 *2.4.1. Tagger magnet*

443 The Hall-D Tagger magnet deflects electrons in the horizontal plane, allow-  
444 ing the bremsstrahlung-produced photons to continue to the experimental hall  
445 while bending the electrons that produced them into the focal plane detectors.  
446 Electrons that lose little or no energy in the radiator are deflected by  $13.4^\circ$  into  
447 the electron beam dump.

448 The Hall-D Tagger magnet is an Elbek-type room temperature dipole mag-  
449 net, similar to the JLab Hall-B tagger magnet [12, 13]. The magnet is 1.13 m  
450 wide, 1.41 m high and 6.3 m long, weighing 80 metric tons, with a normal op-  
451 erating field of 1.5 T for a 12-GeV incident electron beam, a maximum field of  
452 1.75 T, and a pole gap of 30 mm. The magnet design was optimized using the  
453 detailed magnetic field calculation provided by the TOSCA simulation package  
454 and ray tracing of electron beam trajectories [14, 15].

455 The GlueX experiment requirements mandate that the scattered electron  
456 beam be measured with an accuracy of 12 MeV (0.1% of the incident electron  
457 energy). This requires that the magnetic field integrals along all useful electron  
458 trajectories be known to 0.1%. The magnetic field was mapped at Jefferson Lab  
459 and the detailed field maps were augmented by detailed TOSCA calculations,

460 which have allowed us to meet these goals. Details of the magnet mapping and  
461 uniformity are found in Ref. [16].

#### 462 *2.4.2. Tagger Microscope*

463 The Tagger Microscope (TAGM) is a high-resolution hodoscope that counts  
464 post-bremsstrahlung electrons corresponding to the primary coherent peak. Nor-  
465 mally the TAGM is positioned to cover between 8.2 and 9.2 GeV in photon en-  
466 ergy, but the TAGM is designed to be movable should a different peak energy be  
467 desired. The microscope is segmented along the horizontal axis into 102 energy  
468 bins (columns) of approximately equal width. Each column is segmented in five  
469 sections (rows) along the vertical axis. The vertical segmentation allows the  
470 possibility of scattered electron collimation, which gives a significant increase  
471 in photon polarization when used in combination with photon collimation. The  
472 purpose of the quadrupole magnet upstream of the dipole is to provide the  
473 vertical focus needed to make the double-collimation scheme work efficiently.  
474 Summed signals are also available for each column for use in normal operation  
475 when electron collimation is not desired.

476 The Tagger Microscope consists of a two-dimensional array of square scin-  
477 tillating fibers packed in a dense array of dimensions  $102 \times 5$ . The fibers are  
478 multi-clad BCF-20 with a  $2 \times 2$  mm<sup>2</sup> square transverse profile, manufactured by  
479 Saint Gobain. The cladding varies in thickness from 100 microns near the cor-  
480 ners to 70 microns in the middle of the sides, with an active area of  $1.8 \times 1.8$  mm<sup>2</sup>  
481 per fiber. Variations at the level of 5% in the transverse size of the fibers impose  
482 a practical lower bound of 2.05 mm on the pitch of the array. The detection  
483 efficiency of the TAGM averages 75% across its full energy range, in good agree-  
484 ment with the geometric factor of 77%.

485 Each scintillating fiber is 10 mm long, fused at its downstream end to a  
486 clear light guide of matching dimensions (Saint Gobain BCF-98) that transmits  
487 the scintillation light from the focal plane to a shielded box where a silicon  
488 photomultiplier (SiPM) converts light pulses into electronic signals. The scin-  
489 tillators are oriented so that the electron trajectories are parallel to the fiber  
490 axis, providing large signals for electrons from the radiator, in contrast to the  
491 omni-directional electromagnetic background in the tagger hall.

492 Because the electron trajectories do not cross the focal plane at right angles,  
493 the fiber array must be staggered along the dispersion direction. A staggering  
494 step occurs every 6 columns, as illustrated in Fig. 9. The slight variation of  
495 the crossing angle  $\beta$  is taken into account by a carefully adjusted fan-out that  
496 is implemented by small evenly-distributed gaps at the rear ends of adjacent  
497 6-column groups (bundles). A total of 17 such bundles comprise the full Tagger  
498 Microscope.

499 The far ends of the scintillation light guides are coupled to Hamamatsu  
500 S10931-050P SiPMs. The SiPMs are mounted on a custom-built two-stage  
501 preamplifier board, with 15 SiPMs per board. In addition to the 15 individual  
502 signals generated by each preamplifier, the boards also produce three analog  
503 sum outputs, each the sum of five adjacent SiPMs corresponding to the five  
504 fibers in a single column. All 510 SiPMs are individually biased by custom bias

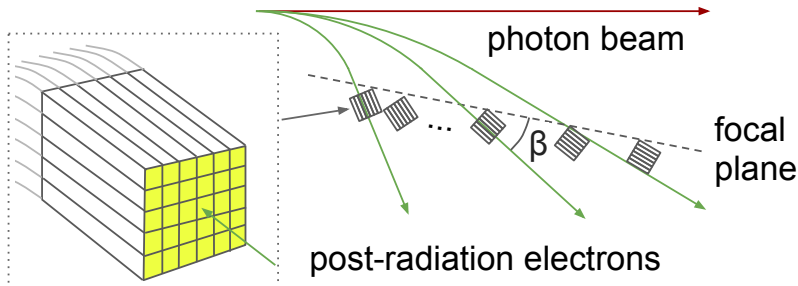


Figure 9: Conceptual overview of the tagger microscope design, showing the fiber bundles and light guides (left), and the orientation of these bundles aligned with the incoming electron beam direction in the tagger focal plane (right). The variation of the crossing angle  $\beta$  is exaggerated for the sake of illustration.

505 control boards, one for every two preamplifier boards. The control boards con-  
 506 nect to the preamplifiers over a custom backplane, and communicate with the  
 507 experimental slow controls system over ethernet. Each control board has the  
 508 capability to electronically select between two gain modes for the preamplifiers  
 509 on that board: a low gain mode used during regular tagging operation, and a  
 510 high gain mode used for triggering on single-pixel pulses during bias calibration.  
 511 Each bias control board manages the control and biasing for two preamplifiers.  
 512 The control board also measures live values for environmental parameters (volt-  
 513 age levels and temperatures) in the TAGM electronics, so that alarms can be  
 514 generated by the experimental control system whenever any of these parameters  
 515 stray outside predefined limits.

516 Pulse height and timing information for 122 channels from the TAGM is  
 517 provided by analog-to-digital converters (ADCs) and time-to-digital converters  
 518 (TDCs). These 122 signals include the 102 column sums plus the individual  
 519 fiber signals from columns 7, 27, 81, and 97. Here, each channels goes through  
 520 a 1:1 passive splitter, with one output going to an ADC and the other through  
 521 discriminators to a TDC. The ADCs are 250-MHz flash ADCs with 12-bit res-  
 522 olution and a full-scale pulse amplitude of 1 V. The TDCs are based on the F1  
 523 TDC chip [17], with a least-count of 62 ps. Pulse thresholds in both the ADC  
 524 and discriminator modules are programmable over the range 1-1000 mV on an  
 525 individual channel basis, covering the full dynamic range of the TAGM front  
 526 end. The TAGM preamplifier outputs (before splitting) saturate around 2 V  
 527 pulse amplitude.

528 The mean pulse charge in units of SiPM pixels corresponding to a single  
 529 high-energy electron varies from 150 to 300 pC, depending on the fiber, with  
 530 an average of 220 pC and standard deviation of 25 pC. During calibration, this  
 531 yield is measured individually for each fiber by selectively biasing the SiPMs on  
 532 each row of fibers, one row at a time, and reading out the column sums. Once

533 all 510 individual fiber yields have been measured, the bias voltages within each  
534 column are adjusted to compensate for yield variations, so that the mean pulse  
535 height in a given column is the same regardless of which fiber in the column  
536 detected the electron. The ADC readout and discriminator thresholds are set  
537 individually for each column, for optimum efficiency and noise rejection.

538 The ADC firmware provides an approximate time for each pulse, in addition  
539 to the pulse amplitude. During offline reconstruction, this time information  
540 is used to associate ADC and TDC pulse information from the same channel,  
541 so that a time-walk correction can be applied to the TDC time. Once this  
542 correction has been applied, a time resolution of 230 ps is achieved for the  
543 TAGM. This resolution is based on data collected at rates on the order of  
544 1 MHz per column, a factor of 2 lower than the 2.2 MHz peak rate anticipated  
545 during GLUEX 2 running. A brief test above 2 MHz per column allowed visual  
546 inspection of the pulse waveforms from the TAGM, without change in the pulse  
547 shape or amplitude. Given that the readout was designed to operate at rates  
548 up to 4 MHz per column without significant degradation in performance, the  
549 TAGM time resolution should be substantially unaffected by the increased beam  
550 intensity of GLUEX Phase 2.

#### 551 *2.4.3. Broadband tagging hodoscope*

552 The Tagger Hodoscope (TAGH) consists of 222 scintillator counters dis-  
553 tributed over a length of 9.25 m and mounted just behind the focal plane of  
554 the tagger magnet. The function of this hodoscope is to tag the full range in  
555 photon energy from 25% to 97% of the incident electron energy. A gap in the  
556 middle of that range is left open for the registration of the primary coherent  
557 peak by the Tagger Microscope. The geometry of the counters in the vicinity  
558 of the microscope is shown in Fig. 10. This broad coverage aids in alignment of  
559 the diamond radiator and expands the GLUEX physics program reach to photon  
560 energies outside the range of the coherent peak. The coverage of the hodoscope  
561 counters in the region below 60% drops to half, with substantial gaps in energy  
562 between the counters. This was done because the events of primary interest to  
563 GLUEX come from interactions of photons within and above the coherent peak;  
564 within and above the coherent peak the coverage is 100% up to the 97%  $E_0$   
565 cutoff.

566 Each counter in the hodoscope is a sheet of EJ-228 scintillator, 6 mm thick  
567 and 40 mm high. The counter widths vary along the focal plane, from 21 mm  
568 near the end-point region down to 3 mm at the downstream end. The scintil-  
569 lators are coupled to a Hamamatsu R9800 photomultiplier tube (PMT) via a  
570 cylindrical acrylic (UVT-PMMA) light guide 22.2 mm in diameter and 120 mm  
571 long. Each PMT is wrapped in  $\mu$ -metal to shield the tube from the fringe field  
572 of the tagger magnet.

573 Each PMT is instrumented with a custom designed active base [18], con-  
574 sisting of a high-voltage divider and an amplifier powered by current flowing  
575 through the divider. The base provides two signal outputs, one going to a flash  
576 ADC and the other through a discriminator to a TDC. Operating the amplifier  
577 with a gain factor of 8.5 allows the PMT to operate at a lower voltage of 900

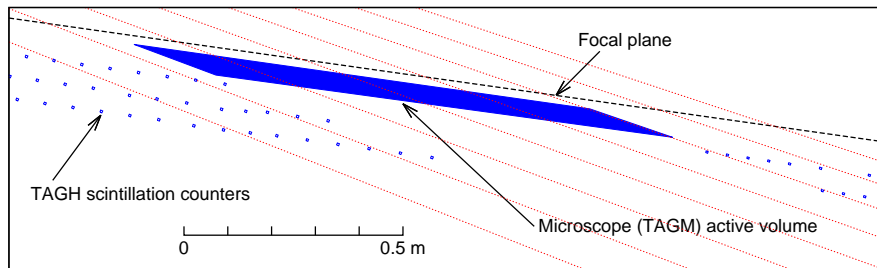


Figure 10: Schematic of electron trajectories in the region of the microscope. Shown are the three layers of hodoscope counters on either side of the microscope and the region covered by the microscope.

578 V and reduce the PMT anode current, therefore improving the rate capability.  
 579 The energy bite of each counter ranges between 8.5 and 30 MeV for a 12 GeV  
 580 incident electron beam. Typical rates during production running are 1 MHz  
 581 above the coherent peak and 2 MHz per counter below the coherent peak. The  
 582 maximum sustainable rate per counter is about 4 MHz.

583 The counters are mounted with their faces normal to the path of the scattered  
 584 electrons in two or three rows slightly downstream of the focal plane, as shown  
 585 in Fig. 10. This allows the counters to be positioned without horizontal gaps in  
 586 the dispersion direction, enabling complete coverage of the entire tagged photon  
 587 energy range.

588 The mounting frame of the hodoscope is suspended from the ceiling of the  
 589 Tagger Hall to provide full flexibility for positioning TAGH. The frame is con-  
 590 structed to also support the addition of counters to fill in the energy range  
 591 currently occupied by the microscope when the TAGM location is changed.

592 A similar procedure to that described above for the TAGM is used to apply  
 593 a time-walk correction to the TDC times from the TAGH counters. Once this  
 594 time-walk correction is applied, the time resolution of the TAGH is 200 ps.  
 595 No significant degradation of this resolution is expected at the operating rates  
 596 planned for Phase 2 running, which are on the order of 2 MHz per counter above  
 597 the coherent peak. Under these conditions, the rates in the TAGH counters  
 598 below the coherent peak would average around 4 Mhz, which is at the top of  
 599 their allowed range. These counters will be turned off when running at full  
 600 intensity.

### 601 2.5. Beam profiler

602 The beam profiler is located immediately upstream of the collimator (see  
 603 Fig. 4) and is used to measure the photon beam intensity in a plane normal to  
 604 the incident photon beam. The profiler consists of two planes of scintillating  
 605 fibers, giving information on the photon beam profile in the X and Y projections.  
 606 Each plane consists of 64 square fibers, 2 mm in width, read out by four 16-  
 607 channel multi-anode PMTs. The beam profiler is only used during beam setup  
 608 until the photon beam is centered on the active collimator.

609 *2.6. Active collimator*

610 The active collimator monitors the photon beam position and provides feed-  
611 back to micro-steering magnets in the electron beamline, for the purpose of  
612 suppressing drifts in photon beam position. The design of the active collimator  
613 for GLUEX is based on a device developed at SLAC for monitoring the coherent  
614 bremsstrahlung beam there [19]. The GLUEX active collimator is located on  
615 the upstream face of the primary collimator, and consists of a dense array of  
616 tungsten pins attached to tungsten base plates. The tungsten plate intercepts  
617 off-axis beam photons before they enter the collimator, creating an electromag-  
618 netic shower that cascades through the array of pins. High-energy delta rays  
619 created by the shower in the pins (known as “knock-ons”) are emitted forward  
620 into the primary collimator. The resulting net current between the tungsten  
621 plates and the collimator is proportional to the intensity of the photon beam on  
622 the plate. The tungsten plates are mounted on an insulating support, and the  
623 plate currents are monitored by a preamplifier with pA sensitivity.

624 The tungsten plate is segmented radially into two rings, and each ring is  
625 segmented azimuthally into four quadrants. The asymmetry of the induced  
626 currents on the plates in opposite quadrants indicate the degree of displacement  
627 of the photon beam from the intended center position. Typical currents on the  
628 tungsten sectors are at the level of 1.4 nA (inner ring) and 0.85 nA (outer ring)  
629 when running with a 50  $\mu\text{m}$  diamond crystal and a 200-nA incident electron  
630 beam current. The current-sensitive preamplifiers used with the active collimator  
631 are PMT-5R devices manufactured by ARI Corporation. The PMT-5R  
632 has six remotely selectable gain settings ranging from  $10^{12}$  V/A to  $10^6$  V/A,  
633 selectable by powers of 10. This provides an excellent dynamic range for operation  
634 of the beam over a wide range of intensities, from 1 nA up to several  $\mu\text{A}$ .  
635 The preamplifier input stage exhibits a fixed gain-bandwidth product of about  
636 2 Hz-V/pA which limits its bandwidth at the higher gain settings, for example  
637 2 Hz at  $10^{12}$  V/A, 20 Hz at  $10^{11}$  V/A.

638 In-situ electronic noise on the individual wedge currents is measured to be  
639  $1.5 \text{ pA}/\sqrt{\text{Hz}}$  on the inner ring, and  $15 \text{ pA}/\sqrt{\text{Hz}}$  on the outer ring. The sensi-  
640 tivity of the current asymmetry to position is 0.160/mm for the inner ring and  
641 0.089/mm for the outer. The electronic noise of the individual wedge currents  
642 is  $1.5 \text{ pA}/\sqrt{\text{Hz}}$  (inner ring) and  $15 \text{ pA}/\sqrt{\text{Hz}}$  (outer ring). With a 50 micron  
643 diamond and 200 nA beam current, operating the active collimator at a band-  
644 width of 1 kHz yields a measurement error in the position of the beam centroid  
645 of 150  $\mu\text{m}$  for the inner ring and 450  $\mu\text{m}$  for the outer ring. The purpose of  
646 the outer ring is to help locate the beam when the beam location has shifted  
647 more than 2 mm from the collimator axis, where the response of the inner ring  
648 sectors becomes nonlinear.

649 The maximum deviation allowed for the Hall D photon beam position rela-  
650 tive to the collimator axis is 200  $\mu\text{m}$ . The active collimator readout was designed  
651 with kHz bandwidth so that use in a fast feedback loop would suppress motion of  
652 the beam at 60 Hz and harmonics that might exceed this limit. Experience with  
653 the Hall-D beam has shown that the electron beam feedback systems already

654 suppresses this motion to less than 100  $\mu\text{m}$  amplitude, so that fast feedback  
655 using the active collimator is not required during normal operation. Instead,  
656 the active collimator is used in a slow feedback loop which locks the photon  
657 beam position at the collimator with a correction time constant of a few sec-  
658 onds. This slow feedback system is essential for preventing long-term drifts in  
659 the photon beam position that would otherwise occur on the time scale of hours  
660 or days. The active collimator can achieve 200  $\mu\text{m}$  position resolution down to  
661 beam currents as low as 2 nA when operated in this mode with noise averaging  
662 over a 5 s interval.

### 663 *2.7. Collimator*

664 The photon beam produced at the diamond radiator contains both inco-  
665 herent and coherent bremsstrahlung components. In the region of the coherent  
666 peak, where photon polarization is at its maximum, the angular spread of coher-  
667 ent bremsstrahlung photons is less than that of incoherent bremsstrahlung. The  
668 characteristic emission angle for incoherent bremsstrahlung is  $m/E = 43 \mu\text{rad}$   
669 at 12 GeV, whereas the coherent flux within the primary peak is concentrated  
670 below 15  $\mu\text{rad}$  with respect to the beam direction. Collimation increases the  
671 degree of linear polarization in the photon beam by suppressing the incoherent  
672 component relative to the coherent part.

673 The Hall-D primary collimator provides apertures of 3.4 mm and 5.0 mm in a  
674 tungsten block mounted on an X-Y table. The 5.0 mm collimator is used under  
675 normal GLUEX running conditions. The tungsten collimator is surrounded by  
676 lead shielding. The collimator may also be positioned to block the beam to  
677 prevent high-intensity beam from entering the experimental hall during tuning  
678 of the electron beam. Downstream of the primary collimator, a sweeping magnet  
679 and shield wall, followed by a secondary collimator with its sweeping magnet  
680 and shield wall, suppress charged particles and photon background around the  
681 photon beam that are generated in the primary collimator. The photon beam  
682 exiting the collimation system then passes through a thin pair conversion target.  
683 The resulting  $e^+e^-$  pairs are used to continuously monitor the photon beam flux  
684 and polarization.

### 685 *2.8. Triplet Polarimeter*

686 The Triplet Polarimeter (TPOL) is used to measure the degree of polariza-  
687 tion of the linearly-polarized photon beam [20]. The polarimeter uses the process  
688 of  $e^+e^-$  pair production on atomic electrons in a beryllium target foil, with the  
689 scattered atomic electrons measured using a silicon strip detector. Information  
690 on the degree of polarization of the photon beam is obtained by analyzing the  
691 azimuthal distribution of the scattered atomic electrons.

#### 692 *2.8.1. Determination of photon polarization*

693 Triplet photoproduction occurs when the polarized photon beam interacts  
694 with the electric field of an atomic electron within a target material and produces  
695 a high energy  $e^+e^-$  pair. When coupled with trajectory and energy information



696 of the  $e^+e^-$  pair, the azimuthal angular distribution of the recoil electron provides a measure of the photon beam polarization. The cross section for triplet  
697 photoproduction can be written as  $\sigma_t = \sigma_0[1 - P\Sigma \cos(2\varphi)]$  for a polarized photon  
698 beam, where  $\sigma_0$  is the unpolarized triplet cross section,  $P$  the photon beam  
699 polarization,  $\Sigma$  the beam asymmetry for the process, and  $\varphi$  the azimuthal angle  
700 of the recoil electron trajectory with respect to the plane of polarization for  
701 the incident photon beam. To determine the photon beam polarization, the  
702 azimuthal distribution of the recoil electrons is recorded and fit to the function  
703  $A[1 - B \cos(2\varphi)]$  where the variables  $A$  and  $B$  are parameters of the fit, with  
704  $B = P\Sigma$ . The value of  $\Sigma$  depends on the intensity profile of the photon beam,  
705 the thickness of the converter target, and the geometry of the setup. The value  
706 of  $\Sigma$  was determined to be  $0.1990 \pm 0.0008$  at 9 GeV for the GLUEX beamline  
707 and a 75 micron Be converter [20].

709 The TPOL detects the recoil electron arising from triplet photoproduction.  
710 This system consists of a converter tray and positioning assembly, which holds  
711 and positions a beryllium foil converter where the triplet photoproduction takes  
712 place. A silicon strip detector (SSD) detects the recoil electron from triplet  
713 photoproduction, providing energy and azimuthal angle information for that  
714 particle. A vacuum housing, containing the pair production target and SSD,  
715 supplies a vacuum environment minimizing multiple Coulomb scattering between  
716 target and SSD. Preamplifier and signal filtering electronics are placed  
717 within a Faraday-cage housing.

718 The preamplifier enclosure is lined with a layer of copper foil to reduce  
719 exterior electromagnetic signal interference. Signals from the downstream (az-  
720 imuthal sector) side of the SSD are fed to a charge-sensitive preamplifier located  
721 outside the vacuum. In operation, the TPOL vacuum box is coupled directly to  
722 the evacuated beamline through which the polarized photon beam passes.

723 Upon entering TPOL, the photon beam passes into the beryllium converter,  
724 triplet photoproduction takes place, an  $e^+e^-$  pair is emitted from the target in  
725 the forward direction, and a recoil electron ejected from the target at large angles  
726 with respect to the beam is detected by the SSD within the TPOL vacuum  
727 chamber. Upon entering TPOL, triplet photoproduction takes place in the  
728 beryllium converter where an  $e^+e^-$  pair is emitted in the forward direction. The  
729 recoil electron is ejected at large angles and detected by the SSD. The  $e^+e^-$   
730 pair, together with any beam photons that did not interact with the converter  
731 material, pass through the downstream port of the TPOL vacuum box into  
732 the evacuated beamline, which in turn passes through a shielding wall into  
733 the Hall-D experimental area. The  $e^+e^-$  pair then enters the vacuum box and  
734 magnetic field of the GLUEX Pair Spectrometer, while photons continue through  
735 an evacuated beamline to the target region of the GlueX detector. Accounting  
736 for all sources of uncertainty from this setup, the total estimated systematic  
737 error in the TPOL asymmetry  $\Sigma$  is 1.5% [20].

### 738 *2.9. Pair Spectrometer*

739 The main purpose of the Pair Spectrometer (PS) [21] is to measure the  
740 spectrum of the collimated photon beam and determine the fraction of linearly

741 polarized photons in the coherent peak energy region. The TPOL relies on the  
742 PS to trigger on pairs in coincidence with hits in the recoil detector. The PS  
743 is also used to monitor the photon beam flux, and for energy calibration of the  
744 tagging hodoscope and microscope detectors.

745 The PS, located at the entrance to Hall D, reconstructs the energy of a  
746 beam photon by detecting the  $e^+e^-$  pair produced by the photon in a thin  
747 converter. The converter used is typically the beryllium target housed within  
748 TPOL; otherwise the PS has additional converters that may be inserted into the  
749 beam with thicknesses ranging between 0.03% and 0.5% of a radiation length.  
750 The produced  $e^+e^-$  leptons are deflected in a modified 18D36 dipole magnet  
751 with an effective field length of about 0.94 m and detected in two layers of  
752 scintillator detectors: a high-granularity hodoscope and a set of coarse counters,  
753 referred to as PS and PSC counters, respectively. The detectors are partitioned  
754 into two identical arms positioned symmetrically on opposite sides of the photon  
755 beam line. The PSC consists of sixteen scintillator counters, eight in each  
756 detector arm. Each PSC counter is 4.4 cm wide and 2 cm thick in the direction  
757 along the lepton trajectory and 6 cm high. Light from the PSC counters is  
758 detected using Hamamatsu R6427-01 PMTs. The PS hodoscope consists of 145  
759 rectangular tiles (1 mm and 2 mm wide) stacked together. Hamamatsu SiPMs  
760 were chosen for readout of the PS counters [22, 23, 24].

761 Each detector arm covers an  $e^\pm$  momentum range between 3.0 GeV/c and  
762 6.2 GeV/c, corresponding to reconstructed photon energies between 6 GeV and  
763 12.4 GeV. The relatively large acceptance of the hodoscope enables energy de-  
764 termination for photons with energies from below the coherent peak to the beam  
765 endpoint energy near 12 GeV.

766 The pair energy resolution of the PS hodoscope is about 25 MeV. The time  
767 resolution of the PSC counters is 120 ps, which allows coincidence measurements  
768 between the tagging detectors and the PS within an electron beam bunch. Sig-  
769 nals from the PS detector are delivered to the trigger system, as described in  
770 Section 9. The typical rate of PS double-arm coincidences is a few kHz. Details  
771 about the performance of the spectrometer are given in [25, 26].

### 772 *2.9.1. Determination of photon flux*

773 The intensity of beam photons incident on the GLUEX target is important for  
774 the extraction of cross sections. The photon flux is determined by converting a  
775 known fraction of the photon beam to  $e^\pm$  pairs and counting them in the PS as a  
776 function of energy. Data from the PS are collected using a PS trigger, which runs  
777 in parallel to the main GLUEX physics trigger, as described in Section 9. The  
778 number of beam photons integrated over the run period is obtained individually  
779 for each tagger counter (TAGH and TAGM), i.e., for each photon beam energy  
780 bin.

781 The PS calibration parameter used in the flux determination, a product  
782 of the converter thickness, acceptance, and the detection efficiency for lep-  
783 tons, is determined using calibration runs with the Total Absorption Counter  
784 (TAC) [27]. The TAC is a small calorimeter (see Section 2.10) inserted directly  
785 into the photon beam to count the number of beam photons as a function of

786 energy. These absolute-flux calibration runs are performed at reduced beam  
787 intensities in order to limit the rate of accidental tagging coincidences. Data  
788 are acquired simultaneously from the PS and TAC. These data enable an abso-  
789 lute flux calibration for the PS by measuring the number of reconstructed  $e^+e^-$   
790 pairs for a given number of photons of the same energy seen by the TAC. Un-  
791 certainties on the photon flux determinations are currently being investigated.  
792 The expected precision of the flux determination is on the level of 1%.

### 793 *2.10. Total Absorption Counter*

794 Only a certain fraction of the photons produced at the radiator reach the  
795 target and causes an interaction that is seen in the GLUEX detector. The frac-  
796 tion of tagged photons reaching the GLUEX target is determined as a function  
797 of energy from individual TAC coincidence measurements with each tagging  
798 counter. These “tagging fractions” are used to scale the counts measured in  
799 the PS in order to obtain the total tagged flux that reached the GlueX target  
800 during a given run period.

801 The TAC is a high-efficiency lead-glass calorimeter, used at low beam cur-  
802 rents ( $< 5\text{nA}$ ) to determine the overall normalization of the flux from the GLUEX  
803 coherent bremsstrahlung facility. Using the device at normal GLUEX produc-  
804 tion currents is not possible, as it would be overwhelmed with rate and would  
805 very quickly succumb to radiation damage. Therefore, the TAC is only inserted  
806 into the beam during dedicated runs at very low intensities where the detector  
807 can run with near 100% efficiency. The TAC was originally developed for and  
808 deployed in Hall B, for photon beam operations with CLAS [28, 29, 30] .

## 809 **3. Solenoid magnet**

### 810 *3.1. Overview*

811 The core of the GlueX spectrometer is a superconducting solenoid magnet  
812 with a bore of about 2 m in diameter and with an overall yoke length of about  
813 4.8 m. The photon beam passes along the axis of the solenoid. At the nominal  
814 current of 1350 A, the magnet provides a magnetic field along the axis of about  
815 2 T.

816 The magnet was designed and built at SLAC in the early 1970’s [31] for the  
817 LASS spectrometer [32]. The solenoid employs a cryostatically stable design  
818 with cryostats designed to be opened and serviced with hand tools. The magnet  
819 was refurbished and modified<sup>29</sup> for the GLUEX experiment [33, 34].

820 The magnet is constructed of four separate superconducting coils and cryo-  
821 stats. The flux return yoke is made of several iron rings. The coils are connected

---

<sup>29</sup> The front plate of the flux return yoke was modified, leading to a swap of the two front coils and modifications of the return flux yoke in order to keep the magnetic forces on the front coil under the design limit. The original gaps between the yoke’s rings were filled with iron. The Cryogenic Distribution Box was designed and built for GLUEX.

822 in series. A common liquid helium tank is located on top of the magnet, pro-  
 823 viding a gravity feed of the liquid to the coils. The layout of the coil cryostats  
 824 and the flux return iron yoke is shown in Fig. 3. Table 3 summarizes the salient  
 825 parameters of the magnet.

Inside diameter of coils	2032 mm
Clear bore diameter	1854 mm
Overall length along iron	4795 mm
Inside iron diameter	2946 mm
Outside iron diameter	3759 mm
Original yoke, cast and annealed - steel	AISI 1010
Added filler plates - steel	ASTM A36
Full weight	284 t
Full number of turns	4608
Number of separate coils	4
Turns per coil 2	928
Turns per coil 1	1428
Turns per coil 3	776
Turns per coil 4	1476
Total conductor weight	13.15 t
Coil resistance at $\sim 300$ K	15.3 $\Omega$
Coil resistance at $\sim 10$ K	$\sim 0.15\Omega$
Design operational current	1500 A
Nominal current (actual)	1350 A
Maximal central field at 1350 A	2.08 T
Inductance at 1350 A	26.4 H
Stored energy at 1350 A	24.1 MJ
Protection circuit resistor	0.061 $\Omega$
Coil cooling scheme	helium bath
Total liquid helium volume	3200 $\ell$
Operating temperature (actual)	4.5 K
Refrigerator liquefaction rate at 0 A	1.7 g/s
Refrigerator liquefaction rate at 1350 A	2.7 g/s

Table 3: Key parameters of the GLUEX solenoid. The coils are listed in order along the beam direction.

### 826 3.2. Conductor and Coils

827 The superconductor composite is made of niobium–titanium filaments in a  
 828 copper substrate, twisted and shaped into a  $\sim 7.62 \times 1$  mm<sup>2</sup> rectangular band.  
 829 The laminated conductor is made by soldering the superconductor compos-  
 830 ite band between two copper strips to form a rectangular cross section of  
 831  $7.62 \times 5.33$  mm<sup>2</sup>. The measured residual resistivity ratio of the conductor at  
 832  $\sim 300^\circ\text{K}$  and  $\sim 15^\circ\text{K}$  is  $\approx 100$ .

833 As the coil was wound, a 0.64 mm-thick stainless steel support band and  
 834 two 0.2 mm-thick Mylar insulating strips were wound together with it for pre-

835 tensioning and insulation. The liquid helium is in contact with the shorter  
836 (5.33 mm) sides of the cable.

837 Each of the coils consists of a number of subcoils. Each subcoil contains  
838 a number of “double pancakes” with the same number of turns. Each double  
839 pancake is made from a single piece of conductor. The voltage across the subcoils  
840 is monitored using special wires passing through the coils’ chimneys along with  
841 the helium supply pipes and the main conductor.

842 The cold helium vessel containing the coil is supported within the warm  
843 cryostat vacuum vessel by a set of columns designed to provide sufficient thermal  
844 insulation. The columns are equipped with strain gauges for monitoring the  
845 stresses on the columns. The helium vessel is surrounded by a nitrogen-cooled  
846 thermal shield made of copper and stainless-steel panels. Super-insulation is  
847 placed between the vacuum vessel and the nitrogen shield. The vacuum vessels  
848 are attached to the matching iron rings of the yoke.

849 The power supply<sup>30</sup> provides up to 10 V DC for establishing the operating  
850 current while ramping. The supply also includes a protection circuit, which  
851 can be engaged by a quench detector as well as by other signals. During trips,  
852 a small dump resistor of 0.061  $\Omega$  limits the maximum voltage on the magnet  
853 to 100 V. The dumping time constant of  $L/R \approx 7$  min is relatively long, but  
854 safe according to the original design of the magnet. A large copper mass and  
855 the helium bath are able to absorb a large amount of energy during a quench  
856 without overheating the solder joints. This permits the use of an “intelligent”  
857 quench detector with low noise sensitivity and a relatively slow decision time  
858 of 0.5 s. The quench detector compares the measured voltages on different  
859 subcoils in order to detect a resistive component. While ramping the current,  
860 such a voltage is proportional to the subcoil inductance. Relative values of  
861 inductance of various subcoils depend on the value of the current because of  
862 saturation effects in the iron yoke. Transient effects are also present at changes  
863 of the slew rate caused by Foucault currents in the yoke. The system includes  
864 two redundant detectors: one uses analog signals and a simplified logic, another  
865 is part of the PLC control system (see Section 3.4) which uses digitized signals.  
866 The PLC digital programmable device is more sensitive since this monitoring  
867 system takes into account the dependence of the coils’ inductance on the current  
868 and provides better noise filtering. The ramping slew rate is limited by the  
869 transient imbalance of the voltages on subcoils that may trigger the quench  
870 detector. Additionally, unexplained voltage spikes of 1 ms duration have been  
871 observed in coil 2 at high slew rates, which can trigger the quench detector.  
872 Powering up the magnet to 1350 A takes about 8 h.

873 For diagnostic purposes two 40-turn pickup coils are installed on the bore  
874 surface of the vacuum vessel of each of the coils.

---

<sup>30</sup>Danfysik System 8000 Type 854.

875 *3.3. Cooling System*

876 The cooling system is described in detail in Ref. [35]. A stand-alone helium  
877 refrigerator located in a building adjacent to Hall D provides liquid helium and  
878 nitrogen via a transfer line to the Cryogenic Distribution Box above the magnet.  
879 The transfer line delivers helium at 2.6 atm and 6 K to a Joule-Thomson (JT)  
880 valve providing liquid to a cylindrical common helium tank in the Distribution  
881 Box. The level of liquid helium in the tank is measured with a superconducting  
882 wire probe;<sup>31</sup> the liquid level is kept at about half of the tank diameter. The  
883 cold helium gas from the tank is returned to the refrigerator, which keeps the  
884 pressure at the top of the tank at 1.2 atm corresponding to about 4.35 K at  
885 the surface of the liquid.<sup>32</sup> Each coil is connected to the common helium tank  
886 by two vertical 2-inch pipes. One pipe is open at the bottom of the tank while  
887 the other one is taller than the typical level of helium inside the tank. The  
888 main conductor and the wires for voltage monitoring pass through the former  
889 pipe. Additionally, two  $\sim 6$  m long, 3/8 inch ID pipes go outside the coil's  
890 helium vessel, from the Distribution Box to the bottom of the coil. One of those  
891 pipes, connected to a JT valve in the box, is used to fill the coil initially, but is  
892 not used during operation. The other pipe reaches the bottom of the common  
893 helium tank in order to provide a thermo-syphon effect essential for the proper  
894 circulation of helium in the coil. The main current is delivered into the helium  
895 tank via vapor-cooled leads, and is distributed to the coils by a superconducting  
896 cable. After cooling the leads, the helium gas is warmed and returned to the  
897 refrigeration system. The gas flow through the leads is regulated based on the  
898 current in the magnet; at 1350 A, the flow is about 0.25 g/s. The coils and the  
899 Distribution Box are equipped with various sensors for temperature, pressure,  
900 voltage, and flow rates.

901 *3.4. Measurements and Controls*

902 The control system for the superconducting solenoid, power supply, and  
903 cryogenic system, is based on Programmable Logic Controllers (PLC)<sup>33</sup>. The  
904 PLC system digitizes the signals from various sensors, communicates with other  
905 devices, reads out the data into a programmable unit for analysis, and sends  
906 commands to various devices. Additionally, the PLC is connected to EPICS<sup>34</sup>  
907 in order to display and archive the data (see Section 11). The practical sampling  
908 limit for the readout of the sensor is a few Hz, which is too low for detection of  
909 fast voltage spikes on the coils due to motion, shorts, or other effects. There-  
910 fore, the voltage taps from the coils and the pickup coils are read out by a

---

<sup>31</sup> American Magnetics Model 1700 with HS-1/4-RGD-19"/46"-4LDCP-LL6-S sensor

<sup>32</sup> The original implementation at SLAC did not recycle the helium and operated at atmospheric pressure.

<sup>33</sup> Allen-Bradley Programmable Logic Controllers <http://ab.rockwellautomation.com/Programmable-Controllers>.

<sup>34</sup> Experimental Physics and Industrial Control System, <https://epics.anl.gov>.

911 PXI<sup>35</sup> system, which provides a sampling rate of about 100 kHz. The PXI sys-  
912 tem also reads out several accelerometers attached to the coils' chimneys, which  
913 can detect motion inside the coils. The PXI CPU performs initial integration  
914 and arranges the data in time-wise rows with a sampling rate of 10 kHz. The  
915 PLC system reads out the data from the PXI system. Additionally, the PXI  
916 data are read out by an EPICS server at the full 10 kHz sampling rate and are  
917 recorded for further analysis.

### 918 3.5. Field calculation and measurement

919 The momentum resolution of the GLUEX spectrometer is larger than 1%  
920 and is dominated by multiple scattering and the spatial resolution of the co-  
921 ordinate detectors. Thus, a fraction of a percent is sufficient accuracy for the  
922 field determination. The coils are axially symmetric, while the flux return yoke  
923 is nearly axially symmetric, apart from the holes for the coil's chimneys. The  
924 field was calculated using a 2-dimensional field calculator *Poisson/Superfish*<sup>36</sup>,  
925 assuming axial symmetry. The model of the magnet included the fine structure  
926 of the subcoils and the geometry of the yoke iron. Different assumptions about  
927 the magnetic properties of the yoke iron have been used: the *Poisson* default  
928 AISI 1010 steel, the measurements of the original yoke iron made at SLAC, and  
929 the 1018 steel used for the filler plates. Since the results of the field calculations  
930 differ by less than 0.1%, the default *Poisson* AISI 1010 steel properties were  
931 used for the whole yoke iron in the final field map calculations.

932 The three projections of the magnetic field have been measured along lines  
933 parallel to the axis, at four values of the radius and at up to six values of  
934 the azimuthal angle. The calculated field and the measured deviations are  
935 shown in Fig. 11. The tracking detectors occupy the volume of  $R < 56$  cm  
936 and  $45 < Z < 340$  cm. In this volume the field deviation at  $R = 0$  does not  
937 exceed 0.2%. The largest deviation of 1.5% is observed at the downstream edge  
938 of the fiducial volume and at the largest radius. Such a field uncertainty in  
939 that region does not noticeably affect the momentum resolution. In most of the  
940 fiducial volume the measured field is axially symmetric to  $\approx 0.1\%$  and deviates  
941 from this symmetry by  $\approx 2\%$  at the downstream edge and the largest radius.

942 The calculated field map is used for track reconstruction and physics analy-  
943 ses.

## 944 4. Target

945 A schematic diagram of the GLUEX liquid hydrogen cryotarget is shown in  
946 Fig. 12. The major components of the system are a pulse tube cryocooler,<sup>37</sup>  
947 a condenser, and a target cell. These items are contained within an aluminum

---

<sup>35</sup> National Instruments, PXI Platform, <http://www.ni.com/pxi/>.

<sup>36</sup> Poisson/Superfish developed at LANL, [https://laacg.lanl.gov/laacg/services/serv\\_codes.phtml#ps](https://laacg.lanl.gov/laacg/services/serv_codes.phtml#ps).

<sup>37</sup> Cryomech model PT415.

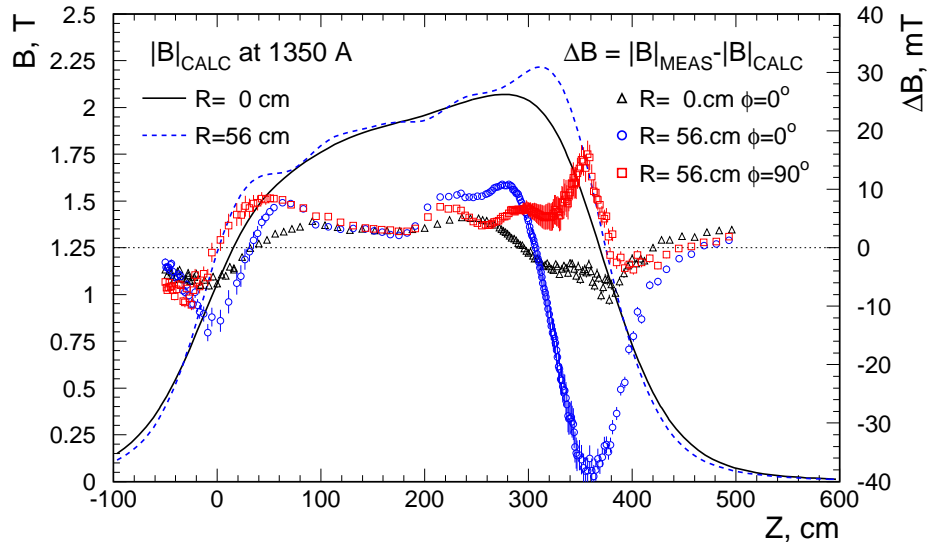


Figure 11: The full field at 1350 A calculated with *Poisson* (left scale) on the axis and at the edge of the tracking fiducial volume ( $R=56$  cm). The deviations of the measurements from the calculations are shown (right scale) on the axis, and at  $R=56$  cm. The measurements were made at 6 azimuthal angles. We show the angles ( $0^\circ$  and  $90^\circ$ ) with the largest deviations from the calculations.

948 and stainless steel ‘L’-shaped vacuum chamber with an extension of closed-cell  
 949 foam<sup>38</sup> surrounding the target cell. In turn, the GLUEX Start Counter (Sec. 8.1)  
 950 surrounds the foam chamber and is supported by the horizontal portion of the  
 951 vacuum chamber. Polyimide foils, 100  $\mu\text{m}$  thick, are used at the upstream and  
 952 downstream ends of the chamber as beam entrance and exit windows. The  
 953 entire system, including the control electronics, vacuum pumps, gas-handling  
 954 system, and tanks for hydrogen storage, are mounted on a small cart that is  
 955 attached to a set of rails for insertion into the GLUEX solenoid. To satisfy  
 956 flammable gas safety requirements, the system is connected at multiple points  
 957 to a nitrogen-purged ventilation pipe that extends outside Hall D.

958 Hydrogen gas is stored inside two 200 l tanks and is cooled and condensed  
 959 into a small copper and stainless steel container, the condenser, that is thermally  
 960 anchored to the second cooling stage of the cryocooler. The first stage of the  
 961 cryocooler is used to cool the  $\text{H}_2$  gas to about 50 K before it enters the condenser.  
 962 The first stage also cools a copper thermal shield that surrounds all lower-  
 963 temperature components of the system except for the target cell itself, which is  
 964 wrapped in a few layers of aluminized-mylar/cerex insulation.

965 The condenser is comprised of a copper C101 base sealed to a stainless steel

<sup>38</sup>Rohacell 110XT, Evonik Industries AG.



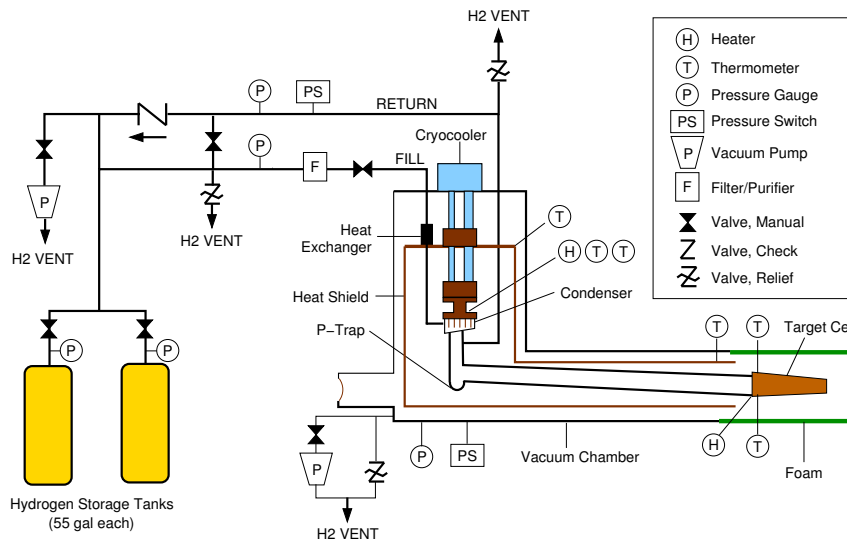


Figure 12: Simplified process and instrumentation diagram for the GlueX liquid hydrogen target (not to scale). In the real system, the P-trap is above the level of the target cell and is used to promote convective cooling of the target cell from room temperature.

966 can with an indium O-ring. Numerous vertical fins are cut into the copper base,  
 967 giving a large surface area for condensing hydrogen gas. A heater and a pair of  
 968 calibrated Cernox thermometers<sup>39</sup> are attached outside the condenser, and are  
 969 used to regulate the heater temperature when the system is filled with liquid  
 970 hydrogen.

971 The target cell, shown in Fig. 13, is similar to designs used in Hall B at  
 972 JLab [36]. The cell walls are made from 100- $\mu\text{m}$ -thick aluminized polyimide  
 973 sheet wrapped in a conical shape and glued along the edge, overlapping in a  
 974 2 mm wide scarf joint. The conical shape prevents bubbles from collecting  
 975 inside the cell, while the scarf joint reduces the stress riser at the glue joint.  
 976 This conical tube is glued to an aluminum base, along with stainless steel fill  
 977 and return tubes leading to the condenser, a feed-through for two calibrated  
 978 Cernox thermometers inside the cell, and a polyamide-imide support for the  
 979 reentrant upstream beam window. Both the upstream and downstream beam  
 980 windows are made of non-aluminized, 100  $\mu\text{m}$  thick polyimide films that have  
 981 been extruded into the shapes indicated in Fig. 13. These windows are clearly  
 982 visible in Fig. 20 where reconstructed vertex positions are shown. All items are  
 983 glued together using a two-part epoxy<sup>40</sup> that has been in reliable use at cryogenic  
 984 temperatures for long periods. A second heater, attached to the aluminum base,

<sup>39</sup>Cernox, Lake Shore Cryotronics.

<sup>40</sup>3M Scotch-Weld epoxy adhesive DP190 Gray.

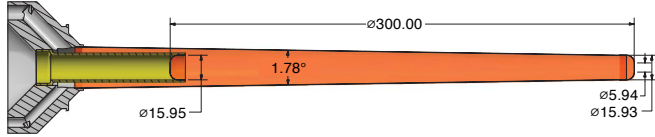


Figure 13: Target cell for the liquid hydrogen target. Dimensions are in mm.

985 is used to empty the cell for background measurements. The base is attached  
 986 to a kinematic mount, which is in turn supported inside the vacuum chamber  
 987 using a system of carbon fiber rods. The mount is used to correct the pitch  
 988 and yaw of the cell, while  $X$ ,  $Y$ , and  $Z$  adjustments are accomplished using  
 989 positioning screws on the target cart.

990 During normal operation, a sufficient amount of hydrogen gas is condensed  
 991 from the storage tanks until the target cell, condenser, and interconnecting  
 992 piping are filled with liquid hydrogen and an equilibrium pressure of about  
 993 19 psia is achieved. The condenser temperature is regulated at 18 K, while  
 994 the liquid in the cell cools to about 20.1 K. The latter temperature is 1 K  
 995 below the saturation temperature of  $H_2$ , which eliminates boiling within the  
 996 cell and permits a more accurate determination of the fluid density,  $71.2 \pm$   
 997  $0.3 \text{ mg/cm}^3$ . The system can be cooled from room temperature and filled with  
 998 liquid hydrogen in approximately six hours. Prior to measurements using an  
 999 empty target cell, the liquid hydrogen is boiled back into the storage tanks in  
 1000 about five minutes.  $H_2$  gas continues to condense and drain towards the target  
 1001 cell, but the condensed hydrogen is immediately evaporated by the cell heater.  
 1002 In this way, the cell does not warm above 40 K and can be re-filled with liquid  
 1003 hydrogen in about twenty minutes.

1004 Operation of the cryotarget is highly automated, requires minimal user inter-  
 1005 vention, and has operated in a very reliable and predictable manner throughout  
 1006 the experiment. The target controls<sup>41</sup> are handled by a LabVIEW program,  
 1007 while a standard EPICS softIOC running in Linux provides a bridge between  
 1008 the controller and JLab's EPICS environment (see Section 11). Temperature  
 1009 read back and control of the condenser and target cell thermometers are man-  
 1010 aged by a four-input temperature controller<sup>42</sup> with PID control loops of 50 and  
 1011 100 W. Strain gauge pressure sensors measure the fill and return pressures with  
 1012 0.25% accuracy. When filled with subcooled liquid, the long-term tempera-  
 1013 ture ( $\pm 0.2 \text{ K}$ ) and pressure ( $\pm 0.1 \text{ psi}$ ) stability of the liquid hydrogen enable a  
 1014 determination of the density to better than 0.5%.

<sup>41</sup>The control logic uses National Instruments CompactRIO 9030.

<sup>42</sup>Lake Shore Model 336.

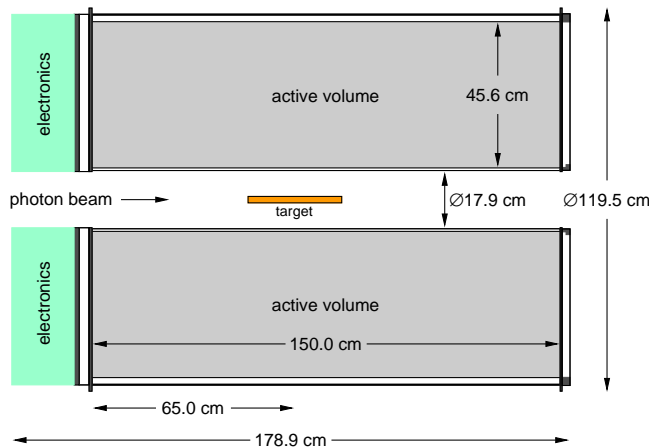


Figure 14: Cross-section through the cylindrically symmetric Central Drift Chamber, along the beamline.

## 1015 5. Tracking detectors

### 1016 5.1. Central drift chamber

1017 The Central Drift Chamber (CDC) is a cylindrical straw-tube drift chamber  
 1018 which is used to track charged particles by providing position, timing and energy  
 1019 loss measurements [37, 38]. The CDC is situated inside the Barrel Calorimeter,  
 1020 surrounding the target and Start Counter. The active volume of the CDC  
 1021 is traversed by particles coming from the hydrogen target with polar angles  
 1022 between  $6^\circ$  and  $168^\circ$ , with optimum coverage for polar angles between  $29^\circ$   
 1023 and  $132^\circ$ . The CDC contains 3522 anode wires of  $20\ \mu\text{m}$  diameter gold-plated  
 1024 tungsten inside Mylar<sup>43</sup> straw tubes of diameter 1.6 cm in 28 layers, located in  
 1025 a cylindrical volume which is 1.5 m long, with an inner radius of 10 cm and  
 1026 outer radius of 56 cm, as measured from the beamline. Readout is from the  
 1027 upstream end. Fig. 14 shows a schematic diagram of the detector.

1028 The straw tubes are arranged in 28 layers; 12 layers are axial, and 16 layers  
 1029 are at stereo angles of  $\pm 6^\circ$  to provide position information along the beam  
 1030 direction. The stereo angle was chosen to balance the extra tracking information  
 1031 provided by the unique combination of stereo and axial straws along a trajectory  
 1032 against the size of the unused volume inside the chamber at each transition  
 1033 between stereo and axial layers. Fig. 15 shows the CDC during construction.

1034 The volume surrounding the straws is enclosed by an inner cylindrical wall  
 1035 of 0.5 mm G10 fiberglass, an outer cylindrical wall of 1.6 mm aluminum, and  
 1036 two circular endplates. The upstream endplate is made of aluminum, while the  
 1037 downstream endplate is made of carbon fiber. The endplates are connected by 12

<sup>43</sup>[www.mylar.com](http://www.mylar.com)



Figure 15: The Central Drift Chamber during construction. A partially completed layer of stereo straw tubes is shown, surrounding a layer of straw tubes at the opposite stereo angle. Part of the carbon fiber endplate, two temporary tension rods and some of the 12 permanent support rods linking the two endplates can also be seen.

1038 aluminum support rods. Holes milled through the endplates support the ends of  
1039 the straw tubes, which were glued into place using several small components per  
1040 tube, described more fully in [38]. These components also support the anode  
1041 wires, which were installed with 30 g tension. At the upstream end, these  
1042 components are made of aluminum and were glued in place using conductive  
1043 epoxy<sup>44</sup>. This attachment method provides a good electrical connection to the  
1044 inside walls of the straw tubes, which are coated in aluminum. The components  
1045 at the downstream end are made of Noryl plastic<sup>45</sup> and were glued in place using  
1046 conventional non-conductive epoxy<sup>46</sup>. The materials used for the downstream  
1047 end were chosen to be as lightweight as feasible so as to minimize the energy  
1048 loss of charged particles passing through them.

1049 At each end of the chamber, a cylindrical gas plenum is located outside the  
1050 endplate. The gas supply runs in 12 tubes through the volume surrounding the  
1051 straws into the downstream plenum. There the gas enters the straws and flows  
1052 through them into the upstream plenum. From the upstream plenum the gas  
1053 flows into the volume surrounding the straws, and from there the gas exhausts  
1054 to the outside, bubbling through small jars of mineral oil. The gas mixture  
1055 used is 50% argon and 50% carbon dioxide at atmospheric pressure. This gas  
1056 mixture was chosen since its drift time characteristics provide good position

---

<sup>44</sup>TIGA 920-H, [www.loctite.com](http://www.loctite.com)

<sup>45</sup>[www.sabic.com](http://www.sabic.com)

<sup>46</sup>3M Scotch-Weld DP460NS, [www.3m.com](http://www.3m.com)

1057 resolution [37]. A small admixture (approximately 1%) of isopropanol is used  
1058 to prevent loss of performance due to aging[39, 40]. Five thermocouples are  
1059 located in each plenum and used to monitor the temperature of the gas. The  
1060 downstream plenum is 2.54 cm deep, with a sidewall of ROHACELL<sup>47</sup> and a  
1061 final outer wall of aluminized Mylar film, and the upstream plenum is 3.18 cm  
1062 deep, with a polycarbonate sidewall and a polycarbonate disc outer wall.

1063 The readout cables pass through the polycarbonate disc and the upstream  
1064 plenum to reach the anode wires. The cables are connected in groups of 20 to 24  
1065 to transition boards mounted onto the polycarbonate disc; the disc also support  
1066 the connectors for the high-voltage boards. Preamplifiers [41] are mounted  
1067 on the high-voltage boards. The aluminum endplate, outer cylindrical wall of  
1068 the chamber, aluminum components connecting the straws to the aluminum  
1069 endplate and the inside walls of the straws are all connected to a common  
1070 electrical ground. The anode wires are held at +2.1 kV during normal operation.

## 1071 *5.2. Forward Drift Chamber*

1072 The Forward Drift Chamber (FDC) consists of 24 disk-shaped planar drift  
1073 chambers of 1 m diameter. They are grouped into four packages inside the bore  
1074 of the spectrometer magnet. Forward tracking requires good multi-track separa-  
1075 tion due to the high particle density in the forward region. This is achieved  
1076 via additional cathode strips on both sides of the wire plane allowing for a  
1077 reconstruction of a space point on the track from each chamber. The FDC reg-  
1078 isters particles emitted into polar angles as low as 1° and up to 10° with all the  
1079 chambers, while having partial coverage up to 20°.

1080 One FDC chamber consists of a wire plane with cathode planes on either  
1081 sides at a distance of 5 mm from the wires (Fig. 16). The frame that holds the  
1082 wires is made out of ROHACELL with a thin G10 fiberglass skin in order to  
1083 minimize the material and allow low energy photons to be detected in the outer  
1084 electromagnetic calorimeters.

1085 The wire plane has sense (20  $\mu\text{m}$  diameter) and field (80  $\mu\text{m}$ ) wires 5 mm  
1086 apart, forming a field cell of  $10 \times 10 \text{ mm}^2$ . To reduce the effects of the magnetic  
1087 field, a “slow” gas mixture of 40% Ar and 60% CO<sub>2</sub> is used. A positive high  
1088 voltage of about 2.2 kV is applied to the sense wires and a negative high voltage  
1089 of 0.5 kV to the field wires. The cathodes are made out of 2- $\mu\text{m}$ -thin copper  
1090 strips on Kapton foil with a pitch of 5 mm, and are held at ground potential.  
1091 The strips on the two cathodes are arranged at 30° relative to each other and  
1092 at angles of 75° and 105° angle with respect to the wires.

1093 The six chambers of a package are separated by thin aluminized Mylar. Each  
1094 chamber is rotated relative to the previous one by 60°. The total material of a  
1095 package in the sensitive area corresponds to 0.43% radiation lengths, with about  
1096 half of that in the area along the beam line that has no copper on the cathodes.  
1097 The sense wires in the inner area of 6 – 7.8 cm diameter (depending on the  
1098 distance of the package to the target) are increased in thickness from 20  $\mu\text{m}$

---

<sup>47</sup>www.rohacell.com

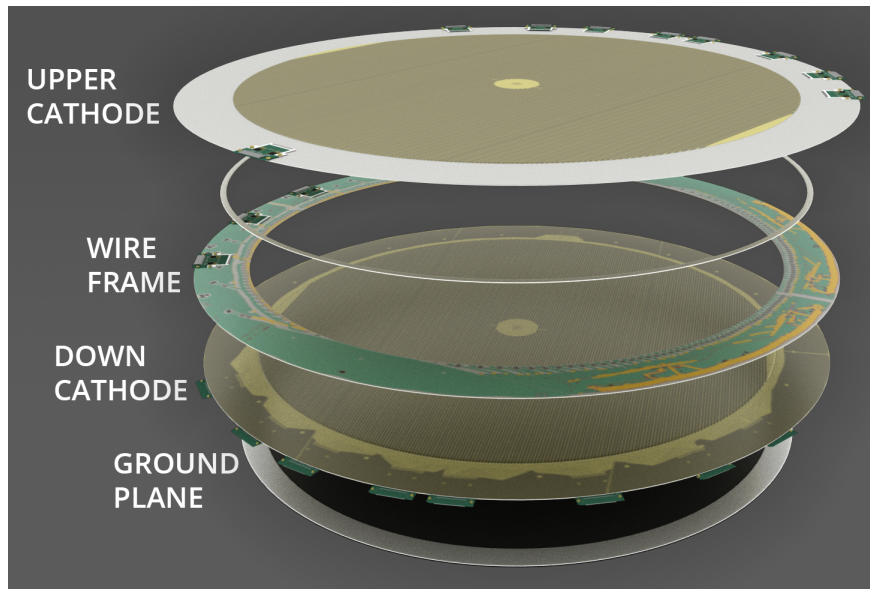


Figure 16: Artist rendering of one FDC chamber showing components. From top to bottom: upstream cathode, wire frame, downstream cathode, ground plane that separates the chambers. The diameter of the active area is 1 m.

1099 to  $\sim 80 \mu\text{m}$ , which makes them insensitive to the high rates along the beam.  
 1100 The distance between the first and last package is 1.69 m. All chambers are  
 1101 supplied with gas in parallel. In total, 2,304 wires and 10,368 strips are read  
 1102 using charge preamplifiers with 10 ns peaking time, with a gain of 0.77 mV/fC  
 1103 for the wires and 2.6 mV/fC for the strips.

### 1104 5.3. Electronics

1105 The high voltage (HV) supply units used are CAEN A1550P<sup>48</sup>, with noise-  
 1106 reducing filter modules added to each crate chassis. The low voltage (LV) sup-  
 1107 plies are Wiener MPOD MPV8008<sup>49</sup>. The preamplifiers are a custom JLab  
 1108 design based on an ASIC [41] with 24 channels per board; the preamplifiers are  
 1109 charge-sensitive, capacitively coupled to the wires in the CDC and FDC, and  
 1110 directly coupled to strips in the FDC.

1111 Pulse information from the CDC anode wires and FDC cathode strips are  
 1112 obtained and read out using 72-channel 125 MHz flash ADCs (FADCs) [42, 43].  
 1113 These use Xilinx<sup>50</sup> Spartan-6 FPGAs (XC6SLX25) for signal digitization and  
 1114 data processing with 12 bit resolution. Each FADC receives signals from three

<sup>48</sup>[www.caen.it](http://www.caen.it)

<sup>49</sup>[www.wiener-d.com](http://www.wiener-d.com)

<sup>50</sup>[www.xilinx.com](http://www.xilinx.com)

1115 preamplifiers. The signal cables from different regions of the drift chambers are  
1116 distributed between the FADCs in order to share out the processing load as  
1117 evenly as possible.

1118 The FADC firmware is activated by a signal from the GLUEx trigger. The  
1119 firmware then computes the following quantities for pulses observed above a  
1120 given threshold within a given time window: pulse number, arrival time, pulse  
1121 height, pulse integral, pedestal level preceding the pulse, and a quality factor  
1122 indicating the accuracy of the computed arrival time. Signal filtering and inter-  
1123 polation are used to obtain the arrival time to the nearest 0.8 ns. The firmware  
1124 performs these calculations both for the CDC and FDC alike, and uses different  
1125 readout modes to provide the data with the precision required by the separate  
1126 detectors. For example, the CDC electronics read out only one pulse but require  
1127 both pulse height and integral, while the FDC electronics read out up to four  
1128 pulses and does not require a pulse integral.

1129 The FDC anode wires are read out using the JLab pipeline F1 TDC[44] with  
1130 a nominal least count of 120 ps.

#### 1131 *5.4. Gas system*

1132 Both the CDC and FDC operate with the same gases, argon and CO<sub>2</sub>. Since  
1133 the relative mixture of the two gases is slightly different for the two tracking  
1134 chambers, the gas system has two separate but identical mixing stations. There  
1135 is one gas supply of argon and CO<sub>2</sub> for both mixing stations. A limiting opening  
1136 in the supply lines provides over-pressure protection to the gas system, and  
1137 filters in the gas lines provide protection against potential pollution of the gas  
1138 from the supply. Both gases are mixed using mass flow controllers (MFCs) that  
1139 can be configured to provide the desired mixing ratio of argon and CO<sub>2</sub>. The  
1140 MFCs and their control electronics are from BROOKS Instruments<sup>51</sup> are used  
1141 throughout.

1142 The mixed gas is filled into storage tanks, with one tank for the CDC and  
1143 another for the FDC. The pressures are regulated by controlling the operation of  
1144 the MFCs with a logic circuit based on an Allen-Bradley ControlLogix system<sup>52</sup>  
1145 that keeps the pressure in the tank between 10 and 12 psi. The tank serves both  
1146 as a reservoir and a buffer. A safety relief valve on each tank provides additional  
1147 protection against over-pressure. While the input pressure to the MFC is at  
1148 40 psi, the pressure after the MFC is designed to always be less than 14 psi  
1149 above atmospheric pressure. After the mixing tank, a provision is built into the  
1150 system to allow the gas to pass through an alcohol bath to add a small amount  
1151 of alcohol gas to the gas mixture. This small admixture of alcohol protects the  
1152 wire chambers from aging effects caused by radiation exposure from the beam.  
1153 This part of the gas system is located above ground in a separate gas shed,

---

<sup>51</sup>BROOKS Instruments, <https://www.brooksinstrument.com/en/products/mass-flow-controllers>.

<sup>52</sup>Allen-Bradley, <https://ab.rockwellautomation.com/>

1154 before the gas mixture is transported to the experimental hall via polyethylene  
1155 pipes.

1156 Additional MFCs in the hall allow the exact amount of gas provided to the  
1157 chambers to be specified: one MFC for the CDC and another four MFCs for the  
1158 individual FDC packages. The CDC is operated with a flow of 1.0 l/m, while  
1159 each FDC package is operated with a flow of 0.1 l/m. To protect the chambers  
1160 from over-pressure, there is a bypass line at the input to the detectors that is  
1161 open to the atmosphere following a bubbler containing mineral oil. The height  
1162 of the oil level determines the maximum possible gas pressure at the input to the  
1163 chambers. There is a second bubbler at the output to protect against possible  
1164 air back-flow into the chamber. The height of the oil above the exhaust line  
1165 determines the operating pressure inside the chambers.

1166 Valves are mounted at many locations in the gas system to monitor various  
1167 pressures with a single pressure sensor. The pressures of all six FDC chambers  
1168 are monitored, as well as the CDC gas at the input, downstream gas plenum  
1169 and the exhaust. A valve in the exhaust line can be used to divert some gas  
1170 from the chamber to an oxygen sensor. Trace quantities of oxygen will reduce  
1171 the gas gain and reduce tracking efficiency. The oxygen levels in the chamber  
1172 are below 100 ppm.

### 1173 *5.5. Calibration, performance and monitoring*

1174 Time calibrations for the drift chambers are used to remove the time offset  
1175 due to the electronics, so that after calibration the earliest possible arrival time  
1176 of the pulse signals is at 0 ns. These offsets and the function parameters used to  
1177 describe the relationship between the pulse arrival time and the closest distance  
1178 between the track and the anode wire are obtained for each session of data  
1179 taking.

1180 The CDC measures the energy loss,  $dE/dx$ , of tracks over a wide range of  
1181 polar angles, including recoiling target protons as well as more forward-going  
1182 tracks. Gain calibrations are made to ensure that  $dE/dx$  is consistent between  
1183 tracking paths through different straws and stable over time. The procedure  
1184 entails matching the position of the minimum ionizing peak for each of the 3522  
1185 straws, and then matching the  $dE/dx$  at 1.5 GeV/c to the calculated value of  
1186 2.0 keV/cm. This takes place during the early stages of data analysis. Gain  
1187 calibration for the individual wires is performed each time the HV is switched  
1188 on and whenever any electronics modules are replaced. Gain calibration for the  
1189 chamber as a whole is performed for each session of data taking; these sessions  
1190 are limited to two hours as the gain is very sensitive to the atmospheric pressure.  
1191 Position calibrations were necessary to describe the small deflection of the straw  
1192 tubes midway along their length; these were performed in 2016 and repeated  
1193 in 2017, with no significant difference found between the two sets of results.  
1194 Position resolution from the CDC is of the order of 130  $\mu\text{m}$  and its detection  
1195 efficiency per straw is over 98% for tracks up to 4 mm from the CDC wire. The  
1196 efficiency decreases as the distance between the track and the wire increases,  
1197 but the close-packing arrangement of the straw tubes and the large number of  
1198 straws traversed by each track compensate for this.



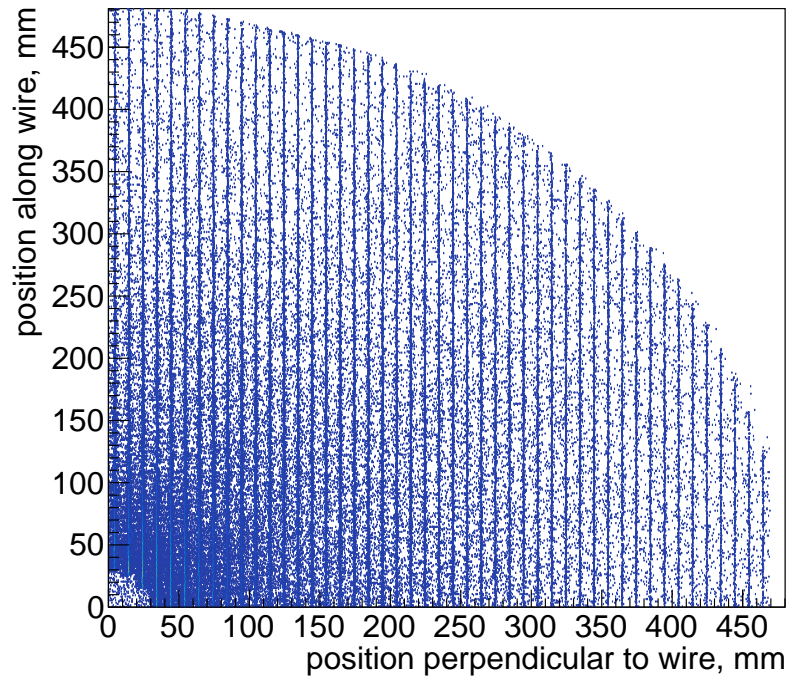


Figure 17: Wire (avalanche) positions reconstructed from the strip information on the two cathodes in one FDC chamber. Only one quarter of the chamber is shown in this figure.

1199 For the FDC system, an internal per-chamber calibration process is first  
 1200 performed to optimize the track position accuracy. In the FDC the avalanche  
 1201 created around the wire is seen in three projections: on the two cathodes and on  
 1202 the wires. The drift time information from the wires is used to reconstruct the  
 1203 hit position perpendicular to the wire. The strip charges from the two cathodes  
 1204 are used to reconstruct the avalanche position along the wire. The same strip  
 1205 information can be used to reconstruct the avalanche position perpendicular to  
 1206 the wire, which, due to the proximity of the avalanche to the wire, is practically  
 1207 the wire position, as illustrated in Fig 17. This strip information is used to  
 1208 align the strips on the two cathodes with respect to the wires. At the same  
 1209 time, the residuals of the reconstructed wire positions are an estimate of the  
 1210 strip resolution. The resolutions of the detector were reported earlier [45]. The  
 1211 strip resolution along the wires, estimated from the wire position reconstruction,  
 1212 varies between 180 and 80  $\mu\text{m}$ , depending on the total charge induced on the  
 1213 strips. The drift distance is reconstructed from the drift time with a resolution  
 1214 between 240 and 140  $\mu\text{m}$  depending on the distance of the hit to the wire in the  
 1215 0.5 – 4.5 mm range.

1216 Position offsets and package rotations were determined for both drift cham-  
1217 ber systems, first independently, and then together, using the alignment software  
1218 MILLEPEDE[46] in a process described in [38] and in [47].

1219 Online monitoring software enables shift-takers to check that the number of  
1220 channels recording data, the distribution of signal arrival times, and the  $dE/dx$   
1221 distribution are as expected.

## 1222 6. Performance of the charged-particle-tracking system

### 1223 6.1. Track reconstruction

1224 The first stage in track reconstruction is pattern recognition. Hits in adjacent  
1225 layers in the FDC in each package are formed into track segments that are linked  
1226 together with other segments in other packages to form FDC track candidates  
1227 using a helical model for the track parameters. Hits in adjacent rings in the axial  
1228 layers of the CDC are also associated into segments that are linked together with  
1229 other segments in other axial layers and fitted with circles in the projection  
1230 perpendicular to the beam line. Intersections between these circles and the  
1231 stereo wires are found and a linear fit is performed to find a  $z$ -position near the  
1232 beamline and the tangent to the dip angle  $\lambda = \pi/2 - \theta$ . These parameters, in  
1233 addition to the circle fit parameters, form a CDC track candidate for each set  
1234 of linked axial and stereo layers. Candidates that emerge from the target, and  
1235 pass through both FDC and CDC in the  $5^\circ - 20^\circ$  range, are linked together.

1236 The second stage uses a Kalman filter [48, 49] to find the fitted track param-  
1237 eters  $\{z, D, \phi, \tan \lambda, q/p_T\}$  at the position of closest approach of the track to the  
1238 beam line. The track candidate parameters are used as an initial guess, where  
1239  $D$  is the signed distance of closest approach to the beam line. The Kalman filter  
1240 proceeds in steps from the hits farthest from the beam line toward the beam  
1241 line. Energy loss and multiple scattering are taken into account at each step  
1242 along the way, according to a map of the magnetic field within the bore of the  
1243 solenoid magnet.

1244 For the first initial pass of the filter, the drift time information from the wires  
1245 is not used. Each particle is assumed to be a pion, except for low momentum  
1246 track candidates ( $p < 0.8 \text{ GeV}/c$ ), for which the fits are performed with a proton  
1247 hypothesis.

1248 The third stage matches each fitted track from the second stage to either the  
1249 Start Counter, the Time-of-Flight scintillators, the Barrel Calorimeter, or the  
1250 Forward Calorimeter to determine a start time  $t_0$  so that the drift time to each  
1251 wire associated with the track could be used in the fit. Each track is refitted  
1252 with the drift information, separately for each value of mass for particles in the  
1253 set  $\{e^\pm, \pi^\pm, K^\pm, p^\pm\}$ .

### 1254 6.2. Momentum and vertex resolution

1255 The momentum resolution as a function of angle and magnitude for pions  
1256 and protons is shown in Fig. 18. The angular resolution is shown in Fig. 19.

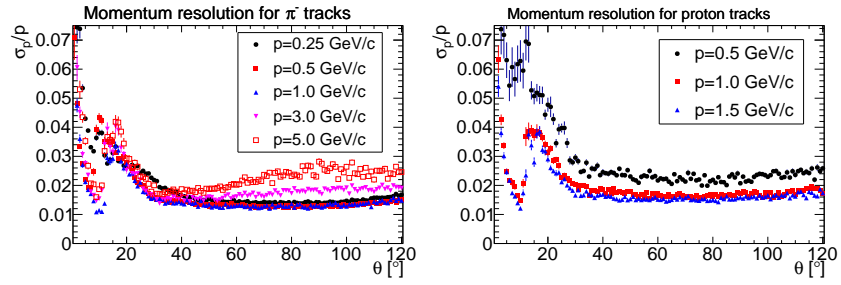


Figure 18: (Left) Momentum resolution for  $\pi^-$  tracks. (Right) Momentum resolution for proton tracks.

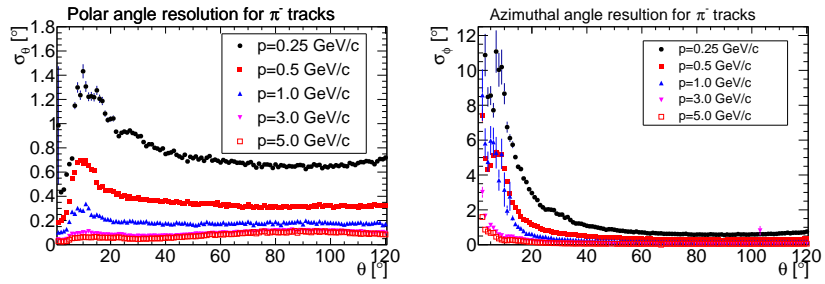


Figure 19: (Left) Polar angle resolution for  $\pi^-$  tracks. (Right) Azimuthal angle resolution for  $\pi^-$  tracks. The resolutions are plotted as a function of the polar angle,  $\theta$ .

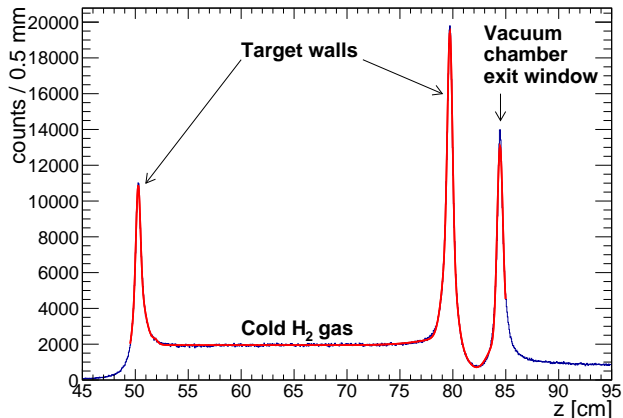


Figure 20: Reconstructed vertex positions within 1 cm radial distance with respect to the beam line for an empty target measurement. The curve shows the result of a fit to the vertex distribution used to determine the vertex resolution.

1257 The thin windows of the cryogenic target and the exit window of the  
 1258 target vacuum chamber provide a means to estimate the vertex resolution of the  
 1259 tracking system. Pairs of tracks from empty target measurements are used to  
 1260 reconstruct these windows as illustrated in Fig. 20. The distance of closest  
 1261 approach between two tracks,  $d$ , was required to be less than 1 cm. The vertex  
 1262 position is at the mid-point of the line segment (of length  $d$ ) defined by the  
 1263 points of closest approach for each track. The estimated  $z$ -position resolution  
 1264 is 3 mm.

## 1265 7. Electromagnetic calorimeters

### 1266 7.1. Barrel Calorimeter

1267 The Barrel Calorimeter (BCAL) is an electromagnetic sampling calorimeter  
 1268 in the shape of an open cylinder. Photon showers with energies between  
 1269 0.05 GeV and several GeV,  $11^\circ$ – $126^\circ$  in polar angle, and  $0^\circ$ – $360^\circ$  in azimuthal  
 1270 angle are detected. The geometry is fairly unique with the production target  
 1271 located in the backward part of the cylinder, as shown in Fig. 1. The contain-  
 1272 ment of showers depends on the angle of photon incidence, with a thickness of  
 1273 15.3 radiation lengths for particles entering normal to the calorimeter face and  
 1274 reaching up to 67 radiation lengths at  $14^\circ$ . Details of the design, construction  
 1275 and performance of the BCAL can be found in Ref.[50].

1276 The BCAL is constructed as a lead and scintillating-fiber matrix, consisting  
 1277 of 0.5 mm-thick corrugated lead sheets and 1.0 mm-diameter Kuraray SCSF-  
 1278 78MJ multi-clad scintillating fibers. The fibers run parallel to the cylindrical  
 1279 axis of the detector. Each module has approximately 185 layers and 15,000

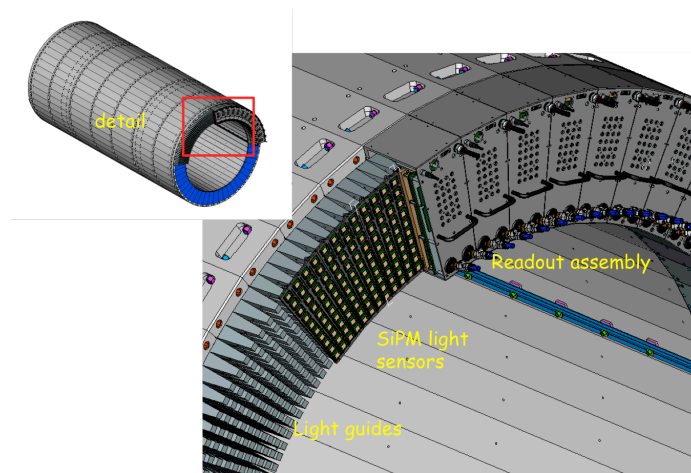


Figure 21: Three-dimensional rendition of the light guides mounted at the end of the BCAL, as well as the readout assemblies mounted over them. The readout assemblies contain the SiPMs and their electronics. (Color online)

1280 fibers. The BCAL consists of 48 optically isolated modules, each with a trapezoidal  
 1281 cross section, forming a 3.9-m-long cylindrical shell having inner and  
 1282 outer radii of 65 cm and 90 cm, respectively. The light generated in the fibers  
 1283 is collected via small light guides at each end of the module, which transport  
 1284 the light to silicon photomultipliers (SiPMs), which were chosen due to their  
 1285 insensitivity to magnetic fields. The end of the calorimeter with light guides,  
 1286 light sensors and electronics is shown in Fig. 21.

1287 The SiPM light sensors are Hamamatsu S12045(X) Multi-Pixel-Photon Counter  
 1288 (MPPC) arrays<sup>53</sup>, which are  $4 \times 4$  arrays of  $3 \times 3$  mm<sup>2</sup> tiles [51]. The SiPMs  
 1289 were accepted following extensive testing. [52, 53, 54, 55, 56, 57]. Four thousand  
 1290 units were purchased and 3840 are installed in the detector. The gain of the  
 1291 SiPM depends on the voltage above the breakdown voltage, about 70 V. These  
 1292 are operated at 1.4 V over the breakdown voltage, selected to reduce the effect  
 1293 of readout thresholds. Even at this relatively high over-bias, the noise level is  
 1294 dominated by fluctuations in the electronics baseline and not by single-pixel  
 1295 noise. In order to keep a constant gain, the temperature is maintained within

<sup>53</sup>Hamamatsu Corporation, Bridgewater, NJ 08807, USA  
 (<http://sales.hamamatsu.com/en/home.php>).

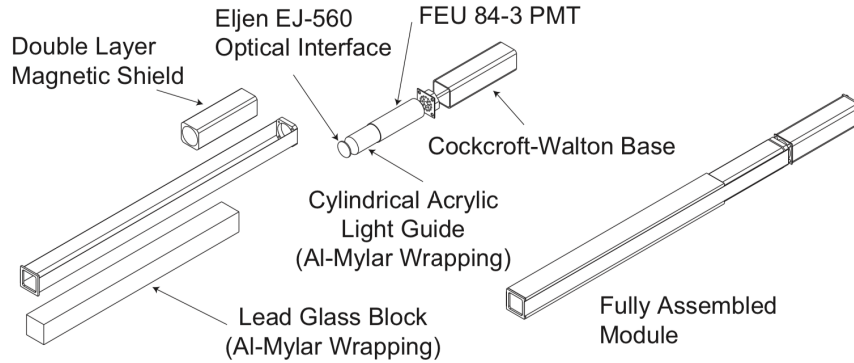


Figure 22: Expanded view of a single FCAL module.

1296 practical limits ( $\pm 2^\circ\text{C}$ ) using a chilled-water system. The gain is stabilized  
 1297 using a custom circuit that adjusts the bias voltage based on the measured tem-  
 1298 perature. Two stages of preamplifiers and summing electronics are attached to  
 1299 the sensors. In order to reduce the number of signals that are digitized, circuits  
 1300 sum the outputs of the preamplifiers in groups of radial columns, with coarser  
 1301 granularity away from the target. The layer closest to the target employs a  
 1302 single SiPM, and the next three layers have two, three, and four SiPMs, respec-  
 1303 tively. On the end of each module, forty SiPMs generate sixteen signals that are  
 1304 delivered to FADCs and twelve signals that are discriminated and then recorded  
 1305 with pipeline TDCs. The FADCs and TDCs are housed in VXS crates located  
 1306 on the floor close to the detector (see Section 9).

### 1307 7.2. Forward Calorimeter

1308 The Forward Calorimeter (FCAL) detects photon showers with energies  
 1309 ranging from 0.1 GeV to several GeV, and between  $1^\circ$ – $11^\circ$  in polar angle. The  
 1310 front face of the FCAL is located 5.6 m downstream from the center of the  
 1311 GlueX target and consists of 2800 lead glass blocks stacked in a circular array  
 1312 that has a diameter of 2.4 m. Each lead glass block has a transverse dimensions  
 1313 of  $4 \times 4 \text{ cm}^2$  and length of 45 cm. The material of the lead-glass blocks is equiv-  
 1314 alent to type F8 manufactured by the Lytkarino Optical Glass Factory.<sup>54</sup> The  
 1315 blocks and most of the PMTs were taken from the decommissioned experiments  
 1316 E852 at Brookhaven National Laboratory [58] and the RadPhi Experiment at  
 1317 JLab [59]. To remove accumulated radiation damage, the glass was annealed  
 1318 by heat treatment prior to installation in GLUEX. The detector is enclosed in a  
 1319 dark room.

1320 The light collection is accomplished via an Eljen EJ-560 optical interface  
 1321 “cookie” and a UVT acrylic cylindrical light guide glued to the PMT. The light

<sup>54</sup><http://lzos.ru> .

1322 guide recesses the magnetically sensitive photocathode of the PMT inside a dual  
1323 layer of soft iron and mu-metal that attenuates the stray field of the GLUEX  
1324 solenoid ( $\lesssim 200$  G). The sensors are FEU 84-3 PMTs with Cockcroft-Walton  
1325 bases, each consuming 0.2 W. The design of the PMT base is similar to that  
1326 noted in Ref. [60], and eliminates the need for a 2800-channel high-voltage power  
1327 system. The bases communicate with a controller using the CAN protocol [61],  
1328 with 100 bases on each of 28 CAN buses. The communication allows continuous  
1329 monitoring of the PMT voltages, temperatures, and current draw. A schematic  
1330 of a single FCAL module is shown in Fig. 22 and more details may be found in  
1331 Ref. [62]. FCAL signals are routed to FADC electronics, situated on a platform,  
1332 directly behind the FCAL dark room.

### 1333 *7.3. Electronics*

1334 Custom readout electronics for the two calorimeters are mounted in standard  
1335 VXS crates and include JLab 12-bit 250 MHz FADCs [63], discriminators [64]  
1336 and F1 TDCs [44]. The maximum input scale of the FADCs (4095 counts) is set  
1337 to 2 V. The FADCs sample each calorimeter channel every 4 ns and generate  
1338 raw waveforms consisting of 100 samples (400 ns). The samples are available  
1339 for further processing by the firmware upon a trigger signal, if the waveform  
1340 exceeds a threshold voltage. The firmware computes several derived quantities  
1341 of the pulse: pedestal, peak value, integral over a selected window, and time  
1342 of the halfway point on the leading edge. At most one pulse is extracted from  
1343 each readout window. These pulse features constitute the raw data that is  
1344 nominally read out from the FADC. Optionally, the full waveforms can be read  
1345 out for diagnostic purposes and to check the firmware output against the offline  
1346 emulation of the parameter extraction; this is done for less than about 1% of  
1347 the production runs.

1348 Pulses are identified by the first sample that exceeds a threshold, currently  
1349 set to 5 (8) counts above the average pedestal for the BCAL (FCAL). These  
1350 thresholds correspond to approximately 2.5 (12) MeV. The integral is deter-  
1351 mined using a fixed number of samples relative to the threshold crossing, which  
1352 was determined by maximizing the ratio of signal to pedestal noise. The inte-  
1353 gration window begins one sample before the threshold time and extends to 26  
1354 (15) samples after the threshold time for the BCAL (FCAL). Typical pedestal  
1355 widths are  $\sigma \sim 1.2$ -1.3 (0.8) counts. For the BCAL, the pedestals are determined  
1356 for each channel event-by-event, appropriately scaled, and then subtracted from  
1357 the peak and integral to obtain signals proportional to the energy deposited in  
1358 the calorimeter. For the FCAL the average pedestal over a run period is deter-  
1359 mined offline for each channel and the pedestal contribution to the pulse integral  
1360 is subtracted when the data are reconstructed. The algorithm that determines  
1361 the time of the pulse is pulse-height independent and, therefore, time-walk cor-  
1362 rection is not required for the FADC times [65].

1363 The outputs of the three inner layers of the BCAL are also fanned out to  
1364 leading-edge discriminators, which feed the JLab F1 TDCs. The discriminator  
1365 thresholds are initially set to 35 mV and then adjusted channel by channel. The  
1366 pulse times are recorded relative to the trigger in a 12-bit word. Multiple hits

1367 may be recorded per channel per event (up to eight), but are culled at a later  
1368 time by comparison to FADC times. The nominal least count is configured to  
1369 be 58 ps.

#### 1370 *7.4. Calibration and monitoring*

1371 The relative gains of the calorimeters are monitored using a modular LED-  
1372 driver system [66]. The control system is the same for both calorimeters, but  
1373 the arrangement of LEDs is tailored to the respective detector geometries. In  
1374 the BCAL, one LED is inserted into each light guide, which can be used to  
1375 monitor each individual SiPM and its partner at the far end of the module.  
1376 Due to geometry, the illumination varies considerably from channel to channel.  
1377 The average gain stability of the detector over a period of ten days is better  
1378 than 1% and the fractional root-mean-square deviations of the mean for each  
1379 SiPM during a single day from the average over the run period is typically less  
1380 than 2%.

1381 For the FCAL, four acrylic panes were installed, each covering the upstream  
1382 end of one quadrant of the FCAL. Each pane is illuminated by forty LEDs, ten  
1383 violet, ten blue, and twenty green. In addition to monitoring the stability of  
1384 the readout, the different colors are used to study the wavelength dependence of  
1385 the transmission of light through the lead glass blocks. In particular, radiation  
1386 damage to lead glass inhibits transmission at the blue end of the spectrum  
1387 and tends to turn glass a brownish color [67]. Throughout a several-month  
1388 experiment, the response to the green LEDs was unchanged. However, the PMT  
1389 response to violet LEDs degraded by about 10% in the blocks closest to the beam  
1390 line, characteristic of radiation damage. Such damage is only evident in the first  
1391 two layers of blocks surrounding the 12 cm $\times$ 12 cm beam hole. This damage is  
1392 likely confined to the upstream end of the block and does not significantly affect  
1393 the response to particle showers in the body of the glass.

1394 The energy of a photon or lepton is obtained from the reconstructed elec-  
1395 tromagnetic shower. Here, a shower is reconstructed using an algorithm that  
1396 finds a cluster by grouping signals close in time and space, called hits, that have  
1397 been registered by individual detector elements. Details of the algorithms to  
1398 obtain shower energies in the BCAL can be found in Ref. [50] and in Ref. [68]  
1399 for the FCAL. The clustering in the FCAL requires that hits register within 15  
1400 ns of the primary hit, where the seed threshold is taken to be 35 MeV. Clusters  
1401 with a single hit are discarded. In the event of overlapping showers, the hit  
1402 energies are divided among the clusters in proportion to the partition predicted  
1403 by a typical shower profile. Both detectors have sources of energy-dependent  
1404 nonlinearities and empirical corrections are developed and applied to minimize  
1405 the measured energy dependence of the measured  $\pi^0$  mass.

#### 1406 *7.5. Performance*

1407 The performance of the calorimeter is summarized by its ability to measure  
1408 the energy, position and timing of electromagnetic showers.

1409 The energy resolution of each calorimeter was extracted from the measured  
1410  $\pi^0$  and  $\eta$  mass distributions, yielding consistent results. To study the  $\eta$  mass



1411 resolution, events were selected using kinematic fits to  $\gamma p \rightarrow p\pi^+\pi^-\gamma\gamma$ , with  
 1412  $\eta \rightarrow \gamma\gamma$  and the photons having the same energies within 10%. The proton  
 1413 and pion tracks were used to determine the event vertex, needed to accurately  
 1414 reconstruct the two-photon invariant mass. This reaction provides a fairly clean  
 1415 sample of  $\eta$ 's with energy-symmetric photons recorded either both in the BCAL  
 1416 or both in the FCAL. The single-photon energy resolution was determined from  
 1417 Gaussian fits to the  $\eta$  invariant mass width, neglecting contributions from uncer-  
 1418 tainty in the opening angle. Monte Carlo simulation of  $\gamma p \rightarrow p\pi^+\pi^-\eta$  events,  
 1419 with kinematics chosen to approximate the experimental distributions, were  
 1420 used to tune the MC resolution to match the data. The single-photon resolu-  
 1421 tions are shown in Fig. 23(a) for the BCAL and Fig. 23(b) for the FCAL as a  
 1422 function of the mean photon energy, both for data and simulation. A fit has  
 1423 been performed to the data for each calorimeter to estimate contributions to  
 1424 noise from stochastic and constant processes. The parameters in the fit are  
 1425 correlated due to the limited range in energy available for this data.

1426 The resolution of the position ( $Z$ ) along the length of the BCAL ( $\sim 2.5$  cm)  
 1427 is computed from the timing resolution of the system, which was measured to  
 1428 be  $\sigma = 150$  ps at 1 GeV. The transverse position resolution ( $\sigma$ ) obtained from  
 1429 simulation for 1 GeV showers in the FCAL is less than 1.1 cm.

1430 The performance of the calorimeters has been demonstrated in the recon-  
 1431 struction of neutral states including  $\pi^0$ ,  $\eta$  and  $\eta'$  mesons for the first GLUEX  
 1432 physics publications [69, 70]. In addition, although the response of the calorime-  
 1433 ters at high energy is still under evaluation, it has provided important electron-  
 1434 pion separation to identify the decays of  $J/\psi \rightarrow e^+e^-$  [71] where electrons were  
 1435 recorded up to 8 GeV.

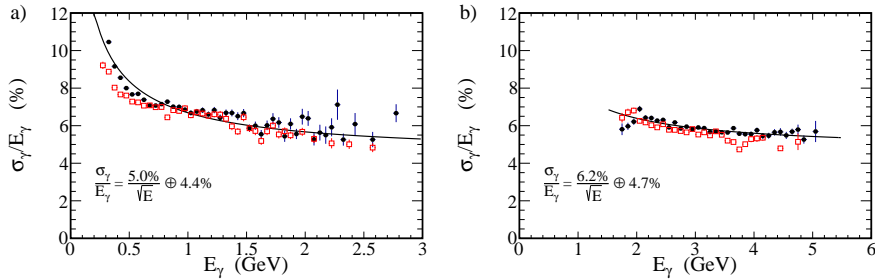


Figure 23: The energy resolution,  $\sigma_\gamma/E_\gamma$ , for single photons in the a) BCAL and b) FCAL calculated from the  $\eta$  mass distribution under the assumption that only the energy resolution contributes to its width. Solid black circles are data and open red squares are simulation. Fitted curves including the stochastic and constant terms are indicated. (Color online)

## 1436 8. Scintillation detectors

1437 There are two scintillator-based detectors deployed in the GLUEX spectrom-  
 1438 eter: a small barrel-shaped detector surrounding the target, referred to as the  
 1439 Start Counter (ST), and a two-plane hodoscope detector system in the forward

1440 direction, referred to as the Time-of-Flight (TOF) detector. Both detectors provide  
1441 timing information. Charged-particle identification is derived from energy  
1442 loss ( $dE/dx$ ) in the ST and flight time from the TOF.

### 1443 8.1. Start Counter

1444 The ST, shown in Fig. 24, surrounds the target region and covers about 90%  
1445 of the solid angle for particles originating from the center of the target. The ST  
1446 is designed to operate at tagged photon beam intensities of up to  $10^8$  photons per  
1447 second in the coherent peak, and has a high degree of segmentation to limit the  
1448 per-paddle rates. The time resolution must be sufficient to resolve the RF beam  
1449 structure and identify the electron beam bunch from which the event originated  
1450 (see Section 2.1). The ST provides a timing signal that is relatively independent  
1451 of particle type and trajectory (because of its proximity to the target) and can  
1452 be used in the Level 1 trigger if necessary. The specific energy deposits  $dE/dx$   
1453 in ST are used for charged-particle identification in combination with the flight-  
1454 time from the TOF. Details of the design, construction and performance of the  
1455 ST system can be found in Ref. [72].

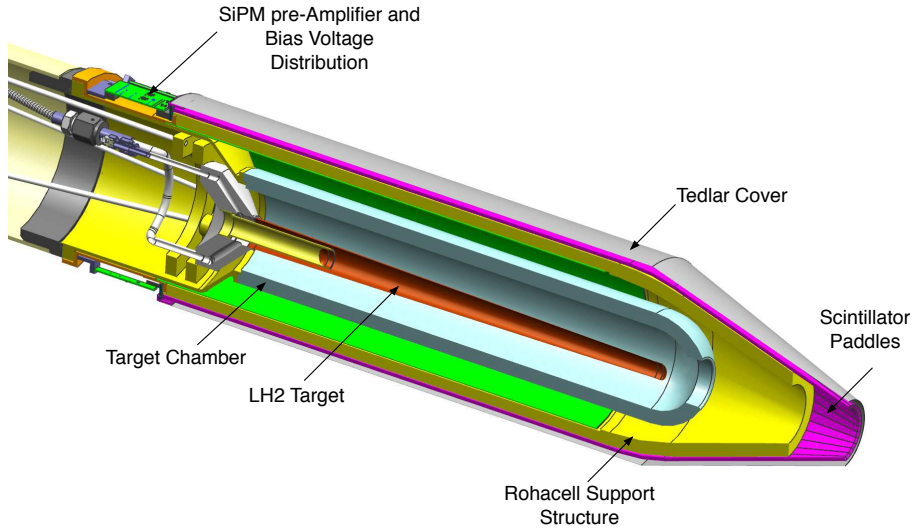


Figure 24: The GLUEX Start Counter surrounding the liquid-hydrogen target assembly. The incident beam travels from left to right down the central axis.

1456 The ST consists of 30 scintillator paddles arranged in a cylinder of radius  
1457 78 mm with a “nose” section that bends towards the beam line to a radius of

1458 20 mm at the downstream end. EJ-200 scintillator from Eljen Technology<sup>55</sup>  
1459 was selected for the ST paddles. EJ-200 has a decay time of 2.1 ns with a bulk  
1460 attenuation length of 380 cm. Each scintillator paddle originated from stock  
1461 3 mm thick and 600 mm in length. The paddles were bent at Eljen to create  
1462 the nose section, and then machined at McNeal Enterprises Inc.<sup>56</sup> to their  
1463 final shape, including edges beveled at 6° to minimize loss of acceptance. The  
1464 scintillator paddles are supported by a Rohacell closed-cell foam structure. The  
1465 Rohacell is 11 mm thick and is rigidly attached to an aluminum support hub  
1466 at the upstream end. The downstream support extends partially into the nose  
1467 section. The cylindrical length of the Rohacell is further reinforced with three  
1468 layers of carbon fiber, each layer being 650  $\mu\text{m}$  thick. The assembly is made  
1469 light-tight with a Tedlar wrapping, attached to a plastic collar at the upstream  
1470 end.

1471 Silicon photomultiplier detectors are used as light sensors, as these are not  
1472 affected by the magnetic field produced by the solenoid. The SiPMs were placed  
1473 at the upstream end of each scintillator element with a 250  $\mu\text{m}$  air gap. Each  
1474 paddle is read out with an array of four SiPMs (Hamamatsu S109031-050P  
1475 multi-pixel photon counters) whose signals are summed. The on-board elec-  
1476 tronics provides two signals per paddle, one delivered to an FADC, and the  
1477 other to a  $5\times$  amplifier that is sent to a discriminator and then to a TDC.

## 1478 8.2. Time-of-flight counters

1479 The TOF system delivers fast timing signals from charged particles passing  
1480 through the detector thereby providing information for particle identification.  
1481 The TOF detector is a wall of scintillators located about 5.5 m downstream from  
1482 the target, covering a polar angular region from 0.6° to 13°. The detector has  
1483 two planes of scintillator paddles stacked in the horizontal and vertical direction.  
1484 Most paddles are 252 cm long and 2.54 cm thick with a width of 6 cm. The  
1485 scintillator material is EJ-200 from Eljen Technology. To allow the photon  
1486 beam to pass through the central region, an aperture of  $12\times 12\text{ cm}^2$  is kept free  
1487 of any detector material by using four shorter, single-PMT paddle detectors  
1488 with a length of 120 cm around the beam hole in each detector plane. These  
1489 paddles also have a width of 6 cm and a thickness of 2.54 cm. In order to keep  
1490 the count rate of the paddles well below 2 MHz the two inner-most full-length  
1491 paddles closest to the beam hole on either side have a reduced width of 3 cm.  
1492 Light guides built out of UV transmitting plastic provide the coupling between  
1493 the scintillator and the PMT and allow the magnetic shielding to protect the  
1494 photocathode by extending about 5 cm past the PMT entrance window. All  
1495 paddles are wrapped with a layer of a highly reflective material (DF2000MA  
1496 from 3M) followed by a layer of strong black Tedlar film for light tightness.

1497 The scintillator paddles are read out using PMTs from Hamamatsu.<sup>57</sup> Full-

---

<sup>55</sup>Eljen Technology, <https://eljentechnology.com/products/plastic-scintillators>.

<sup>56</sup>McNeal Enterprises Inc., <http://www.mcnealplasticmachining.com>

<sup>57</sup>Hamamatsu Photonics, <https://www.hamamatsu.com/us/en/index.html>.

1498 length paddles have a PMT at both ends, while the short paddles have a single  
1499 PMT at the outer end of the detector. These type H10534 tubes have ten stages  
1500 and are complete assemblies with high voltage base, casing and  $\mu$ -metal shield-  
1501 ing. Additional soft-iron external shielding protects each PMT from significant  
1502 stray fields from the solenoid magnet.

### 1503 *8.3. Electronics*

1504 High voltage for the TOF PMTs is provided by CAEN HV modules of type  
1505 A1535SN, initially controlled by a CAEN SY1527 main frame and later up-  
1506 graded to a SY4527. The PMT outputs are connected to a passive splitter by  
1507 a 55'-long RG-58 coaxial cables. The signal is split into two equal-amplitude  
1508 signals. One signal is directly connected to a FADC [73], while the second signal  
1509 passes first through a leading-edge discriminator and is then used as an input  
1510 to a high resolution TDC. The digitizing modules are mounted in VXS crates  
1511 as described in Section 9. The threshold of the leading-edge discriminator is  
1512 controlled separately for each channel and has an intrinsic deadtime of about  
1513 25 ns.

1514 The sparcification threshold for the FADC is set to 120 (160) counts for  
1515 the ST (TOF), with the nominal pedestal set at 100 counts. The high voltage  
1516 of each TOF PMT is adjusted to generate the amplitude of the signal from a  
1517 minimum-ionizing particle of at least 400 ADC counts above baseline. The data  
1518 from the FADC is provided by the FPGA algorithm and consists of two words  
1519 per channel with information about pedestal, signal amplitude, signal integral,  
1520 and timing.

1521 The timing signals from the ST system are registered using the JLab F1  
1522 TDCs, which have a nominal least count of 58 ps. In order to take advantage  
1523 of the higher intrinsic resolution of the TOF counters, this system uses the  
1524 VX1290A TDCs from CAEN<sup>58</sup>, which are multi-hit high-resolution TDCs with  
1525 a buffer of up to 8 words per channel and a nominal least count of 25 ps. Since  
1526 these TDCs provide the best time measurements in the GLUEX detector, the  
1527 timing of the accelerator RF signal is also digitized using these TDCs.

### 1528 *8.4. Calibration and monitoring*

1529 The combined ST and TOF systems are used to determine the flight times  
1530 of particles, the ST providing a precise start time in combination with the  
1531 accelerator RF, and the TOF providing the stop time. Both systems may also  
1532 be used to provide information on particle energy loss. Therefore, the signals  
1533 in ST and TOF must be calibrated to determine corrections for the effects of  
1534 time-walk, light propagation time offsets, and light attenuation. The procedures  
1535 are slightly different for the two detectors because of the different geometries,  
1536 intrinsic resolutions, and the advantages of the TOF system having two adjacent  
1537 perpendicular planes.

---

<sup>58</sup>CAEN, <https://www.caen.it/>

1538 For the time-walk correction for each paddle of the ST, the detector signal is  
1539 sent to both an FADC and a TDC. The time from the FADC, being independent  
1540 of pulse amplitude, is the reference. The amplitude dependence of the difference  
1541 between TDC and FDC times is used to measure the time walk; the resulting  
1542 curve is fit to an empirical function for use in the correction. The propagation  
1543 time is measured as a function of the hit position in a paddle as determined  
1544 by well-reconstructed charged particle tracks. The propagation velocity is measured  
1545 in three regions of the counter (“straight,” “bend,” and “nose”) and is not  
1546 assumed to be a single value for all hits. The light attenuation is also measured  
1547 at several positions along the counter using charged particle tracks. The energy-  
1548 per-unit pathlength in the paddle as a function of distance from the SiPM is  
1549 fit to a modified exponential, with different parameters allowed for the straight  
1550 section and the nose section, with continuity enforced at the section boundary.

1551 The calibration procedures for the TOF system take advantage of the two  
1552 planes of narrow paddles oriented orthogonal to each other, which permits cal-  
1553 ibration of the full TOF detector independent of any other external detector  
1554 information. The overlap region of two full-length paddles from the two planes  
1555 define a  $6 \times 6$  cm<sup>2</sup> area for most paddles, with a few  $3 \times 3$  cm<sup>2</sup> areas close to  
1556 the beam hole. The separation between the two detector planes is minimal as  
1557 they are mounted adjacent to each other, separated only by wrapping material.  
1558 While the time-difference (TD) between the two ends of a paddle is related to  
1559 the hit position along the paddle, the mean-time (MT) is related to the flight  
1560 time of a particle from the vertex to the paddle. Therefore, the MT for two  
1561 overlapping paddles must be the same when hit by the same particle passing  
1562 through both paddles, while the hit position in the horizontal and vertical di-  
1563 mensions are defined by the TD of the two paddles. This relationship results  
1564 in an internally consistent calibration of all paddles with respect to every other  
1565 paddle. Prior to finding timing offsets for calibration, all times must corrected  
1566 for the amplitude-dependent walk. The relation between time at threshold and  
1567 signal amplitude is parameterized and used to correct for time slewing.

1568 After all full-length paddles have been calibrated, they can be used them-  
1569 selves as references to calibrate the remaining eight short paddles that only  
1570 have single-ended readout. Again we use the fact that any overlap region of two  
1571 paddles from different planes has the same particle flight time from the vertex.  
1572 This coincidence produces peaks in the time difference distributions that can be  
1573 used to determine the timing offsets of these single-ended readout paddles.

1574 To test the calibration, we take tracks that are incident on a paddle in one  
1575 plane and compute the time difference between the MT of that paddle and  
1576 the MT of every other full-length paddle in the other plane. The resulting  
1577 distribution of these differences is shown in Fig. 25. Assuming that all paddles  
1578 have the same timing resolution, we can compute the average time resolution  
1579 to be  $\sigma = 105$  ps =  $\frac{148}{\sqrt{2}}$  ps, assuming a Gaussian distribution.

### 1580 8.5. Performance

1581 The purpose of the ST is to select the electron beam bunch that generated  
1582 the tagged photon which induced a reaction in the target. The corresponding

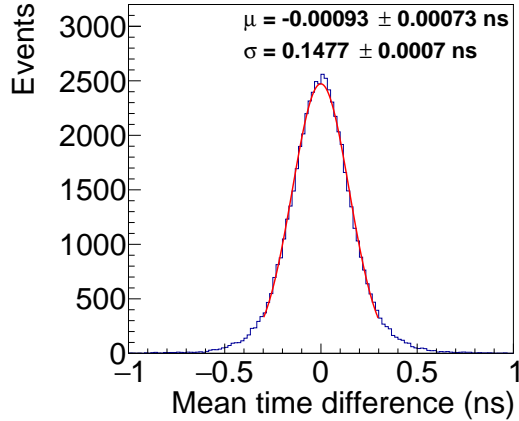


Figure 25: Mean time difference between one TOF long paddle of one plane with all other long paddles of the other plane. (Color online)

1583 time derived from a signal from the CEBAF accelerator, which is synchronized  
 1584 with the RF time structure of the machine, is used to determine the event start  
 1585 time. Therefore, the ST resolution does not contribute to the resolution of the  
 1586 flight time as long as the resolution is sufficient to pick out the correct beam  
 1587 bunch with high probability.

1588 The ST timing performance can be determined by comparing the event time  
 1589 at the target measured by the start counter and the accelerator RF time. The  
 1590 start counter time must be corrected for the flight path of the charged particle  
 1591 emerging from the event, and all instrumental corrections mentioned in the  
 1592 previous section must be applied. Fig. 26 shows the distribution of this time  
 1593 difference. The average time resolution is about  $\sigma=234$  ps, where the resolution  
 1594 varies depending on the position of the hit along the counter.

1595 The ST is also used to identify particles using  $dE/dx$ . Fig. 27 shows  $dE/dx$   
 1596 versus momentum,  $p$ , for charged particles tracked to the Start Counter. Protons  
 1597 can be separated from pions up to  $p = 0.9$  GeV/ $c$ .

1598 The performance of the TOF detector for particle identification (PID) was  
 1599 investigated by considering the relative number of particle types within the event  
 1600 sample. Events with at least three fully-reconstructed positively-charged tracks  
 1601 were selected, with at least one of these tracks intersecting the TOF detector.  
 1602 More pions are expected than protons, and more protons than kaons. Looking  
 1603 at the distribution of velocity,  $\beta$ , of these tracks as a function of momentum,  
 1604 the bands from protons, kaons and pions are identified (see Fig. 28).

1605 The distributions of  $\beta$  at two specific track momenta, 2 GeV/ $c$  and 4 GeV/ $c$   
 1606 (see Fig. 29), are illustrative of the PID capability of the TOF detector. At  
 1607  $p = 2$  GeV/ $c$ , the TOF detector provides about a  $4\sigma$  separation between the  
 1608 pion/positron peak and the kaon peak, sufficient to identify tracks as kaons

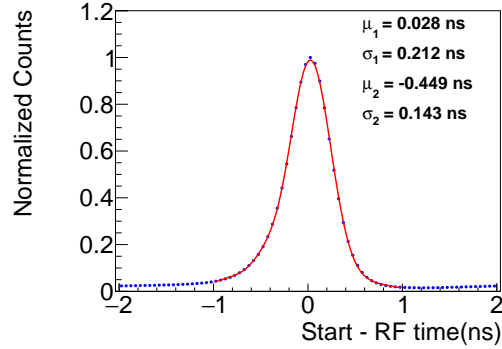


Figure 26: Time difference distribution between the vertex time computed from the start counter and the accelerator RF. The time from the RF does not contribute significantly to the width of the distribution. The fit function is a double Gaussian plus a third-degree polynomial.

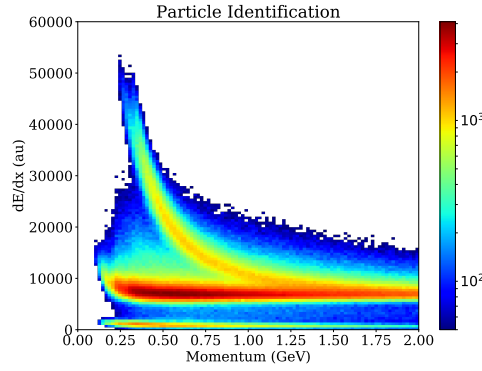


Figure 27:  $dE/dx$  vs.  $p$  for the Start Counter. The curved band corresponds to protons while the horizontal band corresponds to electrons, pions, and kaons. Pion/proton separation is achievable for tracks with  $p < 0.9$  GeV/ $c$ .

1609 with  $\beta = 0.97$ , or lower, with very high certainty. However, at  $\beta = 0.98$ , the  
 1610 probability of the track being a kaon is less than 50%, due to the abundance  
 1611 of pions that is an order of magnitude larger than kaons. The protons, on the  
 1612 other hand, are very well separated from the other particle types and can be  
 1613 identified with high confidence over the full range in  $\beta$ . At a track momentum  
 1614 of 4 GeV/ $c$ , PID becomes much more difficult and represents the limit at which  
 1615 the a time-of-flight measurement can identify protons with high confidence. The  
 1616 separation between the large peak containing pions, kaons and positrons from  
 1617 the proton peak is about  $4\sigma$ , while the relative abundance in this case is about  
 1618 a factor of 4. As a consequence, a 4 GeV/ $c$  momentum track with  $\beta = 0.975$   
 1619 is most likely a proton, with a small probability of being a pion. At  $\beta = 0.98$ ,

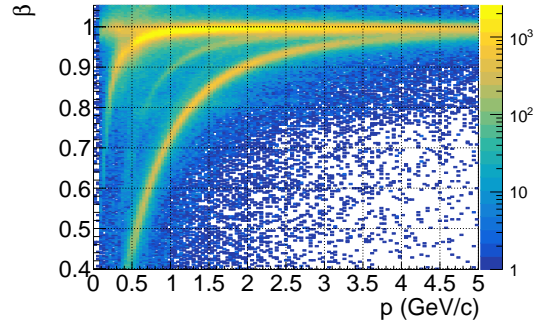


Figure 28:  $\beta$  of positive charged tracks versus track momentum, showing bands for  $e^+$ ,  $\pi^+$ ,  $K^+$  and  $p$ . The color coding of the third dimension is in logarithmic scale. (Color online)

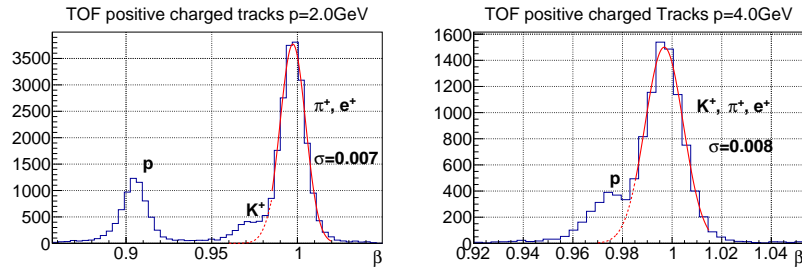


Figure 29:  $\beta$  of positive charged tracks with 2 GeV/c momentum (left) and with 4 GeV/c (right).

1620 such a track has a similar probability for being a proton or a pion.

## 1621 9. Trigger

1622 The goal of the GLUEX trigger is to accept most high-energy hadronic in-  
 1623 teractions while reducing the background rate induced by electromagnetic and  
 1624 low-energy hadronic interactions to the level acceptable by the data acquisition  
 1625 system (DAQ). The main trigger algorithm is based on measurements of energy  
 1626 depositions in the FCAL and BCAL as described in Ref. [74, 75]. Supplemen-  
 1627 tary triggers can also use hits from scintillator detectors, such as the PS, tagging  
 1628 detectors, ST, TOF, and TAC.

### 1629 9.1. Architecture

1630 The GLUEX trigger system[76] is implemented on dedicated programmable  
 1631 pipelined electronics modules, designed at JLab using Field-Programmable Gate  
 1632 Arrays (FPGAs). The GLUEX trigger and readout electronics are hosted in VXS



1633 (ANSI/VITA 41.0) crates. VXS is an extension of the VME/VME64x architec-  
1634 ture, which uses high-speed backplane lines to transmit trigger information.

1635 A layout of the trigger system is presented in Fig. 30. Data from the FCAL  
1636 and BCAL are sent to FADC modules [73], situated in 12 and 8 VXS crates,  
1637 respectively, and are digitized at the sampling rate of 250 MHz. The digitized  
1638 amplitudes are used for the trigger and are also stored in the FPGA-based  
1639 pipeline for subsequent readout via VME. Digitized amplitudes are summed for  
1640 all 16 FADC250 channels in each 4 ns sampling interval and are transmitted to  
1641 the crate trigger processor (CTP) module, which sums up amplitudes from all  
1642 FADC boards in the crate. The sub-system processor (SSP) modules located  
1643 in the global trigger crate receive amplitudes from all crates and compute the  
1644 total energy deposited in the FCAL and BCAL. The global trigger processor  
1645 (GTP) module collects data from the SSPs and makes a trigger decision based  
1646 on the encoded trigger equations. The core of the trigger system is the trigger  
1647 supervisor (TS) module, which receives the trigger information from the GTP  
1648 and distributes triggers to the electronics modules in all readout crates in order  
1649 to initiate the data readout. The GLUEX system has 55 VXS crates in total (26  
1650 with FADC250s, 14 with FADC125s, 14 with F1 TDCs, and 1 CAEN TDC). The  
1651 TS also provides a synchronization of all crates and provides a 250 MHz clock  
1652 signal. The triggers and clock are distributed through the trigger distribution  
1653 (TD) module in the trigger distribution crate. The signals are received by  
1654 the trigger interface (TI) module and signal distribution (SD) module in each  
1655 crate. The GLUEX trigger system provides a fixed latency. The longest trigger  
1656 distribution time of about  $3.3 \mu\text{s}$  is due to the distance of the tagger hall from  
1657 Hall D. The smallest rewritable readout buffer, where hits from the detector are  
1658 stored, corresponds to about  $3.7 \mu\text{s}$  for the F1 TDC module. The trigger jitter  
1659 does not exceed 4 ns.

## 1660 9.2. Trigger types

1661 The GLUEX experiment uses two main trigger types: the pair spectrometer  
1662 trigger, and the physics trigger based on energy depositions in the BCAL and  
1663 FCAL. The pair spectrometer trigger is used to measure the flux of beam pho-  
1664 tons. This trigger requires a time coincidence of hits in the two arms of the PS  
1665 detector, described in Section 2.9. The physics triggers are generated when the  
1666 FCAL and BCAL energies satisfy the following conditions:

1667 1.  $2 \cdot E_{\text{FCAL}} + E_{\text{BCAL}} > 1 \text{ GeV}$ ,  $E_{\text{FCAL}} > 0 \text{ GeV}$ , and

1668

1669 2.  $E_{\text{BCAL}} > 1.2 \text{ GeV}$ .

1670 The first condition defines the main trigger that uses the fact that most events  
1671 produce forward-going energy. The second trigger type is used to accept events  
1672 with large transverse energy released in the BCAL, such as decays of  $J/\psi$   
1673 mesons.

1674 Several other trigger types were implemented for efficiency studies and de-  
1675 tector calibration. Efficiency of the main production trigger was studied using  
1676 a trigger based on the coincidence of hits from the ST and TAGH, detectors not

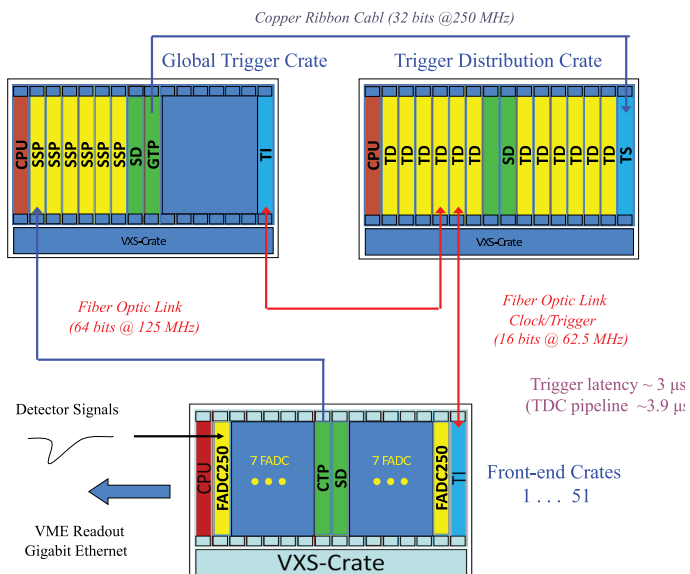


Figure 30: Schematic view of the Level-1 trigger system of the GLUEX experiment. The electronics boards are described in the text.

1677 used in the main production trigger. A combination of the PS and TAC triggers  
 1678 was used for the acceptance calibration of the PS, described in Section 2.9.1.  
 1679 Ancillary minimum-bias random trigger and calorimeter LED triggers were collected  
 1680 concurrently with data taking.

### 1681 9.3. Performance

1682 The rate of the main physics triggers as a function of the PS trigger rate is  
 1683 shown in Fig. 31. The typical rate of the PS trigger in spring 2018 was about  
 1684 3 kHz, which corresponds to a photon beam flux of  $2.5 \cdot 10^7 \gamma/\text{sec}$  in the coherent  
 1685 peak range. The total trigger rate was about 40 kHz. The rates of the random  
 1686 trigger and each of the LED calorimeter triggers were set to 100 Hz and 10 Hz,  
 1687 respectively. The electronics and DAQ were running with a livetime close to  
 1688 100%, collecting data at a rate of 600 MB per second. The trigger system can  
 1689 operate at significantly higher rates, considered for the next phase of the GlueX  
 1690 experiment. The combined dead time of the trigger and DAQ systems at the  
 1691 trigger rate of 80 kHz was measured to be about 10%. The largest contribution  
 1692 to the dead time comes from the hit processing time of readout electronics  
 1693 modules.

## 1694 10. Data acquisition

1695 The GLUEX data acquisition software uses the CEBAF Data Acquisition  
 1696 (CODA) framework. CODA is a software toolkit of applications and libraries

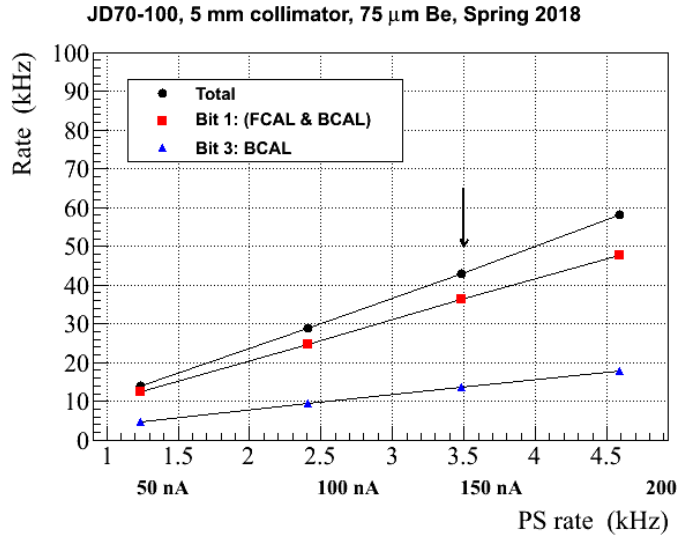


Figure 31: Rate of the main production triggers as a function of the PS rate: FCAL and BCAL trigger (boxes), BCAL trigger (triangles), the total trigger rate (circles). The vertical arrow indicates the run condition corresponding to the experimental run of spring 2018.

1697 that allows customized data acquisition systems based on distributed commercial  
 1698 networks. A detailed description of CODA software and hardware can be  
 1699 found in Ref. [77].

1700 The maximum readout capability of the electronics in the VME/VXS crate is  
 1701 200 MB/s per crate and the number of crates producing data is about 55. The  
 1702 data from the electronic modules are read via the VME back-plane (2eSST,  
 1703 parallel bus) by the crate readout controller (ROC), which is a single board  
 1704 computer running Linux. The GLUEX network layout and data flow are shown  
 1705 in Fig. 32. Typical data rates from a single ROC are in the range of 20–70 MB/s,  
 1706 depending on the detector type and trigger rate. The ROC transfers data over  
 1707 1 Gbit Ethernet links to Data Concentrators (DC) using buffers containing event  
 1708 fragments from 40 triggers at a time. Data Concentrators are programs that  
 1709 build partial events received from 10-12 crates and run on a dedicated computer  
 1710 node. The DC output traffic of 200-600 MB/s is routed to the Event Builder  
 1711 (EB) to build complete events. The Event Recorder (ER), which is typically  
 1712 running on the same node as an Event Builder, writes data to local data storage.  
 1713 GLUEX has been collecting data at a rate of 500–900 MB/s, which allows the  
 1714 ER to write out to a single output stream. The system is expandable to handle  
 1715 higher luminosity where rates rise to 1.5–2.5 GB/s. In this case, the ER must  
 1716 write multi-stream data to several files in parallel. All DAQ computer nodes  
 1717 are connected to both a 40 Gb Ethernet switch and a 56 Gb Infiniband  
 1718 The Ethernet network is used exclusively for DAQ purposes: receiving data  
 1719 from detectors, building events, and writing data to disk, while the Infiniband

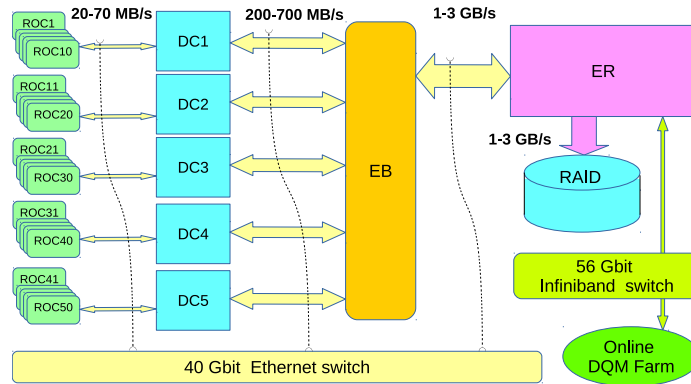


Figure 32: Schematic DAQ configuration for GLUEX. The high-speed DAQ connections between the ROCs and the ER are contained within an isolated network. The logical data paths are indicated by arrows, although physically they are routed through the 40 Gbit ethernet switch. The online monitoring system uses its own separate 56 Infiniband switch.

1720 network is used to transfer events for online data quality monitoring. This allows  
 1721 decoupling DAQ and monitoring network traffic. The livetime of the DAQ is  
 1722 in the range of 92–100%. The deadtime arises from readout electronics and  
 1723 depends on the trigger rate. The DAQ software does not cause dead time during  
 1724 an experimental run, but software-related dead time appears while stopping and  
 1725 starting the run, which takes between 2-8 minutes.

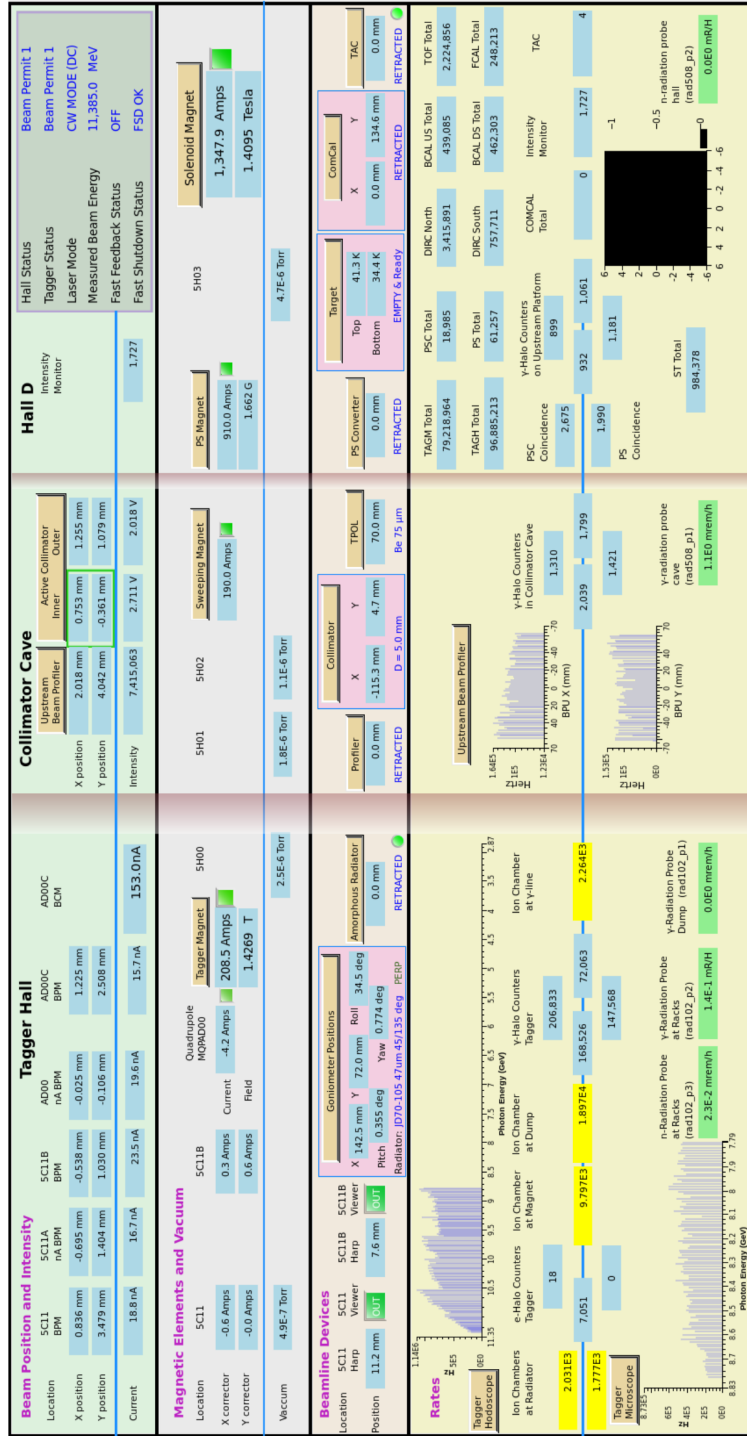


Figure 33: Top-level graphical interface for the beamline. This screen provides information on beam currents and rates, radiators, magnet status, target condition, background levels, etc.

## 1726 11. Slow controls

1727 GLUEX must monitor and control tens of thousands of different variables  
1728 that define the state of the experimental hardware. The values need to be  
1729 acquired, displayed, archived, and used as inputs to control loops continually  
1730 with a high degree of reliability. For GLUEX, approximately 90,000 variables  
1731 are archived, and many more are monitored.

### 1732 11.1. Architecture

1733 The GLUEX slow control system consists of three layers. The first layer  
1734 consists of the remote units such as high voltage or low voltage power chas-  
1735 sis, magnet power supplies, temperature controller, LabView applications, and  
1736 PLC-based applications, which directly interact with the hardware and contain  
1737 almost the all the control loops. The second layer is the Supervisory Control  
1738 and Data Acquisition (SCADA) layer, which is implemented via approximately  
1739 140 EPICS Input/Output Controllers (IOC's). This layer provides the inter-  
1740 face between low level applications and higher level applications via the EPICS  
1741 ChannelAccess protocol. The highest level, referred as the Experiment Control  
1742 System (ECS), contains applications such as Human-Machine Interfaces, the  
1743 alarm system, and data archiving system. This structure allows for relatively  
1744 simple and seamless addition and integration of new components into the overall  
1745 controls system.

### 1746 11.2. Remote Units

1747 GLUEX uses a variety of commercial units to provide control over the hard-  
1748 ware used in the experiment. For instance, most detector high voltages are  
1749 provided by the CAEN SYx527 voltage mainframe,<sup>59</sup> while the low and bias  
1750 voltages are provided by boards residing in a Wiener MPOD chassis<sup>60</sup>. These  
1751 two power supply types provide most voltages for detector elements with the  
1752 exception of Tagger Microscope and Forward Calorimeter. Here custom systems  
1753 were developed that provide voltage regulation and interact with the EPICS-  
1754 based layer through higher level interfaces using custom protocols. See Sec-  
1755 tions. 2.4.2 and 7.2 for more details.

1756 Various beam line devices need to be moved during beam operations. Step-  
1757 per motors are used to move motorized stages via Newport XPS universal  
1758 multi-axis motion controllers<sup>61</sup> that allow for execution of complex trajec-  
1759 tories involving multiple axes. All stage referencing, motion profile computations,  
1760 and encoder-based closed-loop control occur within the controller chassis after  
1761 the basic parameters, such as positions and velocities, are provided by the user  
1762 via a TCP/IP-based interface to EPICS.

---

<sup>59</sup><https://www.caen.it/subfamilies/mainframes/>

<sup>60</sup><http://www.wiener-d.com/sc/power-supplies/mpod-lvhv/mpod-crate.html>

<sup>61</sup><https://www.newport.com/c/xps-universal-multi-axis-motion-controller>.

1763 Custom controls systems were developed for each particular system while  
1764 installing complex systems, such as a superconducting magnet that requires  
1765 large numbers of input and output channels and sophisticated logic. For these  
1766 cases, we used Allen-Bradley CompactLogix and ControlLogix PLC systems<sup>62</sup>.  
1767 These systems are designed for industrial operations, allow modular design,  
1768 provide high reliability, and require minimal maintenance. All controls loops  
1769 are programmed within the PLC application, and are interfaced with EPICS  
1770 through a TCP/IP-EtherNet/IP-proprietary protocol to allow access by higher  
1771 level applications to process variables delivered by the PLC's.

1772 The cryogenic target and the superconducting solenoid employ National In-  
1773 struments LabView applications. The target controls use both custom-made  
1774 and vendor-supplied hardware that include built-in remotely-accessible control  
1775 systems and an NI CompactRIO<sup>63</sup> chassis. This chassis communicates with the  
1776 hardware and serves variables using an internal ChannelAccess server and an  
1777 EPICS IOC running on the CompactRIO controller, as described in Sec. 4. A  
1778 National Instruments PXI high-performance system<sup>64</sup> is used to collect data  
1779 from different sensors as described in Sec. 3.

### 1780 *11.3. Supervisory Control and Data Acquisition layer*

1781 The SCADA layer is the middle layer that distributes the process variables  
1782 allowing the higher level –and sometimes lower level– applications to use various  
1783 process variables of the Hall-D control system. This layer is based on EPICS  
1784 and uses the ChannelAccess protocol to publish the values of the variables over  
1785 Ethernet. Efficient exchange of the information between the experiment and ac-  
1786 celerator operations is achieved because the accelerator controls also use EPICS.  
1787 Several dozen software IOC processes, running on hosts computers of the ex-  
1788 periment control process, collect data from different components of the lowest  
1789 layer. Each IOC is configured to communicate using the protocol appropriate  
1790 for the remote units with which data exchange is needed. For instance, the IOC  
1791 controlling the voltage for the FDC detector needs to be able to communicate  
1792 with the Wiener MPOD and CAEN SYx527 voltage chassis. The middle layer is  
1793 primarily used to distribute data between different applications. This layer also  
1794 contains some EPICS-based applications running on IOC's that provide differ-  
1795 ent control loops and software interlocks. For instance, the low-voltage power  
1796 supplies for the FDC detector (see Sec. 5.2) are shut off if the temperature or  
1797 the flow of the coolant in the chiller falls outside of required limits.

### 1798 *11.4. Experiment Control System*

1799 The highest level of controls contains applications that archive data, display  
1800 data in interactive GUIs and as stripcharts, alarm and notify shift personnel and

---

<sup>62</sup><https://ab.rockwellautomation.com>.

<sup>63</sup><https://www.ni.com/en-us/shop/compactrio.html>

<sup>64</sup><https://www.ni.com/en-us/shop/pxi.html>

1801 experts in case problems occur, and interface with the CODA-based data ac-  
1802 quisition system (Sec. 10). An example of such a GUI is the beamline overview  
1803 screen, shown in Fig. 33. Many of the buttons of the GUI are active and allow  
1804 access to other GUIs. Display management and the alarm system for GLUEx  
1805 controls are based on Controls System Studio (CSS),<sup>65</sup> which is an Eclipse-  
1806 based toolkit for operating large systems. CSS is well suited for systems that  
1807 use EPICS as an integral component. Although CSS provides an archiving  
1808 engine and stripcharting tools, the MYA archiver,[78] provided by the JLab ac-  
1809 celerator software group, was employed with its tools for displaying the archived  
1810 data as a time-series. Display management for GLUEx controls is within the  
1811 CSS BOY [79] environment, which allows system experts to build sophisticated  
1812 control screens using standard widgets. The alarm system is based on the CSS  
1813 BEAST[80] alarm handler software, which alerts shift personnel of problems  
1814 with the detector, and notifies a system expert if the problems are not resolved  
1815 by shift personnel.

## 1816 12. Online computing system

1817 This section describes the GLUEx software and computing systems used for  
1818 data monitoring and for transport to the tape system for permanent storage.

### 1819 12.1. Monitoring

1820 The Online Monitoring system consists of multiple stages that provide im-  
1821 mediate monitoring of the data, as well as near-term monitoring (a few hours  
1822 after acquisition). Immediate monitoring is based on the *RootSpy* system[81]  
1823 written for use in GLUEx, though its design is not experiment specific. Figure  
1824 34 shows a diagram of the processes involved in the RootSpy system and how  
1825 those processes are coupled to the DAQ system. The Event Transfer System  
1826 (ET) process is part of the CODA DAQ system [82] and is used to extract a  
1827 copy of a portion of the datastream without interfering with data acquisition.  
1828 The monitoring system uses a secondary ET to minimize connections to the  
1829 RAID server running the Event Recorder process.

1830 The monitoring system is run on a small computer farm<sup>66</sup> in the counting  
1831 house, each processing a small part of the data stream. In total, about 10% of  
1832 the data is processed for the low level occupancy plots while roughly 2% is fully  
1833 reconstructed for higher level analysis. The CODA ET software system is used  
1834 to distribute the data among the farm computers. Each farm node generates  
1835 histograms, which *RootSpy* gathers and combines before display to shift workers  
1836 in a GUI. Plots are displayed via a set of ROOT [83] macros, each responsible

---

<sup>65</sup><http://controlsystemstudio.org/>

<sup>66</sup>The online monitoring farm consists of eight 2012 era Intel x86\_64 computers with 16 cores+16 hyper-threads (ht) plus six 2016 era Intel x86\_64 computers with 36 cores + 36ht. The monitoring farm uses 40 Gbps (QDR) and 56 Gbps(FDR) IB for the primary interconnect. Note that the DAQ system uses a separate 40 Gbps ethernet network that is independent of the farm.



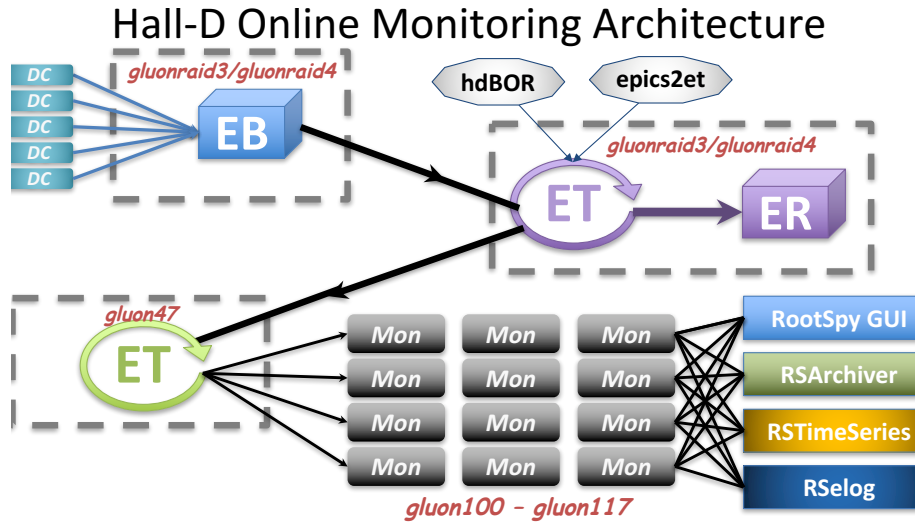


Figure 34: Processes distributed across several computers in the online monitoring system. DC, EB, and ER are the Data Concentrator, Event Builder, and Event Recorder processes, respectively, in the CODA DAQ system.

1837 for drawing a single page. Most macros divide the page into multiple sections  
 1838 so that multiple plots can be displayed on a single page. Figure 35 shows an  
 1839 example of a high-level monitoring plot, where four invariant-mass distributions  
 1840 are shown with fits. Values extracted from the fits are printed on the plots for  
 1841 easy quantitative comparison to the reference plot.

1842 There are several client programs that summarize the information available  
 1843 in the histograms produced by *RootSpy* and generate output that make it easy to  
 1844 assess the uniformity and quality of the data. One of these is the *RSTimeSeries*  
 1845 program, which periodically inserts data into an InfluxDB time series database.  
 1846 The database provides a web-accessible strip chart of detector hit rates and  
 1847 reconstructed quantities (e.g. number of  $\rho$ 's per 1k triggers). Another is the  
 1848 *RSArchiver* program that gathers summed histograms to be displayed in the  
 1849 Plot Browser<sup>67</sup> website. Plot Browser provides easy comparison of plots between  
 1850 different runs and between different analysis passes. Jobs are automatically  
 1851 submitted to the JLab farm for full reconstruction of the first five files (100GB)  
 1852 of each run. The results are displayed in Plot Browser and may be compared  
 1853 directly with the online analysis of the same run.

#### 1854 12.2. Data transport and storage

1855 GLUEX Phase I generated production data at rates up to 650MB/s. The  
 1856 data were temporarily stored on large RAID-6 disk arrays, and then copied to

<sup>67</sup>[https://halldweb.jlab.org/data\\_monitoring/Plot\\_Browser.html](https://halldweb.jlab.org/data_monitoring/Plot_Browser.html).

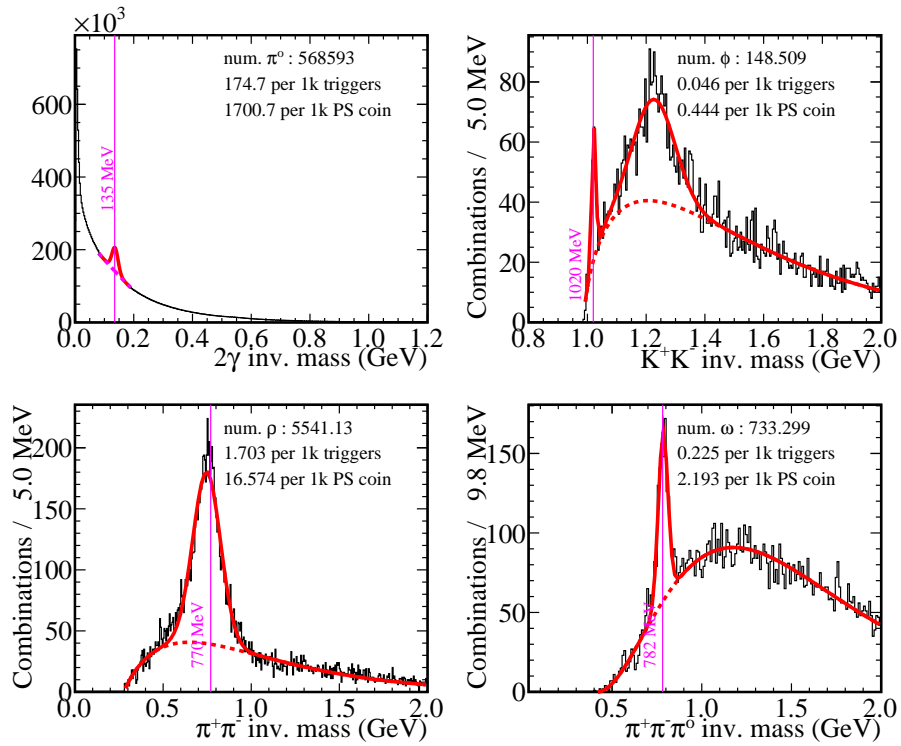


Figure 35: Invariant mass distributions showing  $\pi^0$ ,  $\omega$ ,  $\rho$ , and  $\phi$  particles. These plots were generated online in about 1hr 40min by looking at roughly 2% of the data stream.

	2016	2017	2018
actual (raw data only)	0.624	0.914	3.107
model (raw data only)		0.863	3.172
actual (production data)	0.55	1.256	1.206

Table 4: GLUEX data volumes by year. All values are in petabytes (PB). Most years include two run periods. The line marked “model” gives calculated rates from the GLUEX Computing Model[84] based on the detector luminosity. “Raw data only” represents data generated by the DAQ system (not including the backup copy). “Production” represents all derived data including reconstructed values and ROOT trees.

1857 an LT0 tape system in the JLab Computer Center for long term storage. Two  
1858 RAID servers, each with four partitions, were used for staging the data. The  
1859 partition being written was rotated between runs to minimize head thrashing  
1860 on disks by only reading partitions not currently being written. Partitions were  
1861 kept at approximately 80% capacity and older files were deleted to maintain  
1862 this level, allowing the monitoring farm easy access to files when the beam was  
1863 down. A copy of the first three files ( $\sim 1.5\%$ ) of each run was also kept on the  
1864 online computers for direct access to samples from each run.

1865 The data volumes stored to tape are shown in Table 4 in units of petabytes  
1866 (PB). Entries marked “actual” are values taken from the tape storage system.  
1867 The line marked “model” comes from the GLUEX computing model[84].

### 1868 13. Event reconstruction

1869 GLUEX uses the computer center batch farm at JLab to perform data moni-  
1870 toring, event reconstruction, and physics analyses. For data monitoring, de-  
1871 tector hit occupancies, calibration and reconstruction quality, and experimental  
1872 yields and resolutions, are analyzed for several physics channels. A subset of the  
1873 data is monitored automatically as it is saved to tape. Every few weeks, moni-  
1874 toring processes are launched on a subset of the data to study improvements from  
1875 ongoing calibrations and reconstruction software improvements. The histograms  
1876 produced by these monitoring jobs are displayed on a website and ROOT files  
1877 are available for download, enabling the collaborators to easily study the quality  
1878 of the data.

1879 Every few months, a major reconstruction launch over all of the data is  
1880 performed, linking hits in the various detector systems to reconstruct particles  
1881 in physics events. Monitoring plots from these launches are also published to  
1882 the web. Finally, regular analysis launches over the reconstructed data are per-  
1883 formed, where a reconstruction plugin filters out reactions previously specified  
1884 by users in a web form. The results of these launches are saved in reaction-  
1885 specific ROOT TTrees for further analysis.

1886 For all launches, the reconstruction is run in a multi-threaded mode to make  
1887 efficient use of the available computing resources. Fig. 36 shows the multi-  
1888 threaded scaling from our monitoring launches. The program performs near the  
1889 theoretical limit for jobs that use a number of threads that is less or equal the

1890 number of physical cores on the processor. By using hyperthreads, a smaller but  
1891 still significant gain is achieved. All file outputs are written to a write-through  
1892 cache system, which is ultimately backed up to tape.

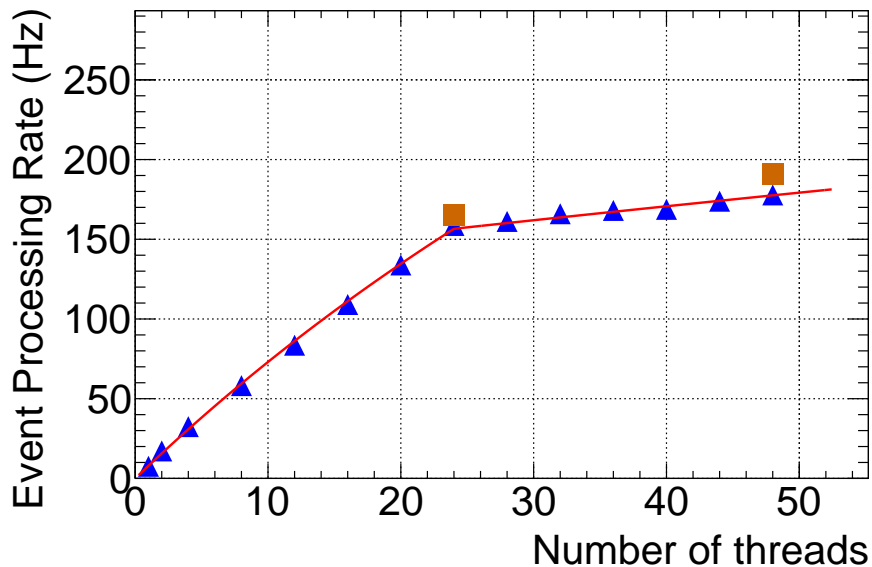


Figure 36: The scaling of program performance as a function of the number of processing threads. The computer used for this test consisted of 24 full cores (Intel x86.64) plus 24 hyperthreads. The orange squares are from running multiple processes, each with 12 threads.

1893 GLUEX Phase I has recorded about 1400 separate physics-quality runs,  
1894 with a total data footprint of about 3 petabytes. Data were saved in 19-GB  
1895 files, with all runs consisting of multiple files (typically 100 or more per run).  
1896 Fig. 37 shows an overview of the different production steps for GLUEX data,  
1897 which are described in more detail in the following subsections.

### 1898 13.1. Calibration

1899 During the acquisition of data, a unique run number is assigned to a period  
1900 of data corresponding to less than about 2 hours of clock time, which may result  
1901 in writing a couple hundred files. It is assumed that the detector changes very  
1902 little during this period and therefore there will be no changes in the calibration  
1903 constants. Two types of calibration procedures are used, depending on the  
1904 complexity of the calibration procedures. Simple, well-understood calibrations  
1905 such as timing alignment between individual channels and subdetectors or drift  
1906 chamber gain and time-to-distance calibrations, can be performed with one file  
1907 of data per run. These procedures are executed either in the online environment  
1908 or on the batch farm, and can be repeated as needed following any improvements  
1909 in reconstruction algorithms or other calibrations.

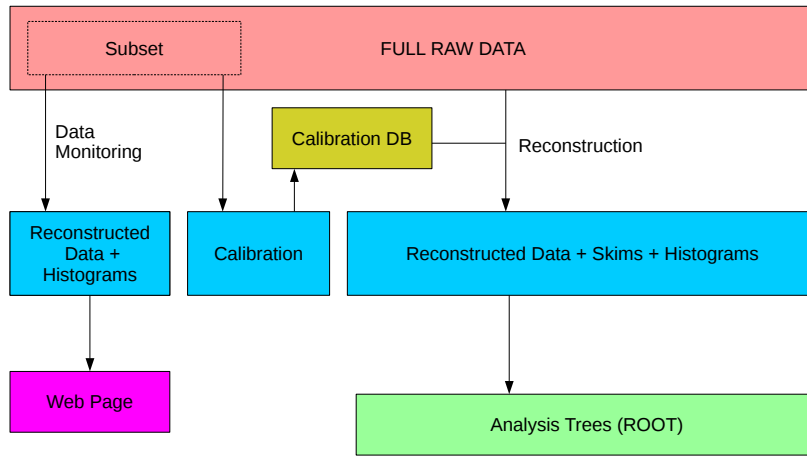


Figure 37: Production flowchart for GLUEX data, illustrating analysis steps.

1910 More complicated calibration procedures, such as calorimeter gain calibration,  
 1911 require more data and are often iterative procedures, requiring several  
 1912 passes through the data. The raw data is processed upon arrival on the batch  
 1913 farm, resulting in histograms or in selected event data files in EVIO [85] or  
 1914 ROOT-tree format. Many of these outputs require that charged particle tracks  
 1915 are reconstructed. However, the computationally intensive nature of track re-  
 1916 construction makes it a challenge to fully reconstruct all raw data as it comes  
 1917 in. Therefore, the full suite of calibration procedures is only applied to 10 - 20%  
 1918 of the data. Processing of the remaining data is mostly focused on separating  
 1919 out, or “skimming,” events collected by calibration triggers.

### 1920 13.2. Monitoring

1921 The red-colored box at the top of Fig. 37 represents experimental data that  
 1922 has been backed up to tape. The left-hand section of the box labeled “subset”  
 1923 represents the first five files of each run, which are run through offline monitoring  
 1924 processes. These monitoring jobs are first processed during the run to check the  
 1925 quality of the data, but are also processed after major changes to calibrations or  
 1926 software to validate those changes. The resulting Reconstructed Events Storage  
 1927 (REST) files and ROOT histogram files are used for checking the detector and  
 1928 reconstruction performance.

### 1929 13.3. Reconstruction

1930 When the data is sufficiently well calibrated, a full production pass on the  
 1931 physics quality data is performed. In the current total GLUEX data set, about  
 1932 1400 runs were deemed “physics quality.” The remaining runs were short runs  
 1933 related to engineering and commissioning tests of the experiment. The 1400  
 1934 physics quality runs include the majority of the data recorded during the running

1935 period, representing about 3 petabytes. All these files were reconstructed using  
1936 computing resources at several sites, equivalent to more than 20 million core-  
1937 hours combined. This produced more than 500 terabytes of REST data files.  
1938 The large reduction in size from collected event data to physics data files (about  
1939 a factor of six) permits faster and more efficient physics analyses on the data.

1940 During the REST production, a series of detector studies were performed  
1941 that required access to raw data and that would not be possible on the recon-  
1942 structed data alone. Many improvements to software and detector calibration  
1943 resulted from these studies. Similar studies can be made with simulated data  
1944 to match and assess the detector acceptance.

#### 1945 *13.4. Offsite reconstruction*

1946 Production processing of GLUOX data uses offsite high-performance com-  
1947 puting (HPC) resources in addition to the onsite computing farm at JLab,  
1948 specifically, the National Energy Research Supercomputing Center (NERSC)  
1949 and the Pittsburgh Supercomputing Center (PSC). For NERSC, the total allo-  
1950 cation used for the academic year 2018-2019 was 53M NERSC units, which was  
1951 used to process 70.5k jobs. This is equivalent to approximately 9M core-hours  
1952 on a Intel x86\_64 processor. The jobs were run on NERSC's Cori II system,  
1953 which is comprised of KNL (Knight's Landing) processors. The PSC alloca-  
1954 tion was awarded through the XSEDE<sup>68</sup> allocation system in the last quarter  
1955 of calendar year 2019 for 5.9 MSU's. Only 0.85M SU's were used in 2019 to run  
1956 7k jobs on the PSC Bridges system or about 10% of the number processed at  
1957 NERSC. Figure 38 shows how the event processing rates scaled with the number  
1958 of processing threads for both NERSC and PSC. Jobs run at both of those sites  
1959 were assigned entire nodes so the number of processing threads used was equal  
1960 to the total number of hardware threads.

1961 Container and distributed file system technologies were used for offsite pro-  
1962 cessing. The software binaries as well as calibration constants, field maps, etc.  
1963 were distributed using the CERN-VM-file system (CVMFS). The binaries were  
1964 all built at JLab using a CentOS7 system. A very lightweight Docker con-  
1965 tainer was made based on CentOS7 that had only a minimal number of system  
1966 RPMs<sup>69</sup> installed. All other software, including third-party packages such as  
1967 ROOT, were distributed via CVMFS. This meant changes to the container it-  
1968 self were very rare (about once per year). The Docker container was pulled into  
1969 NERSC's Shifter system without modification. The same container was used to  
1970 create a Singularity container used at both PSC and on the Open Science Grid  
1971 (OSG) for simulation jobs.

1972 Raw data were transferred from JLab to the remote sites using Globus<sup>70</sup>,  
1973 which uses GridFTP. The Globus tasks were submitted and managed by the

---

<sup>68</sup><https://www.xsede.org>.

<sup>69</sup>RedHat Package Management, [https://access.redhat.com/documentation/en-us/red\\_hat\\_enterprise\\_linux/5/html/deployment\\_guide/ch-rpm](https://access.redhat.com/documentation/en-us/red_hat_enterprise_linux/5/html/deployment_guide/ch-rpm)

<sup>70</sup><https://opensciencegrid.org/technology/policy/globus-toolkit>.

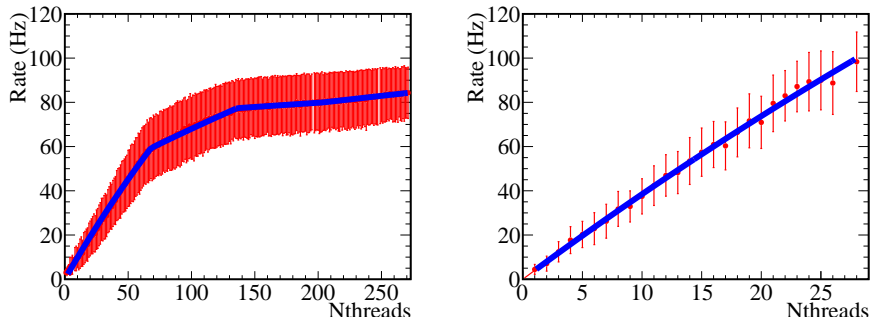


Figure 38: Event processing rate versus number of threads for reconstruction jobs on NERSC Cori II (left) and PSC Bridges (right). The slope changes in the NERSC plot is due to the KNL architecture, which had four hardware threads per core. For PSC Bridges, hyper-threading is disabled and the plot shows a single slope.

1974 SWIF2 workflow tool written by the JLab Scientific Computing group. SWIF2  
 1975 was needed to manage the data retrieval from tape, for transfer to the remote  
 1976 site, for submission of remote jobs, and for transfer of processed data back to  
 1977 JLab. Disk space limitations at both JLab and the remote sites meant only a  
 1978 portion of the data set could be on disk at any one time. Thus, SWIF2 had to  
 1979 manage the jobs through all stages of data transfer and job submission.

### 1980 13.5. Analysis

1981 The full set of reconstructed (REST) data is too large to be easily handled by  
 1982 individual analyzers. For that reason, a system was developed to analyze data  
 1983 at JLab and extract reaction-specific ROOT trees. This step is represented by  
 1984 the right-hand green box at the bottom of Fig. 37.

1985 Users can specify individual reactions via a web interface. Periodically, the  
 1986 submitted reactions are downloaded into a configuration file, which steers the  
 1987 analysis launch. For each reaction, the GLUEX analysis library inside the JANA  
 1988 framework creates possible particle combinations from the reconstructed partic-  
 1989 le tracks and showers saved in the REST format. Common selection criteria  
 1990 are applied for exclusivity and particle identification before performing a kine-  
 1991 matic fit, using vertex and four-momentum constraints. Displaced vertices and  
 1992 inclusive reactions are also supported. Objects representing successful particle  
 1993 combinations (e.g.  $\pi^0 \rightarrow \gamma\gamma$ ) and other objects are managed in memory pools,  
 1994 and can be reused by different channels to reduce the overall memory footprint  
 1995 of the process. With this scheme, up to one hundred different reactions can be  
 1996 combined into one analysis launch processing the reconstructed data.

1997 If the kinematic fit converged for one combination of tracks and showers, the  
 1998 event is stored into a reaction-specific but generic ROOT tree, made accessible  
 1999 to the whole collaboration. The size of the resulting ROOT trees for the full  
 2000 data set strongly depends on the selected reaction, but is usually small enough  
 2001 to be copied to the user's home institution for a more detailed analysis.

## 2002 14. Monte Carlo simulation

2003 The detailed simulation of events in the Hall-D beamline and GLUEX de-  
2004 tector is performed with a GEANT-based software package. The package was  
2005 originally developed within the GEANT3 framework [86] and then migrated  
2006 to the GEANT4 framework [87, 88]. The simulation framework uses the same  
2007 geometry definitions and magnetic field maps as used in reconstruction. The  
2008 geometry includes the full photon beamline, starting at the radiator and ending  
2009 at the photon beam dump. Both internal and external event generators are sup-  
2010 ported by the framework. Internal sources include the coherent bremsstrahlung  
2011 source and the single particle gun. Events read from any number of external  
2012 generators are also supported. These input events specify one or more primary  
2013 vertices to be simulated, which are randomized within the hydrogen target with  
2014 timing that matches the RF structure of the beam.

2015 The Monte Carlo data flow is presented in Fig. 39. Events of interest are  
2016 generated using either an internal or user-supplied event generator. The in-  
2017 put event specification is fed to the Hall D GEANT simulation code, either  
2018 *hdgeant* or *hdgeant4*, which tracks the particles through the experimental setup  
2019 and records the signals they produce in the active elements of the detector.  
2020 Behavior of the simulation is conditioned by a run number, which corresponds  
2021 to a particular set of experimental conditions: beam polarization and intensity,  
2022 beamline and detector geometry, magnetic field maps, etc. All this information  
2023 is read by the simulation at run-time from the calibrations database, which  
2024 functions as the single source for all time-dependent geometry, magnetic field,  
2025 and calibration data relevant to the simulation.

2026 Events written by the simulation are processed by the detector response  
2027 package *mcsmeasr*. It applies corrections to the simulated hits to account for  
2028 detector system inefficiencies and resolution, and overlays additional hits from  
2029 uncorrelated background events. Loss of hits from detector channels, multi-hit  
2030 truncation, and electronic deadtime are also applied at this step. Information  
2031 needed for this processing comes from the databases for calibrations and run-  
2032 conditions, and from files containing real backgrounds sampled using random  
2033 triggers. Events emerging from the smearing step are deemed to be faithful  
2034 representations of what the detector would have produced for the given run in  
2035 response to the specified input. These Monte Carlo events are then processed  
2036 with the same reconstruction software as used for the real events, and the output  
2037 is saved to a REST file. These REST files are then made available for physics  
2038 analysis.

### 2039 14.1. Geometry specification

2040 The geometry and material descriptions for the experiment are common  
2041 across simulation and reconstruction, residing in a family of xml files that follow  
2042 a common schema called the Hall D Detector Specification, or *HDDS* [89, 90].  
2043 Run-specific variations of the geometry xml records are maintained in the cali-  
2044 bration database. The geometry and magnetic field map are also maintained in  
2045 the calibration database.



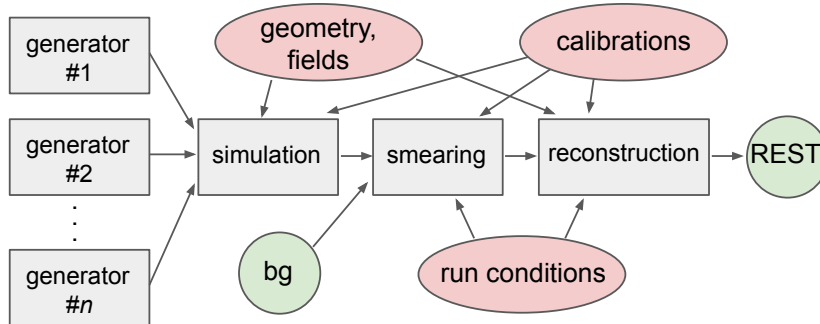


Figure 39: The Monte Carlo data flow from event generators through physics analysis REST files. The ovals represent databases containing tables indexed by run number, providing a common configuration for simulation, smearing, and reconstruction. Background events represented by the circle marked *bg* are real events collected using a random trigger, which are overlaid on the simulated events to account for pile-up in the Monte Carlo.

2046 The output events from the simulation are written as a data stream, which  
 2047 may either be piped directly into the next step of the Monte Carlo pipeline  
 2048 or saved to a file. Events are passed between all stages of the Monte Carlo  
 2049 processing pipeline, shown in Fig. 39, using the common data format of the  
 2050 Hall-D Data Model, HDDM [91]. HDDM is used for all intermediate input and  
 2051 output event streams.

#### 2052 14.2. Event generators

2053 Simulation starts with the generation of events, which can be specific parti-  
 2054 cles or reactions, or simply unbiased background events. A common toolset has  
 2055 been developed to minimize redundancy. These tools include standard methods  
 2056 to generate the distributions of primary photon beam energies and polarization.  
 2057 An output interface is used to produce files suitable as input to the GEANT  
 2058 simulation.

2059 The photon beam energy distribution can be produced using a coherent  
 2060 bremsstrahlung generator that accounts for the physical properties of the ra-  
 2061 diator and the photon beamline. This generator allows the user to select the  
 2062 orientation of the diamond radiator, and then calculates the linear polarization  
 2063 for each photon. Photons can also be generated according to the spectrum mea-  
 2064 sured in the pair spectrometer during any actual data run by interfacing to the  
 2065 calibration data base. Here the user inputs the degree of linear polarization and  
 2066 the orientation. Finally, the user can provide a histogram of the photon energy  
 2067 spectrum and a second one of the degree of polarization to be used to generate  
 2068 the photon beam.

2069 One of the first generators was used to simulate the total photoproduction  
 2070 cross section. It is currently used to study backgrounds to physics reactions  
 2071 as well as develop analysis tools for extracting signals. This event generator,  
 2072 called *bggen*, is based on Pythia [92], and includes additions that describe the

2073 low-energy photoproduction cross sections. Other generators are tied to specific  
2074 reactions, where the generator needs to describe the underlying physics.

### 2075 14.3. HDGEANT

2076 Both GEANT3 and GEANT4 versions are available for simulation of the  
2077 experiment. Both versions have been tuned to reproduce the behavior of the  
2078 experiment, but there are some differences arising from how the two versions  
2079 decide when to stop tracking particles. In general, the simulation mimics the  
2080 running conditions found across a range of runs, typically a large part of a single  
2081 run period. The output from GEANT contains both hit times and energies  
2082 deposited in detector volumes.

### 2083 14.4. Detector response

2084 Converting time and energy deposits coming from GEANT into electronic  
2085 detector responses that match the readout from the experiment is carried out  
2086 by the detector response package *mcsmeas*. The output of this digitization is  
2087 identical to the real data with the exception that the so-called *truth information*  
2088 about the data is retained to allow detailed performance studies. In addition  
2089 to the digitization, at this stage the run-dependent efficiency effects are applied  
2090 to the data, including both missing electronic channels and reduced efficiency  
2091 of other channels. Additional smearing of some signals is also applied here to  
2092 better match the performance of the Monte Carlo to data.

2093 The *mcsmeas* package also folds measured backgrounds into the data stream.  
2094 During regular data collection, random triggers are collected concurrently with  
2095 data taking (see Section 9). These are separated from the actual data and used  
2096 to provide experimental background signals in the Monte Carlo, with rates based  
2097 on the actual beam fluxes in the experiment.

### 2098 14.5. Job submission

2099 A large number of experimental conditions need to be matched in simulated  
2100 data. The *MCWrapper* tool was developed to streamline the input specifications,  
2101 implement consistency with corresponding data reconstruction, seamlessly  
2102 access computer offsite resources, and produce Monte Carlo samples in proportion  
2103 to the actual data taken. The goal is to model the differences between runs  
2104 and provide a simulated data set, comparable to the real data. The primary  
2105 system used for this phase is the Open Science Grid (OSG) in order to leverage  
2106 resources in addition to the local JLab computing farm. Many automated  
2107 checks are made to avoid flawed submission, and all aspects of the requests and  
2108 jobs are monitored during running. Once completed, *MCWrapper* checks for  
2109 expected output files to be returned as if the jobs were run on the JLab farm. If  
2110 expected files are not found the system will automatically submit a replacement  
2111 job. Once the jobs are verified completed and all data from the request has  
2112 been properly moved, the user receives an automated email alerting them that  
2113 their request has been fulfilled and the location where the user can access the  
2114 event sample.

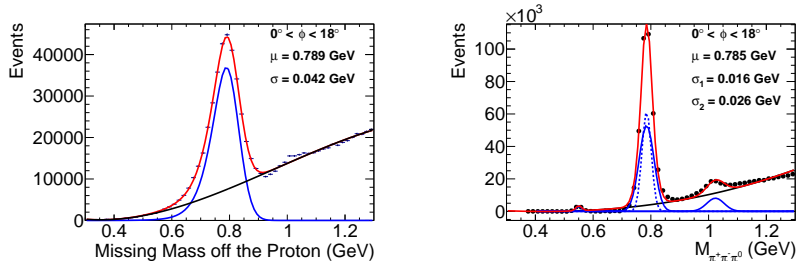


Figure 40: Reconstructed mass distributions for the reaction  $\gamma p \rightarrow p\pi^0\pi^\pm(\pi^\mp)$  for a bin in  $\phi$ . (Left) Distribution of the missing mass off the proton. (Right) Invariant mass distribution for the  $\pi^+\pi^-\pi^0$  system. The blue curves show the resonant contributions, the black curve shows the polynomial backgrounds, and the red curve shows the sum. (Color online)

2115 Users are able to monitor and control their simulations via an online dash-  
 2116 board. The *MCWrapper* dashboard gives information about active projects and  
 2117 allows users (or administrators) to interact with their requests. Users may cancel,  
 2118 suspend, or declare projects complete. Detailed information is presented  
 2119 about the individual jobs, such as where the jobs are being run, basic usage  
 2120 statistics, and current status. This information gives individuals a near real-time  
 2121 look into the production of their Monte Carlo samples.

## 2122 15. Detector performance

2123 The capability of the GLUEX detector in reconstructing charged and neutral  
 2124 particles and assembling them into fully reconstructed events has been studied  
 2125 in data and simulation using several photoproduction reactions. The results of  
 2126 these studies are summarized in this section.

### 2127 15.1. Charged-particle reconstruction efficiency

2128 The track reconstruction efficiency was estimated by analyzing  $\gamma p \rightarrow p\omega$ ,  
 2129  $\omega \rightarrow \pi^+\pi^-\pi^0$  events, where the proton, the  $\pi^0$ , and one of the charged pions  
 2130 were used to predict the three-momentum of the other charged pion. Two  
 2131 methods were used to calculate this efficiency,  $\varepsilon = N_{found}/(N_{found} + N_{missing})$ .  
 2132 Events for which no track was reconstructed in the predicted region of phase  
 2133 space contributed to  $N_{missing}$ , while events where the expected track was recon-  
 2134 structed contributed to  $N_{found}$ . For the first method, the  $\omega$  yields for  $N_{found}$   
 2135 and  $N_{missing}$  were estimated from the missing mass off the proton; for the sec-  
 2136 ond method, the invariant mass of the  $\pi^+\pi^-\pi^0$  system was used to find  $N_{found}$ .  
 2137 This analysis was performed for individual bins of track momentum,  $\theta$ , and  $\phi$ .  
 2138 Examples of mass histograms for a typical bin in  $\phi$  are shown in Fig. 40. The  
 2139 exercise was repeated for a sample of  $\omega$  Monte Carlo events. A comparison of  
 2140 the efficiency for pion reconstruction derived from the two methods for both

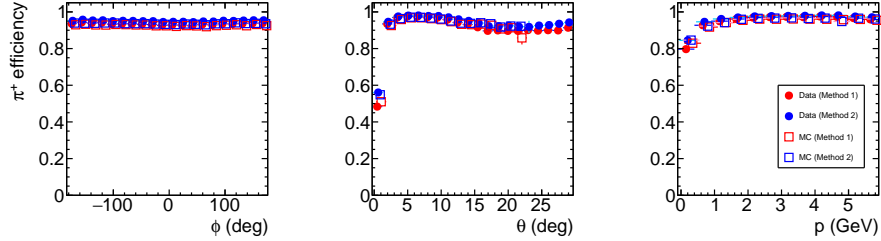


Figure 41: Tracking efficiency for  $\pi^+$  tracks, determined by data and simulation using two methods. (Color online)

2141 Monte Carlo and experimental data is shown in Fig. 41. The efficiencies for  
 2142 Monte Carlo and experimental data agree to within 5%.

2143 While this reaction only allows the determination of track reconstruction  
 2144 efficiencies for  $\theta < 30^\circ$ , this covers the majority of charged particles produced  
 2145 in GLUEX due to its fixed-target geometry. Other reactions are being studied  
 2146 to determine the efficiency at larger angles.

### 2147 15.2. Photon efficiency

2148 Photon-reconstruction efficiency has been studied using different methods for  
 2149 the FCAL and BCAL. In the FCAL, absolute photon reconstruction efficien-  
 2150 cies have been determined using the “tag-and-probe” method with a sample  
 2151 of photons from the reaction  $\gamma p \rightarrow \omega p$ ,  $\omega \rightarrow \pi^+\pi^-\pi^0$ ,  $\pi^0 \rightarrow \gamma(\gamma)$ , where one  
 2152 final photon is allowed but not required to be reconstructed. The yields with  
 2153 and without the reconstructed photon are determined using two methods. In  
 2154 the first method, the  $\omega$  yield is determined from the missing-mass spectrum,  
 2155  $M_X(\gamma p \rightarrow pX)$ , selecting on whether only one or both reconstructed photons  
 2156 are consistent with a final-state  $\pi^0$ . In the second method, the count when both  
 2157 photons are found is determined from the  $\omega$  yield from the fully reconstructed  
 2158 invariant mass  $M(\pi^+\pi^-\gamma\gamma)$ . If the photon is not reconstructed, the  $\omega$  yield  
 2159 is determined by a fit to the distribution of the missing mass off the proton.  
 2160 Both methods yield consistent results, with a reconstruction efficiency generally  
 2161 above 90%, and within 5% or less agree with the efficiencies determined from  
 2162 simulation.

2163 A relative photon efficiency determination has been performed using  $\pi^0 \rightarrow$   
 2164  $\gamma\gamma$  decays, which spans the full angular range detected in GLUEX. A sample of  
 2165 fully reconstructed  $\gamma p \rightarrow \pi^+\pi^-\pi^0 p$  events were inspected, taking advantage of  
 2166 the  $\pi^0 \rightarrow \gamma\gamma$  decay isotropy in the center-of-mass frame. Thus, any anisotropy  
 2167 indicates an inefficiency in the detector. Results from this analysis are illustrated  
 2168 in Fig. 43. Generally, this relative efficiency is above 90%, and agrees within  
 2169 5% of that determined from simulation.

2170 The models for the simulated response of both calorimeters are being up-  
 2171 dated, and the final agreement between photon efficiency determined in data

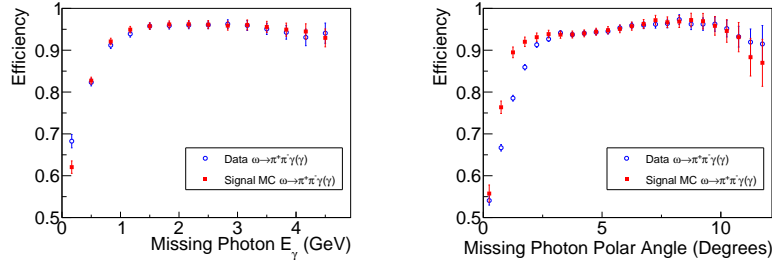


Figure 42: Photon reconstruction efficiency in FCAL determined from  $\gamma p \rightarrow \omega p$ ,  $\omega \rightarrow \pi^+\pi^-\pi^0$ ,  $\pi^0 \rightarrow \gamma(\gamma)$  as a function of (left) photon energy and (right) photon polar angle. Good agreement between data and simulation is observed in the fiducial region  $\theta = 2^\circ - 10.6^\circ$ . (Color online)

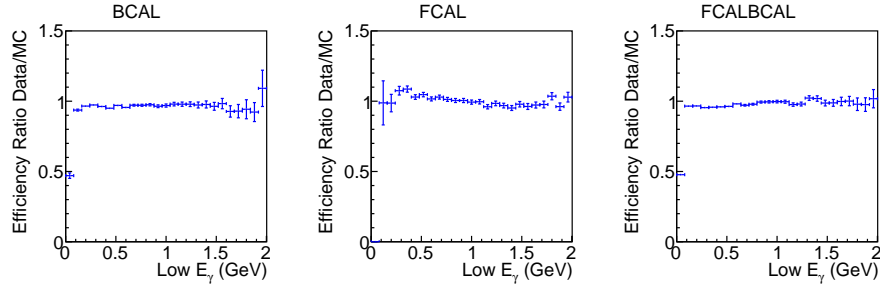


Figure 43: Ratios of relative photon reconstruction efficiency between data and simulation determined from  $\pi^0 \rightarrow \gamma\gamma$  decays in  $\gamma p \rightarrow \pi^+\pi^-\pi^0 p$  events. The efficiency ratios are shown for the cases where (left) both photons were measured in the BCAL, (middle) both photons were measured in the FCAL, and (right) one photon was measured in the BCAL and the other in the FCAL.

2172 and simulation is expected to improve.

2173 Detailed studies of detector performance determined the standard fiducial  
 2174 region for most analyses to be  $\theta = 2^\circ - 10.6^\circ$  and  $\theta > 11.3^\circ$ . These requirements  
 2175 avoid the region dominated by beam-related backgrounds at small  $\theta$  and the  
 2176 transition region between the BCAL and FCAL, where shower reconstruction  
 2177 is difficult.

### 2178 15.3. Kinematic fitting

2179 Kinematic fitting is a powerful tool to improve the resolution of measured  
 2180 data and to distinguish between different reactions. In GLUEX, this method  
 2181 takes advantage of the fact that the initial state is very well known, with the  
 2182 target proton at rest, and the incident photon energy measured with very high  
 2183 precision ( $< 0.1\%$ ). This knowledge of the initial state gives substantial im-  
 2184 provements in the kinematic quantities determined for exclusive reactions. The

2185 most common kinematic fits that are performed are those that impose energy-  
 2186 momentum conservation between the initial and final-state particles. Additional  
 2187 optional constraints in these fits are for the four-momenta of the daughters of  
 2188 an intermediate particle to add up to a fixed invariant mass, and for all the  
 2189 particles to come from a common vertex (or multiple vertices, in the case of  
 2190 reactions containing long-lived, decaying particles).

2191 To illustrate the performance of the kinematic fit, we use a sample of  $\gamma p \rightarrow$   
 2192  $\eta p$ ,  $\eta \rightarrow \pi^+ \pi^- \pi^0$  events selected using a combination of standard particle iden-  
 2193 tification and simple kinematic selections. The use of the kinematic fit im-  
 2194 proves the  $\eta$ -mass resolution from 2.6 MeV to 1.7 MeV, which is typical of  
 2195 low-multiplicity meson production reactions. The quality of the kinematic fit is  
 2196 determined using either the probability calculated from the  $\chi^2$  of the fit and the  
 2197 number of degrees-of-freedom or the  $\chi^2$  of the fit itself. The distributions of the  
 2198 kinematic fit  $\chi^2$  and probability are illustrated in Fig. 44 for both reconstructed  
 2199 and simulated data. The agreement between the two distributions is good for  
 2200 small  $\chi^2$  (large probability), and flat over most of the probability range, indicat-  
 2201 ing good overall performance for most signal events. The disagreement between  
 2202 the two distributions at larger  $\chi^2$  (probability  $< 0.2$ ) is due to a combination of  
 2203 background events and deficiencies in the modelling of poorly measured events  
 2204 with large resolution.

2205 The performance of the reconstruction algorithms and kinematic fit can be  
 2206 studied through investigating the “pull” distributions, where the pull of a vari-  
 2207 able  $x$  is defined by comparing its measured values and uncertainties and those  
 2208 resulting from the kinematic fit as

$$\text{pull}_x = \frac{x_{\text{fitted}} - x_{\text{measured}}}{\sqrt{\sigma_{x,\text{measured}}^2 - \sigma_{x,\text{fitted}}^2}}. \quad (1)$$

2209 If the parameters and covariances of reconstructed particles are Gaussian, are  
 2210 measured accurately, and the fit is performing correctly, then these pull values  
 2211 are expected to have a Gaussian distribution centered at zero with a width  $\sigma$   
 2212 of 1. If the pull distributions are not centered at zero, this is an indication that  
 2213 there is a bias in the measurements or the fit. If  $\sigma$  varies from unity, this is an  
 2214 indication that the covariance matrix elements are not correctly estimated.

2215 As an example, the pull distributions for the momentum components of the  
 2216  $\pi^-$  in reconstructed  $\gamma p \rightarrow \eta p$ ,  $\eta \rightarrow \pi^+ \pi^- \pi^0$  events are shown in Fig. 45.  
 2217 Both real and simulated data have roughly Gaussian shapes with similar widths.  
 2218 More insight into the stability of the results of the kinematic fit can be found  
 2219 by studying the variation of the means and widths of the fit distributions as  
 2220 a function of the fit probability. The results of such a study are summarized  
 2221 in Fig. 46, where broad agreement between the results from real and simulated  
 2222 data is seen. The means of the pull distributions are generally around zero (with  
 2223  $p_x$  and its mean of roughly  $-0.1$  a notable exception), and the widths within  
 2224 about 20% of unity. This level of performance and agreement between data and  
 2225 simulation is acceptable for the initial analysis of data, where very loose cuts on  
 2226 the kinematic fit  $\chi^2$  are performed, and steady improvement in the modeling of

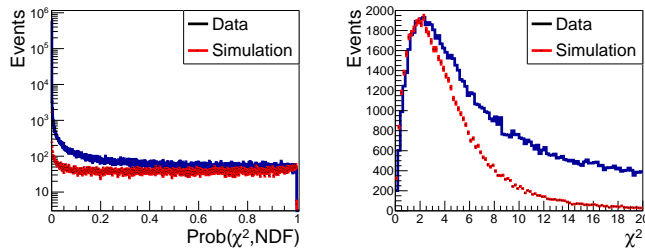


Figure 44: Distribution of kinematic fit (left) probability and (right)  $\chi^2$  for reconstructed  $\gamma p \rightarrow \eta p$ ,  $\eta \rightarrow \pi^+ \pi^- \pi^0$  events in data and simulation. Both distributions agree reasonably for well-measured events, and diverge due to additional background in data and differences in modeling poorly-measured events. (Color online)

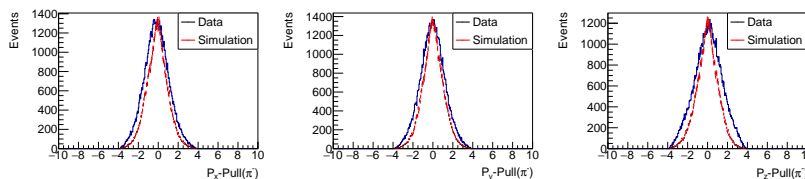


Figure 45: Pull distributions for momentum components of the  $\pi^-$  from reconstructed  $\gamma p \rightarrow \eta p$ ,  $\eta \rightarrow \pi^+ \pi^- \pi^0$  events in data and simulation for events with fit probability  $> 0.01$ : (left)  $p_x$ , (center)  $p_y$ , (right)  $p_z$ . (Color online)

2227 the covariance matrices of reconstructed particles is expected to continue.

#### 2228 15.4. Invariant-mass resolution

2229 The invariant-mass resolution for resonances depends on the momenta and  
 2230 angles of their decay products. This resolution has been studied using several  
 2231 different channels, which are illustrated in Figs. 47 and 49. A typical meson  
 2232 production channel including both charged particles and photons,  $\omega \rightarrow \pi^+ \pi^- \pi^0$   
 2233 from  $\gamma p \rightarrow \omega p$ , is shown in the left panel of Fig. 47. The distribution shows  
 2234 the strong peak due to  $\omega$  meson production. Other structures are also seen,  
 2235 such as peaks corresponding to the production of  $\eta$  and  $\phi$  mesons. The  $\omega$  peak  
 2236 resolution obtained is 26.1 MeV when using only the reconstructed particle 4-  
 2237 vectors, and improves to 16.4 MeV after a kinematic fit. The invariant-mass  
 2238 distribution of  $\pi^+ \pi^-$  from  $\gamma p \rightarrow K_S K^+ \pi^- p$ ,  $K_S \rightarrow \pi^+ \pi^-$  exhibits the peak  
 2239 due to  $K_S \rightarrow \pi^+ \pi^-$  decays (right panel of Fig. 47). The  $K_S$  peak resolution is  
 2240 17.0 MeV using only the reconstructed charged particle 4-vectors, and improves  
 2241 to 8.6 MeV after a kinematic fit imposing energy and momentum conservation.  
 2242 The dependence of the  $K_S \rightarrow \pi^+ \pi^-$  invariant-mass resolution as a function of  
 2243  $K_S$  momentum is shown in Fig. 48, both before and after an energy/momentum-  
 2244 constraint kinematic fit.

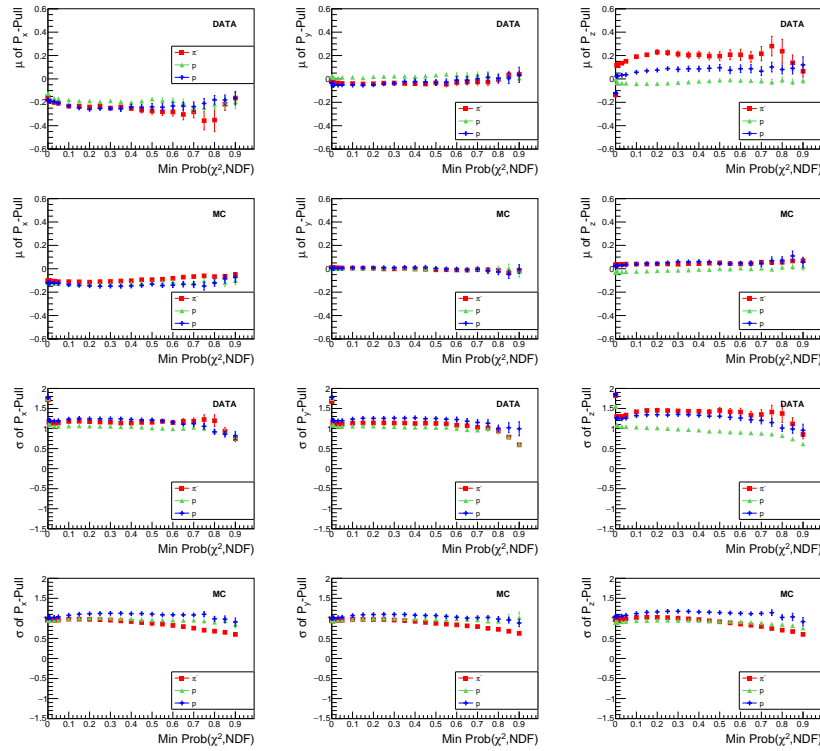


Figure 46: Pull means (top) and sigmas (bottom) for the momentum components of each particle as a function of the minimum probability required of the fit from reconstructed  $\gamma p \rightarrow \eta p, \eta \rightarrow \pi^+ \pi^- \pi^0$  events. (Color online)



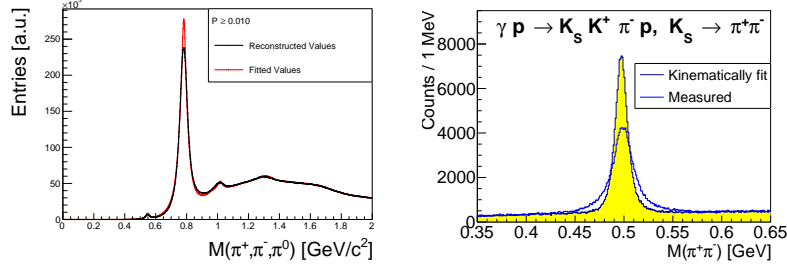


Figure 47: (Left top)  $\pi^+\pi^-\pi^0$  invariant-mass distribution from  $\gamma p \rightarrow \pi^+\pi^-\pi^0 p$  (Right top)  $\pi^+\pi^-$  invariant mass distribution from  $\gamma p \rightarrow K_S K^+ \pi^- p$ ,  $K_S \rightarrow \pi^+\pi^-$ . (Color online)

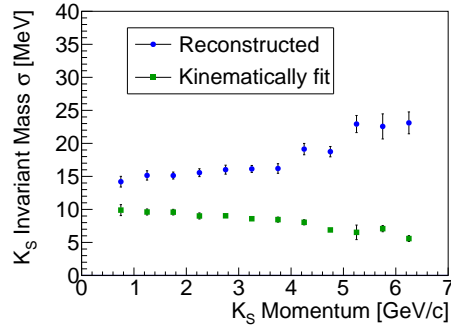


Figure 48:  $K_S \rightarrow \pi^+\pi^-$  invariant mass resolution for the events shown in Fig. 47, as a function of  $K_S$  momentum, both before and after a kinetic fit, which constrains energy and momentum conservation. (Color online)

2245 The invariant mass of  $\Lambda^0\pi^-$  from  $\gamma p \rightarrow K^+K^+\pi^-\pi^-p$  is shown in the left  
 2246 panel of Fig. 49, illustrating the peak due to  $\Xi^- \rightarrow \pi^-\Lambda^0$ ,  $\Lambda^0 \rightarrow p\pi^-$ . The  $\Xi^-$   
 2247 peak resolution obtained is 7.3 MeV when using only the reconstructed charged  
 2248 particle 4-vectors, and improves to 4.6 MeV after a kinematic fit imposing en-  
 2249 ergy and momentum conservation and the additional constraint that the mass  
 2250 of the  $p\pi^-$  pairs must be that of the  $\Lambda^0$  mass. The  $e^+e^-$  invariant mass distri-  
 2251 bution from kinematically fit  $\gamma p \rightarrow e^+e^-p$  events is shown in the right panel of  
 2252 Fig. 49, illustrating the peak due to  $J/\psi \rightarrow e^+e^-$ . The resolution of the peak is  
 2253 13.7 MeV.

### 2254 15.5. Particle identification

2255 Particle identification in GLUEX uses information from both energy loss in  
 2256 different detector systems and time-of-flight measurements. This information  
 2257 can be used for identification in several ways. The simplest method is to apply  
 2258 selections directly on the relevant PID variables. To include detector resolution  
 2259 information, one can create a  $\chi^2$  variable comparing a measured value to the

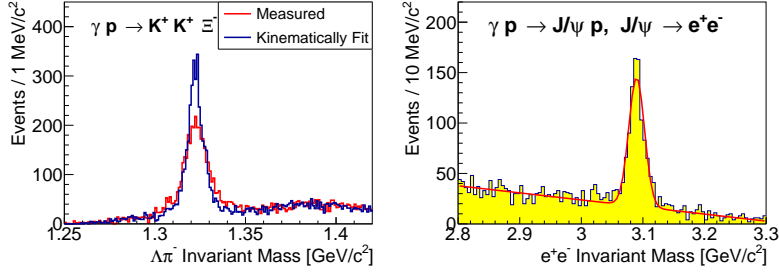


Figure 49: (Left)  $\Lambda^0\pi^-$  invariant mass distribution from  $\gamma p \rightarrow K^+K^+\pi^-\pi^-p$ . (Right)  $e^+e^-$  invariant mass distribution from kinematically fit  $\gamma p \rightarrow e^+e^-p$  events. (Color online)

2260 expected value for a particular hypothesis, that is

$$\chi^2(p) = \left( \frac{X(\text{measured}) - X(\text{expected})_p}{\sigma_X} \right)^2 \quad (2)$$

2261 where  $X$  is the given PID variable,  $p$  is the particle hypothesis, and  $\sigma_X$  is the  
 2262 resolution of this variable. Multiple PID variables can be combined into one  
 2263 probability, or a figure-of-merit. Standard, loose selections on time-of-flight and  
 2264 energy loss are sufficient for initial physics analyses, while the performance of  
 2265 more complicated selections is being actively studied.

2266 At sufficiently large  $\theta$ , the energy loss for charged particles in the central  
 2267 drift chamber  $dE/dx$  can be used. Fig. 50 illustrates these distributions for  
 2268 positively charged particles, showing a clear separation of pions and protons in  
 2269 the momentum range  $\lesssim 1$  GeV. The  $dE/dx$  resolution is approximately 27%,  
 2270 with the separation between the pion and proton bands dropping from about  $8\sigma$   
 2271 at  $p = 0.5$  GeV/ $c$  to about  $2\sigma$  at  $p = 1.0$  GeV/ $c$ , with both bands fully merged  
 2272 by  $p = 1.5$  GeV/ $c$ .

2273 The primary means of particle identification is through time-of-flight mea-  
 2274 surements, and information from several sources is combined to make the most  
 2275 accurate determination. The RF reference signal from the accelerator is used to  
 2276 define the time when each photon bunch enters the target. The reconstructed  
 2277 final-state particles are used to determine which photon bunch most likely gen-  
 2278 erated the detected reaction, with the primary determination coming from the  
 2279 signals from the Start Counter associated with the charged particle tracks. The  
 2280 photon bunch determination has a resolution of  $< 10$  ps. Each charged par-  
 2281 ticle is associated with additional timing information based on the hit in the  
 2282 highest resolution detector (for example the BCAL or TOF). The flight time  
 2283 to this measured hit  $t_{\text{meas}}$  relative to the time of the photon bunch that gen-  
 2284 erated the event  $t_{\text{RF}}$  can be used to distinguish between particles of different  
 2285 mass. Two common variables that are used are the velocity ( $\beta$ ) determined  
 2286 using the measured time-of-flight and the momentum of the particle, and  $\Delta t_{\text{RF}}$ ,  
 2287 the difference between the measured and RF times after they both have been

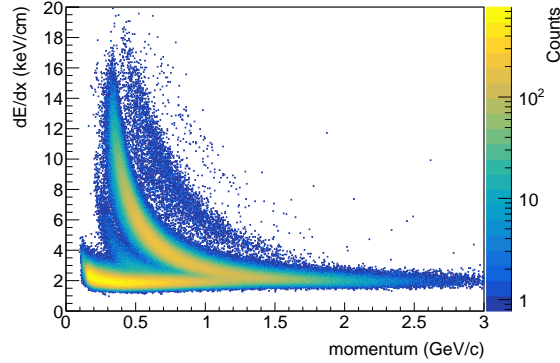


Figure 50: CDC energy loss ( $dE/dx$ ) for positively charged particles that have at least 20 hits in the detector, as a function of measured particle momentum. The band corresponding to protons curves upwards, showing a larger energy loss than pions and other lighter particles at low momentum. The two bands show a clear separation for momenta  $\gtrsim 1$  GeV. A faint kaon band can be seen between them.

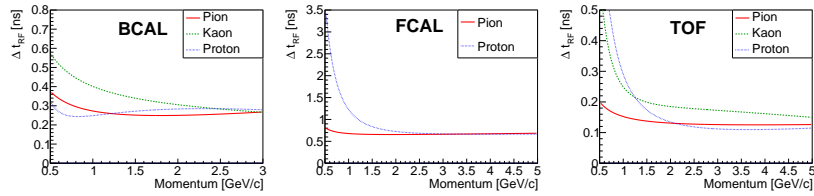


Figure 51: Resolution as a function of particle momentum for  $\Delta t_{\text{RF}}$  in various subdetectors: (left) BCAL, (center) FCAL, (right) TOF (Color online)

2288 extrapolated back to the center of the target, assuming some particle-mass hypo-  
 2289 thesis. An example of the separation between different particle types can be  
 2290 seen in Fig. 28. The loose selections used for initial analyses of this data placed  
 2291 on the  $\Delta t_{\text{RF}}$  distributions and the momentum dependence of the resolution of  
 2292 this variable in different detectors are shown in Fig. 51. Requiring reconstructed  
 2293 particles to have  $\Delta t_{\text{RF}} \lesssim 1 - 2$  ns has been found to be sufficient for analyses  
 2294 of high-yield channels which are the focus of initial analysis. The study of the  
 2295 selections required for more demanding channels is ongoing.

2296 Electrons are identified using the ratio of their energy loss in the electromag-  
 2297 netic calorimeters  $E$  to the momentum reconstructed in the drift chambers  $p$ .  
 2298 This  $E/p$  ratio should be approximately unity for electrons and less for hadrons.  
 2299 The overall distribution of this variable is illustrated for both calorimeters in  
 2300 Fig. 52. Other variables, such as the shape of the showers generated by the  
 2301 charged particles in the calorimeter, promise to provide additional information  
 2302 to separate electron and hadron showers.

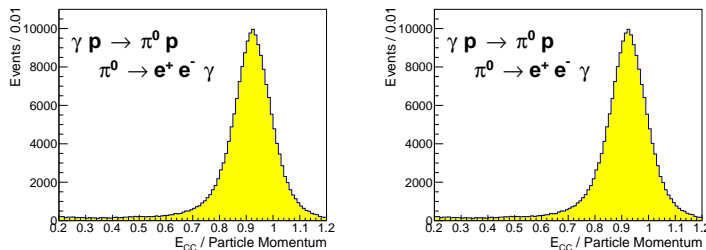


Figure 52: Electron identification in the calorimeters is performed using the  $E/p$  variable, the ratio of the energy loss in the electromagnetic calorimeters ( $E$ ) to the momentum reconstructed in the drift chambers ( $p$ ). This distribution is shown for selected samples of electrons from (left)  $\gamma p \rightarrow \pi^0 p$ ,  $\pi^0 \rightarrow e^+ e^- \gamma$ , where the  $e^\pm$  are reconstructed in the FCAL, and (right) ....

## 2303 16. Summary and outlook

2304 We have presented the design, construction, and performance, of the beam-  
 2305 line and detector of the GLUEX experiment in Hall D at Jefferson Lab during  
 2306 its first phase of operation. The experiment operated routinely at an incident  
 2307 photon flux of  $2 \times 10^7$  photons/s in the coherent peak with an open trigger,  
 2308 taking data at 40 kHz, and recording 600 MB/s to tape with live time  $>95\%$ .  
 2309 During this period the experiment accumulated  $121.4 \text{ pb}^{-1}$  in the coherent peak  
 2310 and  $319.4 \text{ pb}^{-1}$  total for  $E_\gamma > 8.1 \text{ GeV}$ . Data were collected in two sets of or-  
 2311 thogonal linear polarizations of the incident photons, with  $\sim 23\%$  of the data in  
 2312 each of the four orientations. The remaining  $\sim 11\%$  was collected with unpolar-  
 2313 ized photons. Approximately 270 billion triggers were accumulated during this  
 2314 period, as shown in Fig. 53.

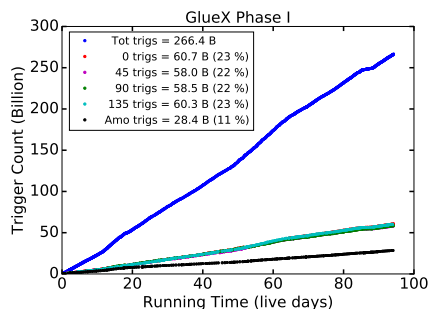


Figure 53: Plot of integrated number of triggers versus the number of live days in 2017 and 2018. The legend provides the number of triggers for the four diamond orientations relative to the horizontal ( $0, 45, 90, 135^\circ$ ) and the amorphous radiator. The trigger curves of the four diamond configurations fall on top of one another, as we attempted to match the amount of data taken for each configuration. (Color online)

2315 The operational characteristics of the charged and neutral particle detectors,

2316 trigger, DAQ, online and offline systems have been verified, and individual com-  
2317 ponents performed as designed. The detector is able to reconstruct exclusive  
2318 final states, reconstruction efficiencies have been determined, and Monte Carlo  
2319 simulations compare well with experimental data. The infrastructure is in place  
2320 to process our high volume of data both on the JLab computing farm as well  
2321 on other offsite facilities, providing the ability to process the data in a timely  
2322 fashion.

2323 Future running will include taking data at higher luminosity and with im-  
2324 proved particle identification capability. The GLUEX experiment has already  
2325 implemented the necessary infrastructure to allow the experiment to operate at  
2326 a flux of  $5 \times 10^7$  photons/s in the coherent peak for the upcoming run periods  
2327 and has added a new DIRC detector<sup>71</sup> to extend particle identification of kaons  
2328 to higher momenta.

## 2329 **17. Acknowledgments**

2330 We gratefully acknowledge the outstanding efforts of technical support at  
2331 all the collaborating institutions and the support groups at Jefferson Lab that  
2332 completed the assembly, installation, and maintenance of the detector. This  
2333 work was supported in part by the U.S. Department of Energy, the U.S. National  
2334 Science Foundation, the German Research Foundation, Forschungszentrum  
2335 Jülich GmbH, GSI Helmholtzzentrum für Schwerionenforschung GmbH,  
2336 the Russian Foundation for Basic Research, the UK Science and Technology  
2337 Facilities Council, the Chilean Comisión Nacional de Investigación Científica y  
2338 Tecnológica, the National Natural Science Foundation of China, and the China  
2339 Scholarship Council. This material is based upon work supported by the U.S.  
2340 Department of Energy, Office of Science, Office of Nuclear Physics under con-  
2341 tract DE-AC05-06OR23177.

---

<sup>71</sup>Four “bar boxes” from the BaBar DIRC[93] detector have been installed and tested.

2342 **References**

- 2343 [1] V. Crede, C. A. Meyer, The Experimental Status of Glueballs, Prog. Part.  
2344 Nucl. Phys. 63 (2009) 74–116. [arXiv:0812.0600](https://arxiv.org/abs/0812.0600), [doi:10.1016/j.ppnp.](https://doi.org/10.1016/j.ppnp.2009.03.001)  
2345 2009.03.001.
- 2346 [2] C. A. Meyer, Y. Van Haarlem, The Status of Exotic-quantum-number  
2347 Mesons, Phys. Rev. C82 (2010) 025208. [arXiv:1004.5516](https://arxiv.org/abs/1004.5516), [doi:10.1103/](https://doi.org/10.1103/PhysRevC.82.025208)  
2348 [PhysRevC.82.025208](https://doi.org/10.1103/PhysRevC.82.025208).
- 2349 [3] C. A. Meyer, E. S. Swanson, Hybrid Mesons, Prog. Part. Nucl. Phys. 82  
2350 (2015) 21–58. [doi:10.1016/j.ppnp.2015.03.001](https://doi.org/10.1016/j.ppnp.2015.03.001).
- 2351 [4] The GlueX Collaboration, The GlueX Experiment in Hall D, GlueX Project  
2352 Overviews (hyperlink) (2010).
- 2353 [5] C. W. Leemann, D. R. Douglas, G. A. Krafft, The Continuous Electron  
2354 Beam Accelerator Facility: CEBAF at the Jefferson Laboratory, Ann.  
2355 Rev. Nucl. Part. Sci. 51 (2001) 413–450. [doi:10.1146/annurev.nucl.](https://doi.org/10.1146/annurev.nucl.51.101701.132327)  
2356 [51.101701.132327](https://doi.org/10.1146/annurev.nucl.51.101701.132327).
- 2357 [6] U. Timm, Coherent Bremsstrahlung of Electrons in Crystals, Fortschritt  
2358 der Physik 17 (1969) 765–808. [doi:10.1002/prop.19690171202](https://doi.org/10.1002/prop.19690171202).
- 2359 [7] K. Livingston, The Stonehenge technique. A method for aligning co-  
2360 herent bremsstrahlung radiators, Nucl. Instrum. Meth. A 603 (3)  
2361 (2009) 205 – 213. Available from: [http://www.sciencedirect.com/](http://www.sciencedirect.com/science/article/pii/S0168900209003477)  
2362 [science/article/pii/S0168900209003477](http://www.sciencedirect.com/science/article/pii/S0168900209003477), [doi:https://doi.org/10.](https://doi.org/10.1016/j.nima.2009.02.010)  
2363 [1016/j.nima.2009.02.010](https://doi.org/10.1016/j.nima.2009.02.010).
- 2364 [8] C. Meyer, A review of asymmetry measurements in vec-  
2365 tor meson photoproduction experiments, Tech. Rep. 3076,  
2366 Carnegie Mellon University, [https://halldweb.jlab.org/doc-](https://halldweb.jlab.org/doc-private/DocDB/ShowDocument?docid=3076)  
2367 [private/DocDB/ShowDocument?docid=3076](https://halldweb.jlab.org/doc-private/DocDB/ShowDocument?docid=3076) (August 2016).
- 2368 [9] H. Bilokon, et al., Coherent bremsstrahlung in crystals as a tool for  
2369 producing high energy photon beams to be used in photoproduction  
2370 experiments at CERN SPS, Nucl. Instrum. Meth. 204 (1983) 299–310.  
2371 Available from: [https://www.sciencedirect.com/science/article/](https://www.sciencedirect.com/science/article/pii/0167508783900613)  
2372 [pii/0167508783900613](https://www.sciencedirect.com/science/article/pii/0167508783900613), [doi:10.1016/0167-5087\(83\)90061-3](https://doi.org/10.1016/0167-5087(83)90061-3).
- 2373 [10] G. Yang, et al., Rocking curve imaging for diamond radiator crys-  
2374 tal selection, Diamond and Related Materials 19 (7) (2010) 719 –  
2375 722, proceedings of Diamond 2009, The 20th European Conference  
2376 on Diamond, Diamond-Like Materials, Carbon Nanotubes and Ni-  
2377 trides, Part 2. Available from: [http://www.sciencedirect.com/](http://www.sciencedirect.com/science/article/pii/S0925963510000063)  
2378 [science/article/pii/S0925963510000063](http://www.sciencedirect.com/science/article/pii/S0925963510000063), [doi:https://doi.org/10.](https://doi.org/10.1016/j.diamond.2009.12.017)  
2379 [1016/j.diamond.2009.12.017](https://doi.org/10.1016/j.diamond.2009.12.017).

- 2380 [11] G. Yang, et al., High resolution X-ray diffraction study of single crystal  
2381 diamond radiators, *physica status solidi (a)* 209 (9) (2012) 1786–1791.  
2382 Available from: [https://onlinelibrary.wiley.com/doi/abs/10.1002/](https://onlinelibrary.wiley.com/doi/abs/10.1002/pssa.201200017)  
2383 [pssa.201200017](https://onlinelibrary.wiley.com/doi/abs/10.1002/pssa.201200017), doi:10.1002/pssa.201200017.
- 2384 [12] J. Borggreen, B. Elbek, L. P. Nielsen, A proposed spectro-  
2385 graph for heavy particles, *Nuclear Instruments and Methods* 24  
2386 (1963) 1 – 12. Available from: [http://www.sciencedirect.](http://www.sciencedirect.com/science/article/pii/0029554X63902763)  
2387 [com/science/article/pii/0029554X63902763](http://www.sciencedirect.com/science/article/pii/0029554X63902763), doi:[https://doi.org/](https://doi.org/10.1016/0029-554X(63)90276-3)  
2388 [10.1016/0029-554X\(63\)90276-3](https://doi.org/10.1016/0029-554X(63)90276-3).
- 2389 [13] D. Sober, et al., The bremsstrahlung tagged photon beam in Hall  
2390 B at JLab, *Nucl. Instrum. and Meth. A* 440 (2) (2000) 263  
2391 – 284. Available from: [http://www.sciencedirect.com/science/](http://www.sciencedirect.com/science/article/pii/S0168900299007846)  
2392 [article/pii/S0168900299007846](http://www.sciencedirect.com/science/article/pii/S0168900299007846), doi:[http://dx.doi.org/10.1016/](http://dx.doi.org/10.1016/S0168-9002(99)00784-6)  
2393 [S0168-9002\(99\)00784-6](http://dx.doi.org/10.1016/S0168-9002(99)00784-6).
- 2394 [14] G. L. Yang, A summary of the optics design for the  
2395 GLUEX single dipole tagger spectrometer, Tech. Rep. GlueX-  
2396 doc-1186, Glasgow University, [https://halldweb.jlab.org/doc-](https://halldweb.jlab.org/doc-public/DocDB/ShowDocument?docid=1186)  
2397 [public/DocDB/ShowDocument?docid=1186](https://halldweb.jlab.org/doc-public/DocDB/ShowDocument?docid=1186) (January 2009).
- 2398 [15] A. Somov, Resolution studies of a dipole tagger mag-  
2399 net: response to the magnet review referees, Tech. Rep.  
2400 GlueX-doc-1368, Jefferson Lab, [https://halldweb.jlab.org/doc-](https://halldweb.jlab.org/doc-public/DocDB/ShowDocument?docid=1368)  
2401 [public/DocDB/ShowDocument?docid=1368](https://halldweb.jlab.org/doc-public/DocDB/ShowDocument?docid=1368) (January 2010).
- 2402 [16] D. I. Sober, Analysis of the Hall D Tagger Dipole  
2403 Magnet Field Maps, Tech. Rep. GlueX-doc-4271, The  
2404 Catholic University of America, [https://halldweb.jlab.org/doc-](https://halldweb.jlab.org/doc-private/DocDB/ShowDocument?docid=4271)  
2405 [private/DocDB/ShowDocument?docid=4271](https://halldweb.jlab.org/doc-private/DocDB/ShowDocument?docid=4271) (July 2015).
- 2406 [17] H. Fischer, et al., Implementation of the dead time free F1 TDC in the  
2407 COMPASS detector readout, *Nucl. Instrum. Meth. A* 461 (2001) 507–510.  
2408 [arXiv:hep-ex/0010065](https://arxiv.org/abs/hep-ex/0010065), doi:10.1016/S0168-9002(00)01285-7.
- 2409 [18] V. Popov, et al., Performance studies of Hamamatsu R9800 photomultiplier  
2410 tube with a new active base designed for use in the Hall D Broadband  
2411 tagger Hodoscope, in: 2014 IEEE Nuclear Science Symposium and Medical  
2412 Imaging Conference (NSS/MIC), Seattle, WA, 2014, pp. 1–4. doi:10.  
2413 1109/NSSMIC.2014.7431075.
- 2414 [19] G. Miller, D. R. Walz, A Tungsten Pin Cushion Photon Beam Moni-  
2415 tor, *Nucl. Instrum. Meth.* 117 (1974) 33. doi:10.1016/0029-554X(74)  
2416 90380-2.
- 2417 [20] M. Dugger, et al., Design and construction of a high-energy photon  
2418 polarimeter, *Nucl. Instrum. Meth. A* 867 (2017) 115 – 127. Avail-  
2419 able from: [http://www.sciencedirect.com/science/article/pii/](http://www.sciencedirect.com/science/article/pii/S0168900217305715)  
2420 [S0168900217305715](http://www.sciencedirect.com/science/article/pii/S0168900217305715), doi:10.1016/j.nima.2017.05.026.

- 2421 [21] F. Barbosa, et al., Pair spectrometer hodoscope for Hall D at Jef-  
2422 ferson Lab, Nucl. Instrum. Meth. A 795 (2015) 376 – 380. Avail-  
2423 able from: [http://www.sciencedirect.com/science/article/pii/](http://www.sciencedirect.com/science/article/pii/S0168900215007573)  
2424 [S0168900215007573](http://www.sciencedirect.com/science/article/pii/S0168900215007573), doi:[https://doi.org/10.1016/j.nima.2015.06.](https://doi.org/10.1016/j.nima.2015.06.012)  
2425 012.
- 2426 [22] F. Barbosa, et al., Time characteristics of detectors based on silicon pho-  
2427 tomultipliers for the GlueX experiment, Instrum. Exp. Tech. 60 (2017)  
2428 322–329. doi:10.1134/S0020441217030022.
- 2429 [23] A. Somov, others., The silicon photomultipliers in the detector subsystems  
2430 of the GlueX experiment, J. Phys. Conf. Ser. 798 (2017) 012223. doi:  
2431 10.1088/1742-6596/798/1/012223.
- 2432 [24] I. A. Tolstukhin, et al., Recording of relativistic particles in thin scin-  
2433 tillators, Instrum. Exp. Tech. 57 (6) (2014) 658–661. doi:10.1134/  
2434 S0020441214060153.
- 2435 [25] A. Somov, et al., Commissioning of the Pair Spectrometer of the GlueX  
2436 experiment, J. Phys. Conf. Ser. 798 (2017). doi:10.1088/1742-6596/798/  
2437 1/012175.
- 2438 [26] A. Somov, et al., Performance of the pair spectrometer of the GlueX experi-  
2439 ment, J. Phys. Conf. Ser. 675 (4) (2016) 042022. doi:10.1088/1742-6596/  
2440 675/4/042022.
- 2441 [27] A. Somov, Pair Spectrometer acceptance determination (Spring 2019),  
2442 Tech. rep., Jefferson Lab, Technical Report GlueX-doc-3924 (hyperlink)  
2443 (Feb. 2019).
- 2444 [28] D. Sober, Calibration of the Tagged Photon Beam: Normalization Meth-  
2445 ods, Shower Counter and Pair Spectrometer, Tech. rep., Catholic University  
2446 of America, Technical Report CLAS-NOTE-92-014 (hyperlink) (1992).
- 2447 [29] A. Eppich, R. Sealock, Studies of a Lead Glass Total Absorption Counter,  
2448 Tech. rep., Jefferson Lab, Technical Report CLAS-NOTE-93-011 (hyper-  
2449 link) (1993).
- 2450 [30] E. Anciant, et al., Photon Flux Normalization for CLAS, Tech. rep., CEA-  
2451 Saclay, Technical Report CLAS-NOTE-1999-002 (hyperlink) (1992).
- 2452 [31] J. S. Alcorn, H. Peterson, S. S. Lorant, SLAC two-meter diameter, 25-  
2453 kilogauss, superconducting solenoid, UAMH BINN, in: Applied Supercon-  
2454 ductivity Conference, Inst. of Electrical and Electronics Engineers, Inc.,  
2455 New York; Stanford Univ., CA, 1972, p. 273.
- 2456 [32] D. Aston, et al., The LASS spectrometer, Tech. Rep. SLAC-298,  
2457 SLAC, Stanford, CA, Technical report SLAC-R-298 (1987). Avail-  
2458 able from: [https://www-public.slac.stanford.edu/scidoc/docMeta.](https://www-public.slac.stanford.edu/scidoc/docMeta.aspx?slacPubNumber=slac-R-298)  
2459 [aspx?slacPubNumber=slac-R-298](https://www-public.slac.stanford.edu/scidoc/docMeta.aspx?slacPubNumber=slac-R-298).



- 2460 [33] J. Ballard, et al., Refurbishment and testing of the 1970's era LASS solenoid  
2461 coils for JLab's Hall D, AIP Conf. Proc. 1434 (2012) 861–868. doi:10.1063/  
2462 1.4707001.
- 2463 [34] J. Ballard, et al., Commissioning and Testing the 1970's Era LASS Solenoid  
2464 Magnet in JLab's Hall D, IEEE Trans. Appl. Supercond. 25 (3) (2015)  
2465 4500805. doi:10.1109/TASC.2014.2385152.
- 2466 [35] N. Laverdure, et al., The Hall D solenoid helium refrigeration system at  
2467 JLab, AIP Conf. Proc. 1573 (1) (2014) 329–336. doi:10.1063/1.4860719.
- 2468 [36] H. Hakobyan, et al., A double-target system for precision measurements of  
2469 nuclear medium effects, Nucl. Instrum. Meth. A: 592 (3) (2008) 218 – 223.  
2470 doi:https://doi.org/10.1016/j.nima.2008.04.055.
- 2471 [37] Y. V. Haarlem, et al., The GlueX Central Drift Chamber: Design and  
2472 Performance, Nucl. Instrum. Meth. A622 (2010) 142–156. doi:10.1016/  
2473 j.nima.2010.06.272.
- 2474 [38] N. S. Jarvis, et al., The Central Drift Chamber for GLUEX, Nucl. In-  
2475 strument. Meth. A962 (2020) 163727. doi:https://doi.org/10.1016/j.  
2476 nima.2020.163727.
- 2477 [39] J. A. Kadyk, Wire chamber aging, Nucl. Instrum. Meth. 300 (3) (1991) 436  
2478 – 479. doi:10.1016/0168-9002(91)90381-Y.
- 2479 [40] J. Vavra, Physics and chemistry of aging - early developments, Nucl. In-  
2480 strument. Meth. A515 (2003) 1 – 14, proceedings of the International Work-  
2481 shop on Aging Phenomena in Gaseous Detectors. doi:https://doi.org/  
2482 10.1016/j.nima.2003.08.124.
- 2483 [41] F. Barbosa, Electronics overview, Tech. rep., Jefferson Lab, Technical Re-  
2484 port GlueX-doc-2515 (hyperlink) (Jun. 2014).
- 2485 [42] G. Visser, High Density 125 MSPS Differential Input ADC Module Spec-  
2486 ifications for GlueX Drift Chamber Application (2008). Available  
2487 from: [https://halldweb.jlab.org/DocDB/0008/000855/002/Drifts\\_](https://halldweb.jlab.org/DocDB/0008/000855/002/Drifts_ADC_Specification_Document.pdf)  
2488 [ADC\\_Specification\\_Document.pdf](https://halldweb.jlab.org/DocDB/0008/000855/002/Drifts_ADC_Specification_Document.pdf).
- 2489 [43] G. Visser, et al., A 72 channel 125 MSPS analog-to-digital converter  
2490 module for drift chamber readout for the GlueX detector, in: IEEE Nu-  
2491 clear Science Symposium Medical Imaging Conference, 2010, pp. 777–781.  
2492 doi:10.1109/NSSMIC.2010.5873864.
- 2493 [44] F. Barbosa, et al., The Jefferson Lab High Resolution Time-to-Digital Con-  
2494 verter (TDC), Tech. rep., Jefferson Lab, Technical Report GlueX-doc-1021  
2495 (hyperlink) (Apr. 2008).
- 2496 [45] L. Pentchev, et al., Studies with cathode drift chambers for the GlueX  
2497 experiment at Jefferson Lab, Nucl. Instrum. Meth. A845 (2017) 281–284.  
2498 doi:10.1016/j.nima.2016.04.076.

- 2499 [46] V. Blobel, Millipede II (2007). Available from: [https://www.desy.de/](https://www.desy.de/~kleinwrt/MP2/doc/html/index.html)  
2500 [~kleinwrt/MP2/doc/html/index.html](https://www.desy.de/~kleinwrt/MP2/doc/html/index.html).
- 2501 [47] M. Staib, Calibrations for charged particle tracking and the measurements  
2502 of  $\omega$  photoproduction with the GlueX Detector, Ph.D. thesis, Carnegie  
2503 Mellon University, Department of Physics, Technical Report GlueX-doc-  
2504 3393 (hyperlink) (September 2017).
- 2505 [48] R. E. Kalman, A New Approach to Linear Filtering and Prediction Prob-  
2506 lems, ASME Journal of Basic Engineering 82 (1) (1960) 35–45. doi:  
2507 10.1115/1.3662552.
- 2508 [49] R. E. Kalman, R. S. Bucy, New Results in Linear Filtering and Prediction  
2509 Theory, ASME Journal of Basic Engineering 83 (1) (1961) 95–108. doi:  
2510 10.1115/1.3658902.
- 2511 [50] T. Beattie, et al., Construction and performance of the barrel electromag-  
2512 netic calorimeter for the GLUEX experiment, Nucl. Instrum. Meth. A896  
2513 (2018) 24 – 42. doi:10.1016/j.nima.2018.04.006.
- 2514 [51] E. Smith, Development of Silicon Photomultipliers and their Applications  
2515 to GlueX, Tech. rep., Jefferson Lab, AIP Proceedings 1753 – XI Latin  
2516 American Symposium on Nuclear Physics and Applications, Medellín,  
2517 Colombia. Technical Report GlueX-doc-2913 (hyperlink) (Dec. 2015).
- 2518 [52] F. Barbosa, et al., Silicon photomultiplier characterization for the GlueX  
2519 barrel calorimeter, Nucl. Instrum. Meth. A695 (2012) 100 – 104. doi:  
2520 10.1016/j.nima.2011.11.059.
- 2521 [53] Y. Qiang, et al., Radiation hardness tests of SiPMs for the JLab Hall D  
2522 Barrel calorimeter, Nucl. Instrum. Meth. A698 (2013) 234 – 241. doi:  
2523 10.1016/j.nima.2012.10.015.
- 2524 [54] O. Soto, et al., Characterization of novel Hamamatsu Multi Pixel Photon  
2525 Counter (MPPC) arrays for the GlueX experiment, Nucl. Instrum. Meth.  
2526 A732 (2013) 431–436. doi:10.1016/j.nima.2013.06.071.
- 2527 [55] O. Soto, et al., Novel Hamamatsu Multi-Pixel Photon Counter (MPPC) ar-  
2528 ray studies for the GlueX experiment: New results, Nucl. Instrum. Methods  
2529 A 739 (2014) 89–97. doi:10.1016/j.nima.2013.12.032.
- 2530 [56] T. Beattie, et al., Methodology for the Determination of the Photon Detec-  
2531 tion Efficiency of Large-Area Multi-Pixel Photon Counters, IEEE Trans-  
2532 actions on Nuclear Science 62 (2015) 1865–1872. doi:10.1109/TNS.2015.  
2533 2442262.
- 2534 [57] E. Smith, Development of Silicon Photomultipliers and their Applications  
2535 to GlueX Calorimetry, AIP Conference Proceedings 1753 (1) (2016) 010001.  
2536 doi:10.1063/1.4955340.

- 2537 [58] R. Crittenden, et al., A 3000 element lead-glass electromagnetic calorimeter, Nucl. Instrum. Meth. A387 (3) (1997) 377 – 394. doi:10.1016/S0168-9002(97)00101-0.  
2538  
2539
- 2540 [59] R. Jones, et al., Performance of the RadPhi detector and trigger in a high  
2541 rate tagged photon beam, Nucl. Instrum. Meth. A570 (3) (2007) 384 – 398.  
2542 doi:10.1016/j.nima.2006.09.039.
- 2543 [60] A. Brunner, et al., A Cockcroft-Walton base for the FEU84-3 photomul-  
2544 tiplier tube, Nucl. Instrum. Meth. A414 (1998) 466–476. doi:10.1016/  
2545 S0168-9002(98)00651-2.
- 2546 [61] Wikipedia contributors, CAN bus — Wikipedia, the free encyclopedia,  
2547 [Online; accessed 28-October-2019] (2019). Available from: [https://en.  
2548 wikipedia.org/w/index.php?title=CAN\\_bus&oldid=922757529](https://en.wikipedia.org/w/index.php?title=CAN_bus&oldid=922757529).
- 2549 [62] K. Moriya, et al., A measurement of the energy and timing resolution of  
2550 the GlueX Forward Calorimeter using an electron beam, Nucl. Instrum.  
2551 Meth. 726 (2013) 60 – 66. doi:10.1016/j.nima.2013.05.109.
- 2552 [63] F. Barbosa, et al., A VME64x, 16-Channel, Pipelined 250 MSPS Flash  
2553 ADC With Switched Serial (VXS) Extension, Tech. rep., Jefferson Lab,  
2554 Technical Report GlueX-doc-1022 (hyperlink) (Apr. 2007).
- 2555 [64] M. Dugger, et al., Hall D / GlueX Technical Construction Report, Chapter  
2556 3.10, Tech. rep., Jefferson Lab, Technical Report GlueX-doc-2511 (hyper-  
2557 link) (Jul. 2017).
- 2558 [65] J. V. Bennett, et al., Precision timing measurement of phototube pulses  
2559 using a flash analog-to-digital converter, Nucl. Instrum. Meth. A622 (2010)  
2560 225–230. doi:10.1016/j.nima.2010.06.216.
- 2561 [66] E. Anassontzis, et al., Relative gain monitoring of the GLUEX calorimeters,  
2562 Nucl. Instrum. Meth. A738 (2014) 41 – 49. doi:10.1016/j.nima.2013.  
2563 11.054.
- 2564 [67] B. D. Schaefer, et al., Radiation Damage of F8 Lead Glass with 20 MeV  
2565 Electrons, Nucl. Instrum. Meth. B274 (2012) 111–114. doi:10.1016/j.  
2566 nimb.2011.12.005.
- 2567 [68] R. T. Jones, et al., A bootstrap method for gain calibration and resolu-  
2568 tion determination of a lead-glass calorimeter, Nucl. Instrum. Meth. A566  
2569 (2006) 366–374. doi:10.1016/j.nima.2006.07.061.
- 2570 [69] H. A. Ghoul, et al., Measurement of the beam asymmetry  $\Sigma$  for  $\pi^0$  and  $\eta$   
2571 photoproduction on the proton at  $E_\gamma = 9$  GeV, Phys. Rev. C95 (4) (2017)  
2572 042201(R). doi:10.1103/PhysRevC.95.042201.
- 2573 [70] S. Adhikari, et al., Beam Asymmetry  $\Sigma$  for the Photoproduction of  $\eta$  and  
2574  $\eta'$  Mesons at  $E_\gamma = 8.8$  GeV, Phys. Rev. C100 (5) (2019) 052201(R). doi:  
2575 10.1103/PhysRevC.100.052201.

- 2576 [71] A. Ali, et al., First Measurement of Near-Threshold J/ Exclusive Pho-  
2577 toproduction off the Proton, *Phys. Rev. Lett.* 123 (7) (2019) 072001.  
2578 doi:10.1103/PhysRevLett.123.072001.
- 2579 [72] E. Pooser, et al., The GlueX Start Counter Detector, *Nucl. Instrum. Meth.*  
2580 A927 (2019) 330–342. doi:10.1016/j.nima.2019.02.029.
- 2581 [73] H. Dong, et al., Integrated tests of a high speed VXS switch card and 250  
2582 MSPS flash ADCs, in: 2007 IEEE Nuclear Science Symposium Conference  
2583 Record, Vol. 1, 2007, pp. 831–833. doi:10.1109/NSSMIC.2007.4436457.
- 2584 [74] A. Somov, Level-1 Trigger of the GlueX Experiment, Tech. rep., Jefferson  
2585 Lab, Technical Report GlueX-doc-1137 (hyperlink) (Jul. 2008).
- 2586 [75] A. Somov, Update on the trigger simulation, Tech. rep., Jefferson Lab,  
2587 Technical Report GlueX-doc-1272 (hyperlink) (Jul. 2009).
- 2588 [76] A. Somov, Development of level-1 triggers for experiments at Jefferson Lab,  
2589 AIP Conf. Proc. 1560 (1) (2013) 700–702. doi:10.1063/1.4826876.
- 2590 [77] S. Boyarinov and others, The CLAS12 Data Acquisition System, *Nucl. In-*  
2591 *strum. Meth.*In press (2020). doi:10.1016/j.nima.2020.163698.
- 2592 [78] C. Slominski, et al., A MySQL based EPICS archiver, Proceedings,  
2593 ICALEPCS2009 (2010) 447–449 Available from: <http://accelconf.web.cern.ch/AccelConf/icalleps2009/papers/wep021.pdf>.  
2594
- 2595 [79] X. Chen, K. Kasemir, BOY, a modern graphical operator interface edi-  
2596 tor and runtime, Proceedings, ICALEPCS2011 (2011) 1404–1406 Available  
2597 from: <http://accelconf.web.cern.ch/AccelConf/PAC2011/papers/weobn3.pdf>.  
2598
- 2599 [80] K. Kasemir, et al., The Best Ever Alarm System Toolkit, Proceedings,  
2600 ICALEPCS2009 (2010) 1062–1065 Available from: <http://accelconf.web.cern.ch/AccelConf/icalleps2009/papers/tua001.pdf>.  
2601
- 2602 [81] D. Lawrence and others, RootSpy Data Quality Monitoring System. Avail-  
2603 able from: <https://www.jlab.org/RootSpy/>.
- 2604 [82] JLab Data Acquisition Group, CODA, [coda.jlab.org](http://coda.jlab.org). Available from:  
2605 <https://coda.jlab.org>.
- 2606 [83] R. Brun, F. Rademakers, ROOT: An object oriented data analy-  
2607 sis framework, *Nucl. Instrum. Meth.* A389 (1997) 81–86, See also  
2608 <http://root.cern.ch/>. doi:10.1016/S0168-9002(97)00048-X.
- 2609 [84] M. Ito, D. Lawrence, GlueX Computing Model for RunPeriod-2017-01,  
2610 Tech. rep., Jefferson Lab, Technical Report GlueX-doc-3821 (hyperlink)  
2611 (Jun. 2018).

- 2612 [85] JLab Data Acquisition Group, CODA Online Data Formats,  
2613 <https://coda.jlab.org/drupal/system/files/eventbuilding.pdf>.
- 2614 [86] R. Brun, F. Bruyant, M. Maire, A. C. McPherson, P. Zancarini, GEANT3  
2615 (1987).
- 2616 [87] S. Agostinelli, et al., GEANT4: A Simulation toolkit, Nucl. Instrum. Meth.  
2617 A506 (2003) 250–303. doi:10.1016/S0168-9002(03)01368-8.
- 2618 [88] J. Allison, et al., Recent developments in Geant4, Nucl. Instrum. Meth.  
2619 A835 (2016) 186–225. doi:10.1016/j.nima.2016.06.125.
- 2620 [89] R. Jones, HDDS Schema. Available from: [https://halldsvn.jlab.org/  
2621 repos/trunk/hdds/HDDS-1\\_1.xsd](https://halldsvn.jlab.org/repos/trunk/hdds/HDDS-1_1.xsd).
- 2622 [90] R. Jones, Detector Models for GlueX Monte Carlo Simulation: the CD2  
2623 Baseline, Tech. rep., University of Connecticut, Technical Report GlueX-  
2624 doc-732 (hyperlink) (Jan. 2007).
- 2625 [91] R. Jones, HDDM – Hall D Data Model, Tech. rep., University of Connecti-  
2626 cut, Technical Report GlueX-doc-65 (hyperlink) (Sep. 2003).
- 2627 [92] T. Sjostrand, S. Mrenna, P. Z. Skands, PYTHIA 6.4 Physics and Manual,  
2628 JHEP 05 (2006) 026. doi:10.1088/1126-6708/2006/05/026.
- 2629 [93] B. Aubert, et al., The BaBar detector, Nucl. Instrum. Meth. A479 (2002)  
2630 1–116. doi:10.1016/S0168-9002(01)02012-5.